



TEZ ŞABLONU ONAY FORMU
THESIS TEMPLATE CONFIRMATION FORM

1. Şablonda verilen yerleşim ve boşluklar değiştirilmemelidir.
2. **Jüri tarihi** Başlık Sayfası, İmza Sayfası, Abstract ve Öz'de ilgili yerlere yazılmalıdır.
3. İmza sayfasında jüri üyelerinin unvanları doğru olarak yazılmalıdır. Tüm imzalar **mavi pilot kalemle** atılmalıdır.
4. **Disiplinlerarası** programlarda görevlendirilen öğretim üyeleri için jüri üyeleri kısmında tam zamanlı olarak çalıştıkları anabilim dalı başkanlığının ismi yazılmalıdır. Örneğin: bir öğretim üyesi Biyoteknoloji programında görev yapıyor ve biyoloji bölümünde tam zamanlı çalışıyorsa, İmza sayfasına biyoloji bölümü yazılmalıdır. İstisnai olarak, disiplinler arası program başkanı ve tez danışmanı için disiplinlerarası program adı yazılmalıdır.
5. Tezin **son sayfasının sayfa** numarası Abstract ve Öz'de ilgili yerlere yazılmalıdır.
6. Bütün chapterlar, referanslar, ekler ve CV sağ sayfada başlamalıdır. Bunun için **kesmeler** kullanılmıştır. **Kesmelerin kayması** fazladan boş sayfaların oluşmasına sebep olabilir. Bu gibi durumlarda paragraf (¶) işaretine tıklayarak kesmeleri görünür hale getirin ve yerlerini **kontrol edin**.
7. Figürler ve tablolar kenar boşluklarına taşmamalıdır.
8. Şablonda yorum olarak eklenen uyarılar dikkatle okunmalı ve uygulanmalıdır.
9. Tez yazdırılmadan önce PDF olarak kaydedilmelidir. Şablonda yorum olarak eklenen uyarılar PDF dokümanında yer almamalıdır.
10. Tez taslaklarının kontrol işlemleri tamamlandığında, bu durum öğrencilere METU uzantılı öğrenci e-posta adresleri aracılığıyla duyurulacaktır.
11. Tez yazım süreci ile ilgili herhangi bir sıkıntı yaşarsanız, [Sıkça Sorulan Sorular \(SSS\)](#) sayfamızı ziyaret ederek yaşadığınız sıkıntıyla ilgili bir çözüm bulabilirsiniz.

1. Do not change the spacing and placement in the template.
2. Write **defense date** to the related places given on Title page, Approval page, Abstract and Öz.
3. Write the titles of the examining committee members correctly on Approval Page. **Blue ink** must be used for all signatures.
4. For faculty members working in **interdisciplinary programs**, the name of the department that they work full-time should be written on the Approval page. For example, if a faculty member staffs in the biotechnology program and works full-time in the biology department, the department of biology should be written on the approval page. Exceptionally, for the interdisciplinary program chair and your thesis supervisor, the interdisciplinary program name should be written.
5. Write **the page number of the last page** in the related places given on Abstract and Öz pages.
6. All chapters, references, appendices and CV must be started on the right page. **Section Breaks** were used for this. **Change in the placement** of section breaks can result in extra blank pages. In such cases, make the section breaks visible by clicking paragraph (¶) mark and **check their position**.
7. All figures and tables must be given inside the page. Nothing must appear in the margins.
8. All the warnings given on the comments section through the thesis template must be read and applied.
9. Save your thesis as pdf and Disable all the comments before taking the printout.
10. This will be announced to the students via their METU students e-mail addresses when the control of the thesis drafts has been completed.
11. If you have any problems with the thesis writing process, you may visit our [Frequently Asked Questions \(FAQ\)](#) page and find a solution to your problem.

Yukarıda bulunan tüm maddeleri okudum, anladım ve kabul ediyorum. / I have read, understand and accept all of the items above.

Name : Hasan Halil
Surname : Karakaş
E-Mail : hasanhalilkarakas@gmail.com
Date : 07.07.2022
Signature : _____

EXPERIMENTAL INVESTIGATION OF FLOW CHARACTERISTICS OF
FLEXIBLE WINGS WITH DIFFERENT STIFFENER ORIENTATIONS
IN LINEAR TRANSLATING MOTION

A THESIS SUBMITTED TO
THE GRADUATE SCHOOL OF NATURAL AND APPLIED SCIENCES
OF
MIDDLE EAST TECHNICAL UNIVERSITY

BY

HASAN HALIL KARAKAŞ

IN PARTIAL FULFILLMENT OF THE REQUIREMENTS
FOR
THE DEGREE OF MASTER OF SCIENCE
IN
AEROSPACE ENGINEERING

AUGUST 2022

Approval of the thesis:

**EXPERIMENTAL INVESTIGATION OF FLOW CHARACTERISTICS OF
FLEXIBLE WINGS WITH DIFFERENT STIFFENER ORIENTATIONS
IN LINEAR TRANSLATING MOTION**

submitted by **HASAN HALIL KARAKAS** in partial fulfillment of the requirements
for the degree of **Master of Science in Aerospace Engineering, Middle East
Technical University** by,

Prof. Dr. Halil Kalıpçılar
Dean, Graduate School of **Natural and Applied Sciences**

Prof. Dr. Serkan Özgen
Head of the Department, **Aerospace Engineering**

Asst. Prof. Dr. Mustafa Perçin
Supervisor, **Aerospace Engineering, METU**

Examining Committee Members:

Prof. Dr. Sinan Eyi
Aerospace Engineering, METU

Asst. Prof. Dr. Mustafa Perçin
Aerospace Engineering, METU

Asst. Prof. Dr. Halil Ersin Söken
Aerospace Engineering, METU

Prof. Dr. Mehmet Metin Yavuz
Mechanical Engineering, METU

Assoc. Prof. Dr. Munir Elfarra
Aerospace Engineering, Ankara Yıldırım Beyazıt University

Date: 12.08.2022

I hereby declare that all information in this document has been obtained and presented in accordance with academic rules and ethical conduct. I also declare that, as required by these rules and conduct, I have fully cited and referenced all material and results that are not original to this work.

Name Last name : Hasan Halil Karakaş

Signature :

ABSTRACT

EXPERIMENTAL INVESTIGATION OF FLOW CHARACTERISTICS OF FLEXIBLE WINGS WITH DIFFERENT STIFFENER ORIENTATIONS IN LINEAR TRANSLATING MOTION

Karakaş, Hasan Halil
Master of Science, Aerospace Engineering
Supervisor: Asst. Prof. Dr. Mustafa Perçin

August 2022, 106 pages

This study experimentally investigates the flow field around the wings, which first accelerate with constant acceleration from the rest and then perform a linear translating motion with constant velocity. Four wings, which are 3D-printed, with a bending stiffness in different directions are examined. The difference in bending stiffness values is achieved by placing stiffeners having different angles with the leading edge on the upper surface of the wing. The stiffeners are printed with wings to obtain well-integrated wing models. The experiments are conducted in an octagonal water tank and the planar flow fields are obtained using the two-dimensional two-component particle imaging velocity measurement technique (2D2C PIV). PIV measurements show that at the initial phases of motion, a coherent leading-edge vortex is formed for all the wings tested in the experiment and LEV remains stable over a long period of movement. Although the flow fields of vortical structures have similar characteristics for all wings at the beginning of the motion, the vortical structures start to be distinguished from each other after approximately 2.4 chord lengths of travel because of the different deformation characteristics of the wing models. The closest LEV to the wing surface is obtained on the wing without stiffener, which has the maximum camber generation because of its highly chordwise

flexibility. The wing with 90° of stiffener produces the highest LEV circulation, whereas the wing without stiffener generates the lowest one. This study shows that the optimum wing structure that offers the best flight performance in terms of aerodynamic efficiency can be manufactured by using 3D printing technology for predefined flapping-wing micro aerial vehicle operations.

Keywords: Particle image velocimetry, Leading-edge vortex, Flexible wing, Stiffener, 3D printer, Micro aerial vehicles

ÖZ

FARKLI YÖNLERDE DESTEK ÇUBUKLARINA SAHİP ESNEK KANATLARIN DOĞRUSAL HAREKET BOYUNCA AKIŞ KARAKTERİSTİĞİNİN DENEYSEL OLARAK İNCELENMESİ

Karakaş, Hasan Halil
Yüksek Lisans, Havacılık ve Uzay Mühendisliği
Tez Yöneticisi: Dr. Öğr. Üyesi Mustafa Perçin

Ağustos 2022, 106 sayfa

Bu çalışma, önce durağan durumdan sabit ivme ile hızlanan, daha sonra sabit hızla doğrusal bir hareket gerçekleştiren kanatlar etrafındaki akış alanını deneysel olarak incelemektedir. Farklı yönlerde eğilme sertliğine sahip kanatlar incelenecektir. Bu sertlik, kanat üst yüzeyine hücum kenarı ile farklı açılara sahip sertliği artırıcı çubuklar (ing., stiffener) yerleştirilerek sağlanmıştır. Deneyler sekizgen profile sahip bir su tankında yapılmıştır ve iki boyutlu iki bileşenli parçacık görüntülemeli hız ölçme tekniği (2D2C PIV) kullanılarak, düzlemsel akış alanları elde edilmiştir. PIV ölçümleri, hareketin ilk anlarında deneyde test edilen kanatların tümü için kararlı hücum kenarı girdabı oluştuğunu ve bu girdabın uzun bir hareket süresi boyunca kararlılığını koruduğunu göstermektedir. Yaklaşık 2.4 veter boyu hareket boyunca, akış alanları tüm kanatlar için oldukça benzerdir. Fakat 2.4 veter boyu hareketten sonra, girdap yapılarının farklı deformasyon karakteristikleri sebebiyle farklılaştığı gözlemlenmiştir. Kanat yüzeyine en yakın hücum kenarı girdabı, en yüksek kambur büyüklüğüne sahip destek çubuksuz kanat etrafında gözlemlenmiştir. 90° destek çubuklu kanat, en yüksek geometrik hücum kenarı ile hareket ederek en büyük hücum kenarı girdabı sirkülasyonunu üretirken destek çubuksuz kanat ise, en küçük hücum kenarı girdabı sirkülasyonuna sahiptir. Bu çalışmanın sonucunda, 3 boyutlu

yazıcı teknolojisi kullanılarak önceden planlanmış bir çırpan kanatlı mikro insansız hava araçları operasyonları için aerodinamik verimlilik açısından en iyi uçuş performansına sahip kanatların üretilebileceği de görülmüştür.

Anahtar Kelimeler: Parçacık görüntülemeli hız ölçme, Hücüm kenarı girdabı, Esnek kanat, Destek çubuğu, 3 boyutlu yazıcı, Mikro insansız hava araçları

To my dear family and my lovely cat

ACKNOWLEDGMENTS

First, I would like to express my deepest gratitude to my supervisor Asst. Prof. Dr. Mustafa Perçin for his kind and patient guidance throughout my thesis process. His suggestions and experience on this subject helped me a lot to complete my thesis. I am so grateful to him for this innovative and exciting topic that he proposed to me.

I would like to thank my thesis jury members Prof. Dr. Mehmet Metin Yavuz, and Prof. Dr. Sinan Eyi, Assoc. Prof. Dr. Munir Elfarra and Asst. Prof. Dr. Halil Ersin Söken for the positive and constructive feedback they shared with me so that I could complete my thesis in a better way.

I would like to appreciate Mahdi Yazdanpanah and Tuğrul Akpolat for sharing their knowledge and experience in the experimental setup with me.

I would like to thank RUZGEM for allowing me to study in their laboratory and use their 3D printer.

I would like to express my sincere thanks to my dear English teacher, dear friend Mr. Steve Joseph Riva, who supported me during my thesis process and is still trying to teach me English, for sharing his knowledge and life experiences with me.

I also would like to thank my dear friends Mert Kaan Varış and Muhammed Ahmed Akyol, Hakan Yurtseven, and Utku Can Tuğutlu for their encouragement and unlimited support in my troubled times. My thesis process has become more enjoyable thanks to them.

I would like to express my endless gratitude to my darling Çağıl Ezgi Aydemir, for showing me her beautiful love and helping me conduct my experiments. Without her, I could not have had a chance to complete my thesis. I'm so lucky to know her and have her in my life.

I would like to express my eternal gratitude to Mmin Karakaş, Nilfer Karakaş, and Gke Karakaş for all the opportunities they have provided for me and for their endless love. They have always been by my side and always supported me. Whenever I called, there was always a phone that was answered and no matter how stressful the situation they always positively calmed me and helped me.

Finally, I would like to express my deepest gratitude to my best friend and lovely cat Morty, for showing me your unlimited and unconditional love and psychological support during my thesis process. Every day, you woke me up early in the morning allowing me to start the day early and helped me work late into the night by wanting to play until midnight thanks to your unlimited energy. Thank you for everything Morty. I am glad you are in my life, and we will have many more beautiful adventures together. I also want to thank our family cats Sherlock, Leo and Nazlı for being with us, showing us their love and being a good friend of Morty.

TABLE OF CONTENTS

ABSTRACT	v
ÖZ.....	vii
ACKNOWLEDGMENTS.....	x
TABLE OF CONTENTS	xii
LIST OF TABLES	xv
LIST OF FIGURES	xvi
LIST OF ABBREVIATIONS	xix
LIST OF SYMBOLS.....	xx
CHAPTERS	
1 INTRODUCTION.....	1
2 FLAPPING-WING AERODYNAMICS.....	7
2.1 Micro Aerial Vehicles (MAVs) & Flapping Wings	7
2.2 Force Generation Mechanism in Flapping-Wing Flight.....	8
2.2.1 Leading-Edge Vortex Formation (Delayed Stall)	10
2.2.2 Rotational Forces.....	13
2.2.3 Wake Capture	14
2.2.4 Clap and Fling	15
2.2.5 Added Mass	16
2.3 Wing Flexibility.....	17
2.3.1 Spanwise Wing Flexibility	18

2.3.2	Chordwise Wing Flexibility.....	19
3	EXPERIMENTAL METHODS & MANUFACTURING	27
3.1	Water Tank.....	27
3.2	Robotic Arm.....	28
3.3	Wing Models	29
3.4	Wing Flexibility	30
3.5	Manufacturing Method.....	32
3.6	Motion Kinematics.....	37
3.7	Flow Field Measurements via Particle Image Velocimetry	39
3.7.1	Field of View and Imaging	39
3.7.2	Illumination.....	40
3.7.3	External Trigger Mechanism	42
3.7.4	Seeding.....	43
3.7.5	Flow Condition	44
3.7.6	Image Acquisition.....	44
3.8	Data Processing	45
3.8.1	Calibration.....	45
3.8.2	Image Pre-Processing.....	47
3.8.3	Vector Calculations (Processing).....	50
3.9	LEV & TEV Circulation	52
3.10	LEV & TEV Centroid Detection Method.....	52
3.11	Analysis of Measurement Errors	54
3.11.1	Uncertainty in Velocity Vectors	54
3.11.2	Uncertainty in the LEV & TEV Circulation	55

3.11.3	Uncertainty in LEV & TEV Centroid	56
3.11.4	Accuracy of Robotic Arm	60
4	RESULTS AND DISCUSSION.....	61
4.1	Geometric Angle of Attack.....	61
4.2	Camber Generation	64
4.3	Flow Characteristics	68
4.4	LEV & TEV Characteristics	79
4.4.1	LEV Circulation	79
4.4.2	TEV Circulation	82
4.4.3	LEV Position	84
4.4.4	TEV Position	87
4.5	Comparison with previous studies.....	90
5	CONCLUSION	97
	REFERENCES.....	103

LIST OF TABLES

TABLES

Table 3.1 Wing Size Parameters	29
Table 3.2 Structural Properties of Wing w/o Stiffener	30
Table 3.3 Stiffener Parameters.....	31
Table 3.4 Printing Parameters.....	34
Table 3.5 Motion Kinematics.....	38
Table 3.6 The Components of illumination.....	42
Table 3.7 Uncertainty Values.....	59

LIST OF FIGURES

FIGURES

Figure 1.1. Maximum lift coefficient for steady and unsteady flows versus Reynolds number (Jones and Babinsky, 2010)	2
Figure 2.1. Micro aerial vehicles (MAVs), a) Fixed-wing MAVs, b) Rotary-wing MAVs, c) Flapping-wing MAVs (Adapted from Percin, 2015)	7
Figure 2.2. Schematic of an insect (Adapted from Sane, 2003).....	8
Figure 2.3. General flapping patterns (Adapted from Sane, 2003)	9
Figure 2.4. Phases of insect wing motion (Adapted from Sane, 2003).....	9
Figure 2.5. LEV motion in 2D translating and 3D revolving motions (Sane, 2003)	11
Figure 2.6. Correlation between LEV and TEV circulation (Yazdanpanah, 2019)	12
Figure 2.7. Rotational forces (Adapted from Sane, 2003)	14
Figure 2.8. Wake capture effect (Adapted from Sane, 2003).....	15
Figure 2.9. Clap and fling mechanism.....	16
Figure 2.10. Added mass effect.....	17
Figure 2.11. Effect of spanwise flexibility on phase lag and wing tip displacement (Adapted from Heathcote et al., 2008)	18
Figure 2.12. Effect of spanwise flexibility on thrust coefficient (Heathcote et al., 2008).....	19
Figure 2.13. Influence of chordwise flexibility on force generation (Zhao et al., 2009).....	20
Figure 2.14. Effects of chordwise flexibility on the geometric angle of attack (Zhao et al., 2011).....	21
Figure 2.15. Variation of LEV magnitude and net force coefficient as the chordwise flexibility increases (Zhao et al., 2009).....	21
Figure 2.16. LEV position (Adapted from Yazdanpanah, 2019)	22
Figure 2.17. The twist mechanism of leading-edge and stiffener (Ennos, 1988)....	23
Figure 2.18. Wing with one of three stiffener configurations (Zhao et al., 2011)...	24

Figure 2.19. Lift versus drag coefficient graph for wings with different stiffener orientations (Zhao et al., 2011)	24
Figure 2.20. Schematic of chordwise deformation and LEV generation of the wings with different stiffener orientations (Zhao et al. 2011).....	25
Figure 2.21. PIV image of wings with different stiffener orientations (Zhao et al. 2011)	25
Figure 3.1. Experimental setup	27
Figure 3.2. Robotic arm	28
Figure 3.3. Schematic of wing models, a) Wing w/o stiffener, b) Wing w/ 30° Stiffener, c) Wing w/ 60° Stiffener, d) Wing w/ 90° Stiffener	29
Figure 3.4. Raise 3D Pro Plus	32
Figure 3.5. Rough surface and wing model	33
Figure 3.6. Printing the rough surface	33
Figure 3.7. Two parts of the wing structure	34
Figure 3.8. Defective wing and well-printed wing	35
Figure 3.9. Wing size measurement.....	35
Figure 3.10. Wing fixture.....	36
Figure 3.11. Printed wing models a) Wing w/o stiffener, b) Wing w/ 30° Stiffener, c) Wing w/ 60° Stiffener, d) Wing w/ 90° Stiffener	37
Figure 3.12. Motion kinematics	38
Figure 3.13. PIV cameras.....	39
Figure 3.14. Schematic of the field of view.....	40
Figure 3.15. Spherical and cylindrical lenses and laser source.....	41
Figure 3.16. Magnets and magnetic hall effect sensor.....	43
Figure 3.17. Seeding particles.....	44
Figure 3.18. LEV centroid positions for different number of samples	45
Figure 3.19. Laser sheet at the 75% wingspan.....	46
Figure 3.20. Focusing the PIV cameras	46
Figure 3.21. Stitched calibration image	47
Figure 3.22. Steps of pre-processing.....	49

Figure 3.23. Steps of vector calculation	51
Figure 3.24. Robotic arm displacement error at each stage of the motion	60
Figure 4.1. Geometric angle of attack	61
Figure 4.2. Variation of the geometric angle of attack.....	62
Figure 4.3. Wing camber	65
Figure 4.4. Variation of camber generation.....	66
Figure 4.5. Curve-fitted version of variation of camber generation.....	67
Figure 4.6. Out-of-vorticity contour	74
Figure 4.7. Velocity contours and streamlines	78
Figure 4.8. LEV circulation.....	79
Figure 4.9. Variation of LEV circulation	80
Figure 4.10. TEV circulation.....	82
Figure 4.11. Variation of LEV & TEV Circulation.....	83
Figure 4.12. LEV centroid.....	84
Figure 4.13. Variation of the LEV Centroid in the y-axis.....	84
Figure 4.14. Variation of the LEV Centroid in the x-axis.....	85
Figure 4.15. The total distance between the LEV centroid and the leading edge ...	86
Figure 4.16. Variation of the distance between the LEV centroid and the leading edge.....	86
Figure 4.17. TEV centroid.....	87
Figure 4.18. Variation of the TEV Centroid in the y-axis.....	88
Figure 4.19. Variation of the TEV Centroid in the x-axis.....	89
Figure 4.20. The total distance between the TEV centroid and the LE.....	89
Figure 4.21. Variation of the distance between the TEV Centroid and the trailing edge.....	90
Figure 4.22. a) Variation of camber generation in magnitude, b) Variation of resultant force coefficient during the revolving motion (Adapted from Meerendonk, 2016).....	93

LIST OF ABBREVIATIONS

ABBREVIATIONS

2D 2C	Two-dimensional two-component
2D PIV	Two-dimensional particle image velocimetry
PIV	Particle image velocimetry
AOA	Angle of Attack
AR	Aspect ratio
CCD	Charge-coupled device
FDM	Fused Deposition Modeling
FOV	Field of view
MAVs	Micro Aerial Vehicles
LE	Leading edge
TE	Trailing edge
LEV	Leading-edge vortex
TEV	Trailing edge vortex
Nd:YAG	Neodymium-doped yttrium aluminum garnet (Nd:Y ₃ Al ₅ O ₁₂)
PLA	Polylactic Acid
METU	Middle East Technical University

LIST OF SYMBOLS

SYMBOLS

γ_1, γ_2	Two-dimensional vortex centroid, boundary detection criterion
ν	Poisson ratio
δ^*	Chord length of travel
α	Angle of attack [deg]
V_t	Terminal velocity [m/s]
ρ	Density [kg/m ³]
T	Temperature [°C]
x, y, z	Directions in x, y and z axes [m]
ω	Vorticity [1/s]
Γ	Circulation [m ² /s]
Γ^*	Dimensionless circulation
c	Chord [m]
b	Wingspan [m]
t	Time [s]
E	Young's modulus [N/m ²]
h	Thickness [m]
Π_1	Stiffness parameter
EI	Flexural stiffness [Nm ²]
C_L, C_D	Lift, drag coefficients
L/D	Lift to drag ratio

CHAPTER 1

INTRODUCTION

Natural fliers have always been inspirational for human beings who are interested in airborne machines. Although the initial attempts at flight in history were on trial by bird-inspired mechanical systems, the flapping-wing aerodynamics, which requires high-tech experimental and computational systems to have extensive knowledge about its mechanism, remained as a mysterious topic in the literature because of the insufficient technology. However, with a recent interest in the field of micro aerial vehicles (MAVs), the flapping-wing aerodynamics regained attention in the last two decades, since the rotary and fixed wings are relatively unfavorable in terms of maneuverability and flight efficiency in low Reynolds number flight regimes (Percin, 2015). In Figure 1.1, the maximum lift coefficient $c_{L_{Max}}$ versus the corresponding Reynolds numbers obtained from previous experiments, which include a wide range of cases from studies on hovering insects in unsteady flow to smooth airfoils in a steady flow, is shown. The figure is colored in a way such that the unshaded region represents the experiments in unsteady flow, whereas, the remaining part, corresponds to experiments in a steady flow. According to Figure 1.1, for the steady flow case, it is obvious that the airfoils which have a smooth surface showed acceptably good performance at high Reynolds numbers. In low Reynolds numbers flight regimes, however, although the insect wing structures are used, the performance is still decreased. For the unsteady flow case, on the other hand, the lift coefficient is enhanced significantly as the flapping-wing motion is presented. Moreover, with the help of the leading-edge vortex formed in the progress of the dynamic stall, the maximum lift coefficient is obtained at a very low Reynolds number where $Re = 10^2$ (See Chapter 2.1). It is clear that, in the low Reynolds number flight regime, especially in unsteady flows, the flapping-wing aerodynamics is more favorable than its conventional counterparts (i.e., rotary-wing and fixed-wing

aerodynamics) in terms of force generation. On the contrary, the flapping-wing flight consists of unconventional and unsteady force generation mechanisms (See chapter 2).

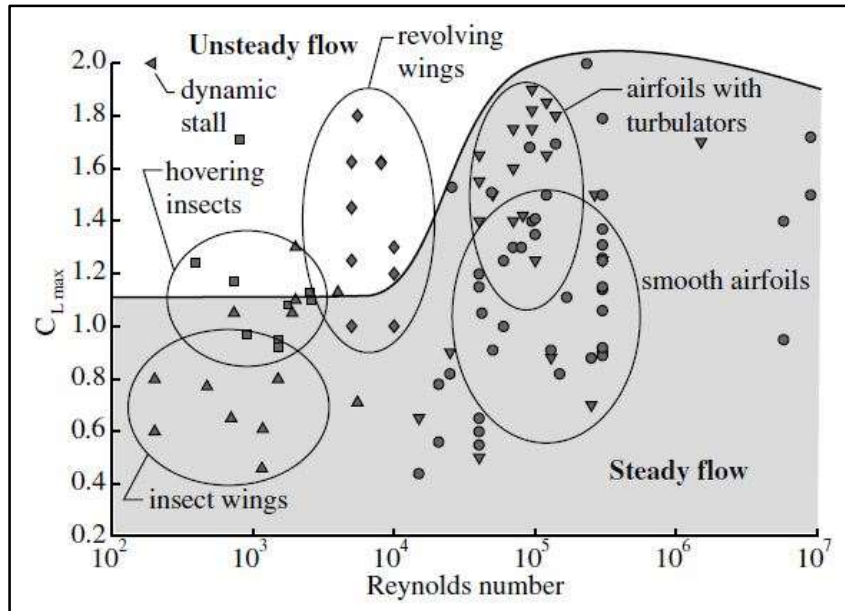


Figure 1.1. Maximum lift coefficient for steady and unsteady flows versus Reynolds number (Jones and Babinsky, 2010)

For aerodynamic force generation, the formation of a stable leading-edge vortex is the main mechanism that is observed in most of the unsteady aerodynamic mechanisms in insect flight (Sane, 2003). The presence of a leading-edge vortex enhances the lift force generation by increasing the circulation around the wing. For three or four chord lengths of travel, this enhancement may be retained before the vortex breakdown or complete detachment from the surface occurs (Ellington et al., 1996). Moreover, thanks to the stable leading-edge formation, without stalling the flapping wings can translate at a higher angle of attack (Zhao et al., 2011). Therefore, because of its importance in force generation, the stability of the leading-edge vortex has been subject to a great number of numerical and experimental studies. Thanks to these investigations, several learning outcomes are obtained, which may be beneficial to enlighten the stability phenomena. Tip vortex, for example, induces a downwash that limits the growth of the leading-edge vortex, which prevents it from

the burst, by lowering the effective angle of attack (Birch and Dickinson, 2001). In addition, for revolving wings moving at low Rossby numbers, the centripetal and Coriolis accelerations are the fundamental mechanisms that underlie the stability, whereas at high Rossby numbers the angular acceleration is the key factor (Lentink et al., 2009). That is, the stability of the leading-edge vortex can be maintained by a spanwise flow reducing the momentum of the flow in a chordwise direction, in which the leading-edge vortex remains smaller allowing the flow to reattach to the surface with ease. As a result, the wing never stalls in a revolving motion. (Ellington et al., 1996). For wings in linear translation where there is no spanwise flow on the wing surface, on the other hand, until the flow reattachment is no longer possible the leading-edge vortex keeps growing in size (Sane, 2003). In this case, the leading-edge vortex bursts as it reaches its maximum size or sheds into the wake, which results in a sudden drop in lift force (i.e., stall) increase in drag. However, the growth of the leading-edge vortex can be modulated by introducing wing flexibility, which makes flapping-wing aerodynamics more complicated (Combes and Daniel, 2002).

Therefore, several experimental and numerical studies are carried out in the literature to investigate the effects of wing flexibility on aerodynamic force generation during the flapping-wing motion. These studies can be divided into two main topics, which are spanwise flexibility and chordwise flexibility. The spanwise flexibility changes the net flow direction by affecting the resulting flapping velocity in the spanwise direction, which results in a change in the net flow direction along the wingspan. (Yang et al., 2012). The excessive spanwise flexibility causes large phase differences between the wing root and tip, which results in a weak vorticity pattern decreasing the thrust force generation. The suitable range of spanwise flexibility, however, could enhance the mean and instantaneous thrust forces of a plunging wing because of the wing deformation (Aona et al., 2009). Chordwise flexibility, on the other hand, can be achieved by a rigid leading edge, which prevents bending in the spanwise direction, and a flexible wing surface, which provides deformation in the chordwise direction. Wings with chordwise flexibility produce lower lift and drag force compared to their rigid counterparts since the chordwise flexibility of the wing

directly influences the leading-edge vortex and thereby the force generation (Zhao et al., 2011). That is, unlike rigid wings, the wings with chordwise flexibility realign with the flow direction, which reduces the effective angle of attack. The reduction in the effective angle of attack provides smaller TEV formation to re-establish the Kutta condition, which results in smaller LEV formation. Therefore, it can be concluded that the LEV circulation increases as the bending stiffness in the chordwise direction increases, enhancing the aerodynamic force generation. In addition, as the wing flexibility increases, because of the lowered geometric angle of attack, the net force vector is tilted more towards the lift direction (Zhao et al., 2011). Compliant trailing-edge to the upcoming flow, allows the wing to realign in the flow direction with ease, which results in smaller leading-edge vortex formation preventing LEV from bursting (Yazdanpanah, 2019). In addition, because of the stable LEV formation, the flow re-attachment before the trailing edge is observed, which results in less chaotic wake formation.

Note that, an aerodynamic force applied at a point, which has some distance between the torsional axis of the wing, causes it to twist with an angle, especially at the leading edge (Ennos, 1988). This twist is transmitted to the stiffener, which is connected to the leading edge with an angle, of the same magnitude but in an opposite direction. That is, if the leading-edge pronates, the stiffener supinates. The twist in the stiffener results in the camber generation in the chordwise direction because of the deformation in the wing membrane in the upward direction. According to Ennos (1988), camber generation is a function of the twist angle of the leading edge, the wing chord length, and the angle between the stiffener and the leading edge. The camber generation is inversely proportional to the angle between the stiffener and the leading edge and proportional to the chord length and angle of the leading-edge twist. For example, if the angle between the stiffener and the leading edge is zero degrees (i.e.: parallel), maximum camber generation in magnitude will be observed, whereas minimum camber generation in magnitude will be obtained when the angle between the stiffener and the leading edge is 90 degrees (i.e., perpendicular). An increase in camber in the positive direction enhances the

circulation around the leading edge, which results in bigger and stronger leading-edge vortex formation (Zhao et al., 2011). As a result, the wing generates a higher lift force.

Note that, in the literature, the influence of stiffeners on flapping wing aerodynamics is studied by a few stiffeners placed on the wing surface. In these studies, stiffeners are constructed with rigid materials, which prevent stiffeners from any deformation and are glued on the flexible wing membrane. However, to investigate the effect of stiffener orientation on the flow field around the wing comprehensively, numerous stiffeners should be well-integrated on the wing surface and the deformation characteristics of the stiffeners should also be considered, which requires advanced production techniques. In this respect, 3D printing technology offers an enormous opportunity to manufacture complex wing structures with a low tolerance in production in a short time (Ahmed et al., 2016).

This thesis has two objectives:

1. To produce 3D-printed wings, which are flexible in chordwise direction and rigid in the spanwise direction, with and without differently oriented stiffeners that are well-integrated on the upper surface of the wings and have deformation capabilities.
2. To investigate the influence of the stiffener orientation on the flow field around the translating wing and LEV characteristics.

Therefore, 2D2C-PIV measurements were conducted around one wing without a stiffener, and three wings with different stiffener orientations, which are 30, 60, and 90 degrees with the leading edge, and according to the results the wings were compared with each other.

This thesis is divided into five chapters. In chapter 1, a brief introduction and related studies carried out in the literature are given. In chapter 2, the unsteady force generation mechanisms of flapping-wing aerodynamics and the influence of wing flexibility on force generation are presented. In chapter 3, the experimental setup and

wing manufacturing technique are introduced. In chapter 4, the results of this study are presented and discussed in detail. Finally, in chapter 5, the conclusion of this thesis is given.

CHAPTER 2

FLAPPING-WING AERODYNAMICS

In this chapter, general information about the MAVs and force generation mechanisms of flapping-wing aerodynamics is explained. In addition, the influence of wing flexibility on aerodynamic force generation is introduced at the end of this chapter.

2.1 Micro Aerial Vehicles (MAVs) & Flapping Wings

According to the DARPA, which is Advance Research Agency, MAVs could have:

- Maximum weight of 100 grams with a payload of 20 grams,
- Maximum dimensions of 15 cm,
- Maximum endurance time of 60 minutes,
- Maximum flight speed of 15 m/s.

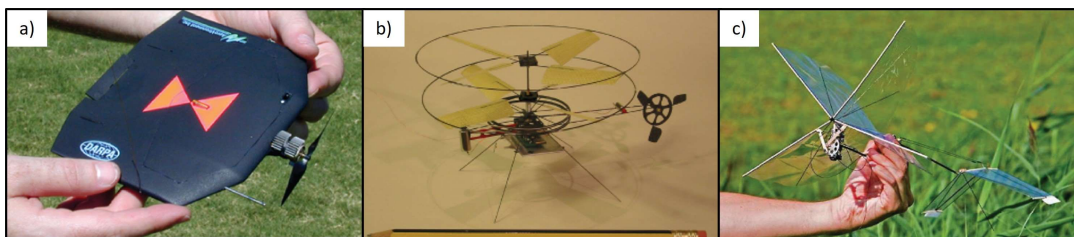


Figure 2.1. Micro aerial vehicles (MAVs), a) Fixed-wing MAVs, b) Rotary-wing MAVs, c) Flapping-wing MAVs (Adapted from Percin, 2015)

The low-speed flow regime and unmanned flight capability of MAVs make them favorable for several military and commercial missions including surveillance or assistance indoor operations, which may be dangerous for human beings. The MAVs can be distinguished in three distinctive design approaches (Figure 2.1). These are fixed wings, which have a low lift-to-drag ratio due to high tip vortices because of

wings with low aspect ratio, rotary wings, which have high noise and low energy consumption efficiency because of higher rotor speeds, and flapping wings, which have exceptional performance in low Reynolds number flight regime as aforementioned (Percin, 2015). Moreover, flapping wings have advanced maneuverability capabilities such as:

- hovering,
- backward and inverted flight,
- taking off and landing upside down.

2.2 Force Generation Mechanism in Flapping-Wing Flight

Similar to the fixed wing aerodynamics, the section between the LE and TE of the wing is named as wing chord whereas the distance between two wing tips is identified as wing span. The ratio of wing span to the mean chord length is called wing aspect ratio and it is often taken as two (Sane, 2003).

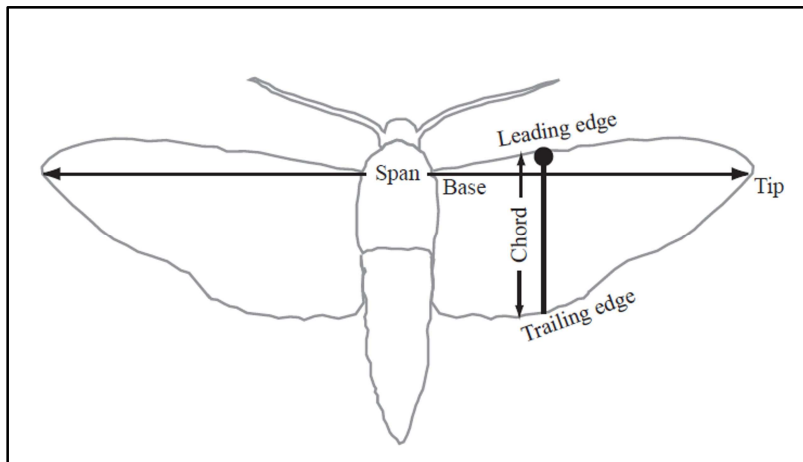


Figure 2.2. Schematic of an insect (Adapted from Sane, 2003)

Note that, the geometric angle of attack, α is the relative angle between the direction of the free stream and the angle of attack, whereas the effective angle of attack, α' is the relative angle between the locally deflected freestream and the angle of attack. Since expressing the deflection of the freestream due to downwash is not an easy

process, the geometric angle of attack is preferred in most flapping-wing studies (Sane, 2003).

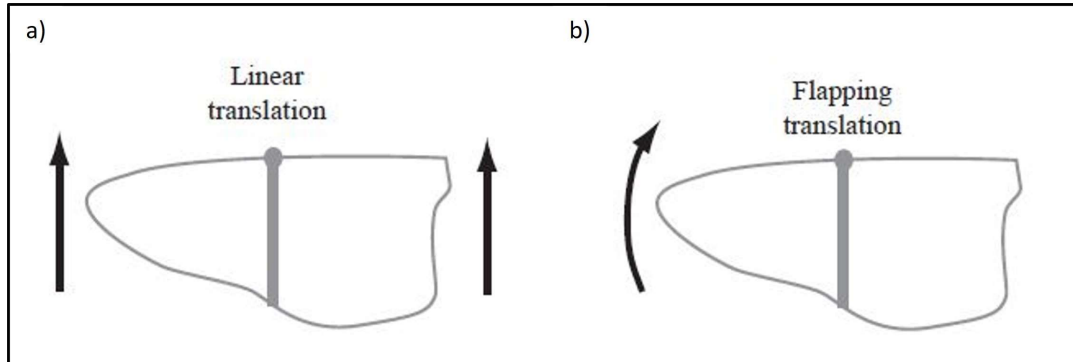


Figure 2.3. General flapping patterns (Adapted from Sane, 2003)

In general, the motion of the insect wings can be expressed in two general flapping patterns such as linear translation and flapping translation. In linear translation (Figure 2.3 a), both wing root and tip move together, whereas, in flapping translation (Figure 2.3 b), wing tip rotation around a fixed point at the wing root occurs. The ventral to the dorsal movement of the wing is called upstroke, whereas the dorsal to the ventral motion of the wing is named downstroke (Figure 2.4).

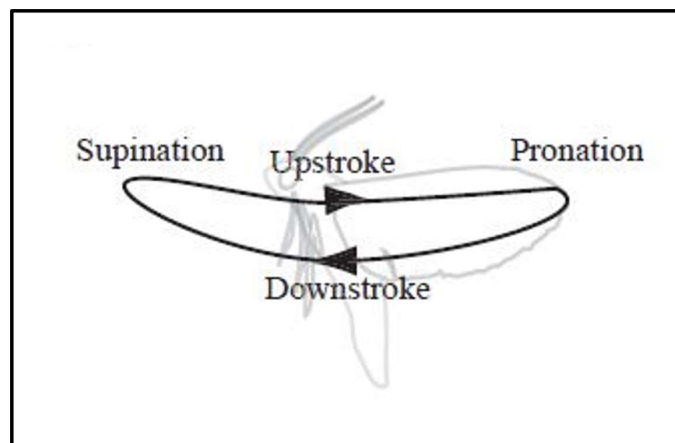


Figure 2.4. Phases of insect wing motion (Adapted from Sane, 2003)

The 3D motion of the wing during the flapping can be decomposed as pitching, plunging, and sweeping. In pitching motion, to preserve a positive angle of attack the wing pronates or supinates. That is, during the transition from upstroke to

downstroke, wing pronation, in which the ventral side of the wing faces upward, occurs, whereas, during the transition from downstroke to upstroke, a wing supinates, in which the dorsal side of the wing looks downward. The up and down motion of the wing, on the other hand, is called plunging (heaving), whereas the back and forth motion of the wing is named sweeping motion. These movements together form the flapping movement (Sane, 2003).

In addition, unlike the other two design approaches, the flapping-wing flight consists of unconventional and unsteady force generation mechanisms. When a wing at an angle of attack starts moving from rest impulsively, the steady-state value of the circulation cannot be attained immediately (Walker, 1931). During this motion, the vorticity generated at the trailing edge, named a trailing-edge vortex, starts rolling up and forming a starting vortex, which induces a velocity field around the wing that prevents the bound circulation from growing. As soon as the distance between the starting vortex and the trailing edge becomes sufficiently large, the wing reaches its steady-state circulation. This phenomenon is called the Wagner effect (Wagner, 1925). Note that, the Wagner effect is neglected in most of the recent flapping-wing models, while the other unsteady effects are focused on (Sane, 2003).

Some of the unsteady flapping flight mechanisms providing favorable and effective force generation at low Reynolds numbers are as follows:

1. Leading-edge vortex formation (delayed stall)
2. Rotational forces
3. Wake capture
4. Clap and fling
5. Added mass

2.2.1 Leading-Edge Vortex Formation (Delayed Stall)

When a wing impulsively starts to its motion at an angle of attack greater than its stall angle, then a large transient vortex forms at the leading edge which creates a

suction region, resulting in a dramatic increase in lift force generation. Moreover, the leading-edge vortex generation is the primary force generation mechanism in flapping-wing aerodynamics, and its size and strength are related to the size and strength of the trailing-edge vortex (See Figure 2.6). The presence of a leading-edge vortex enhances lift force generation by being attached to the bound vortex core, which increases circulation around the wing (Sane, 2003). The behavior of LEV differs in 3D revolving and 2D translating motion, which is illustrated in Figure 2.5.

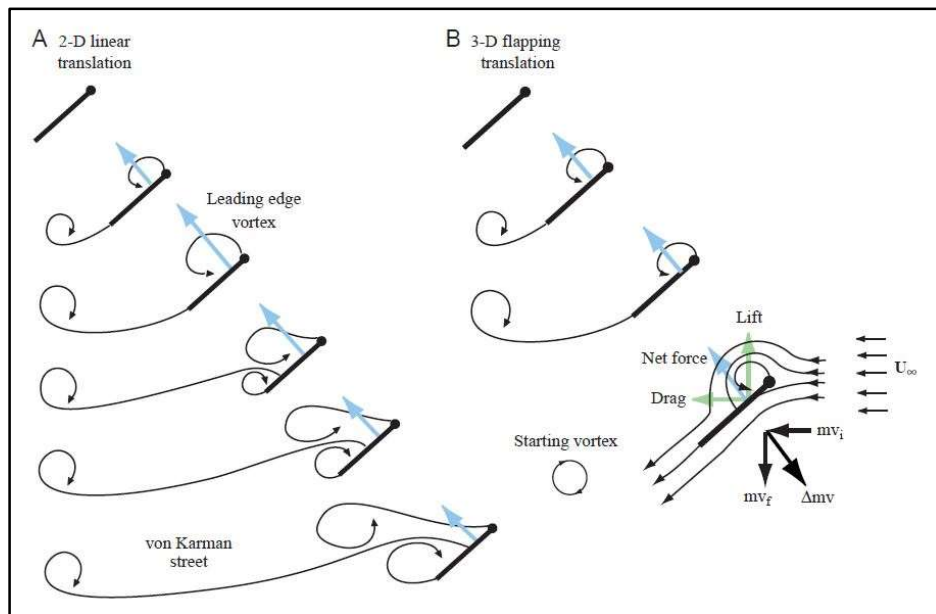


Figure 2.5. LEV motion in 2D translating and 3D revolving motions (Sane, 2003)

For 3D revolving wings, the attachment of the LEV to the wing surface is prolonged because of the spanwise flow from the wing tip to approximately 75% of the wing span, where the LEV is detached from the wing surface. Therefore, the shed of the LEV is prevented for many chord lengths of travel, in which the formation of von Karman vortex street no longer exists. In these circumstances, the wing stall is eliminated (Ellington, 1996). Moreover, during the revolving motion, the momentum of the flow in the chordwise direction is reduced because of the spanwise flows on the wing surface that redirect momentum transfer in the spanwise direction. Therefore, a smaller leading edge is formed providing easier flow re-attachment to

the surface, and the re-attachment can be maintained for a longer time (Maxworthy 1979).

For 2D translating wings, on the other hand, until the flow re-attachment is no longer possible, the leading-edge vortex grew in size as the wing keeps translating at a high angle of attack. The LEV bursts into smaller pieces when it reaches its maximum size, or it sheds into the wake resulting in a sudden drop in the lift force generation. At this point, when the LEV sheds into the wake, the Kutta condition breaks down and a vortex is formed at the trailing edge called the trailing-edge vortex. Note that, at low Reynolds number flights the breakdown of the Kutta condition can be observed by the growth of TEV, which keeps growing until it can no longer be attached to the wing (Dickinson and Götz, 1993). when the trailing-edge vortex is completely detached from the wing, it sheds into the wake a new LEV is formed at the leading edge. This repetitive process ends up forming an alternate vortex pattern with vortices that are counter-rotating with respect to each other called the Karman Vortex Street. This mechanism is called a delayed stall because the lift and drag forces are at their greatest values when the leading-edge vortex is present and the wing stalls when it bursts or sheds into the wake. According to Muijres et al. (2008), the leading-edge vortex can provide 50% of the lift force generated by the wing.

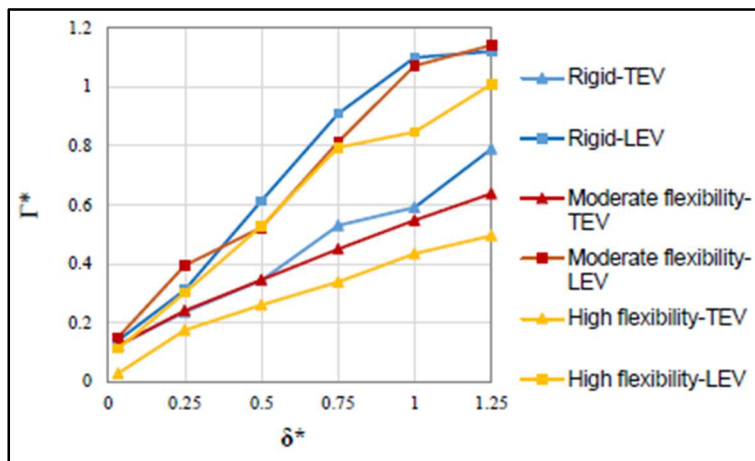


Figure 2.6. Correlation between LEV and TEV circulation (Yazdanpanah, 2019)

Note that, although the first experimental identification of the delayed stall was provided by Walker (1931) on the aircraft wing models that move at an angle of attack greater than its stall angle, the delayed stall in the flapping-wing aerodynamics is firstly introduced by Maxworthy (1979), who observed the LEV on the flinging wing model.

2.2.2 Rotational Forces

To preserve its positive angle of attack during the translational phase of the wing motion, the wing pronates (pitch down) or supinates (pitch up) during the stroke reversals (Sane, 2003). The stagnation point moves away from the trailing edge when the Kutta condition breaks down as the wing starts to rotate about a spanwise axis (Figure 2.7 A). At this instant, to reconstruct the Kutta condition at the trailing edge, additional circulation is produced around the wing, which enhances the lift force generation.

This circulation due to wing rotation is formulated by Fung (1993) theoretically, which states that the strength of additional circulation depends on the axis of rotation and rotational velocity. The formula is given below.

$$\Gamma_{\text{rot}} = \pi (0.75 - x_0) \omega c^2 \quad (2.1)$$

where, Γ_{rot} , x_0 , ω and c represent the rotational circulation, a non-dimensional axis of rotation, rotational velocity, and chord length, respectively.

The wing rotation can be investigated in three different motions. These are:

- **Advanced rotation**, where the wing rotates before the stroke reversal,
- **Delayed rotation**, where the rotation is delayed with respect to the stroke reversal,
- **Symmetrical rotation**, where the simultaneous wing rotation and the stroke reversal occur.

Dickinson et al (1999) state that the greatest lift force generation is observed in the advanced rotation because of an increase in the angle of attack, whereas the delayed rotation produces the lowest lift force due to the lowered angle of attack during the stroke reversal.

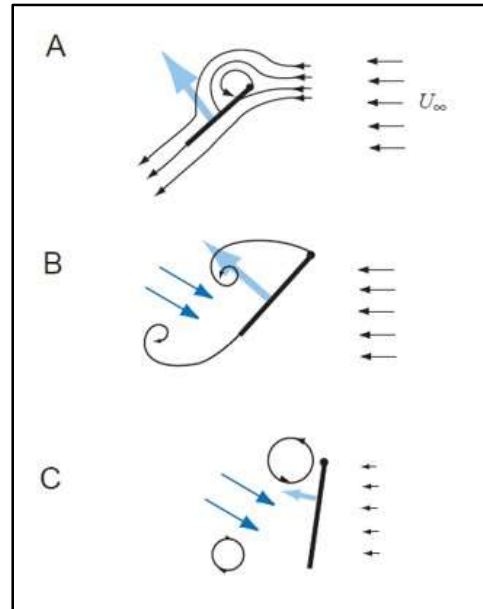


Figure 2.7. Rotational forces (Adapted from Sane, 2003)

2.2.3 Wake Capture

When the wing performs a rotation about a spanwise axis as a preparation of the stroke reversal or translates from a steady-state translation, it generates vorticities at its leading and trailing edges, individually, inducing a strong inter-vortex velocity field, in which orientations and the strength are governed by the position and strength of these two vortices (Figure 2.8 B). When the wing movement direction is reversed, it encounters the accelerated flow field (Figure 2.8 C-D) resulting in an enhancement in the aerodynamic force production immediately after the stroke reversals (Figure 2.8 E-F). This mechanism is called wake capture and is only observed in hovering flights.

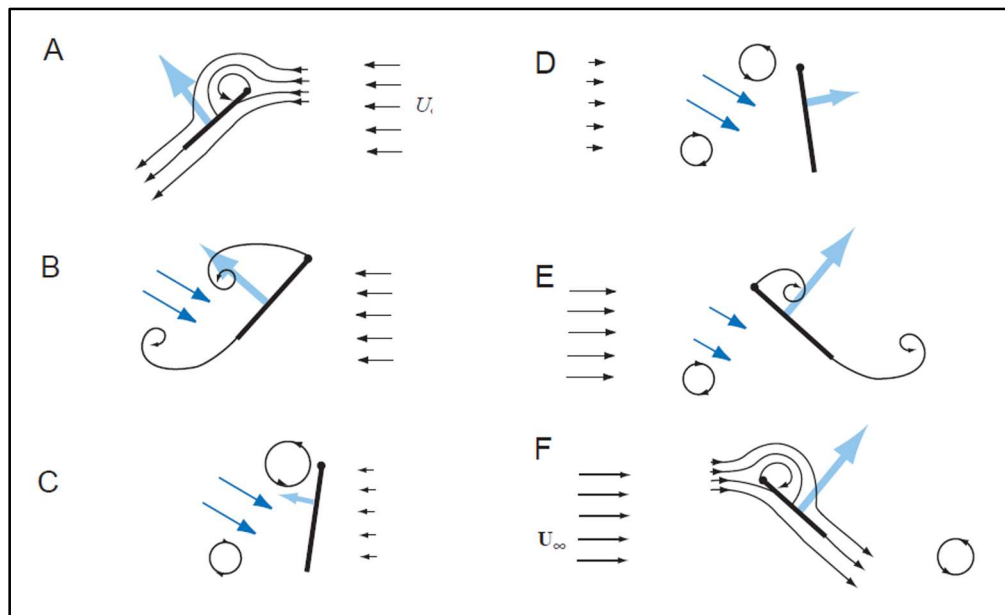


Figure 2.8. Wake capture effect (Adapted from Sane, 2003)

2.2.4 Clap and Fling

Clap and Fling, which is based on wing-wing interactions, is one of the most complex mechanisms in flapping-wing flight enhancing lift force generation. (Weis-Fogh, 1973). It consists of two individual aerodynamic mechanisms, therefore they should be investigated separately (Sane, 2003). The clap and fling mechanism is illustrated in Figure 2.9.

During the clap phase, the leading edges of the wings start approaching each other (Figure 2.9 A). Then pronation about their leading edges occurs until the V-shaped gap between the two wings is closed (Figure 2.9 B). As the trailing-edges touches to each other, the vorticity that is shed from the trailing edge starts rolling up in the form of starting vortex, and it dissipates into the wake. At the end of this phase, the trapped air between the wings is forced to move downwards, hence the downward momentum jet is formed (Figure 2.9 C). As a result, the additional thrust force is generated (Sane, 2003).

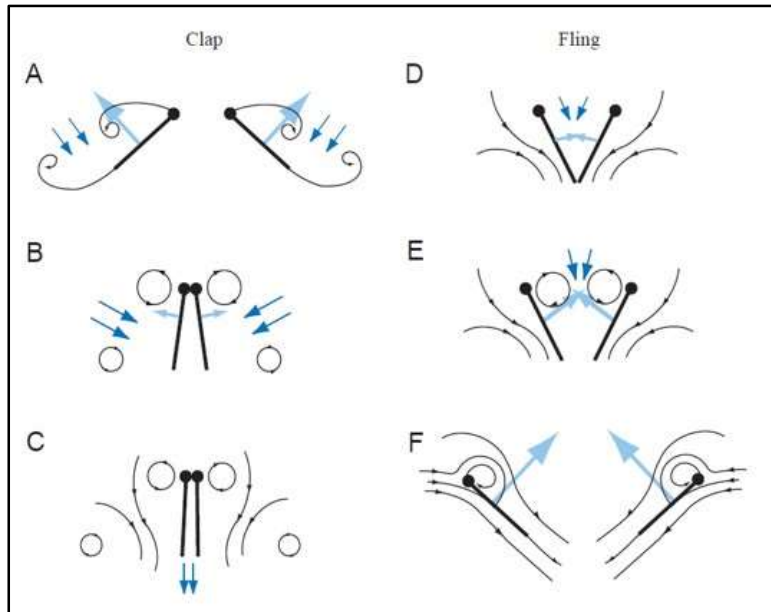


Figure 2.9. Clap and fling mechanism

During the fling phase, on the other hand, the wings perform rotation about their trailing edges that forms a gap between them (Figure 2.9 D). Therefore, a region with low pressure between the wings is created and the surrounding air suddenly moves into this field with a massive leading-edge vortex formation on each wing at the beginning of this phase (Figure 2.9 E). At this instant, oppositely directed trailing-edge vortices vanish themselves suppressing the Wagner Effect (Figure 2.9 F). Therefore, the circulation may be built up more rapidly. In addition, the clap and fling mechanism improves the lift force generation by 25% compared to the conventional flapping-wing motion (Marden 1987).

2.2.5 Added Mass

Unlike aforementioned force generation mechanisms, added mass is a non-circulatory force generation mechanism, which cannot be explained mathematically, which is nothing but a calculation of the changes in the velocity potential around the wing (Sane, 2003). When the wing accelerates with an angle of attack, the fluid around it generates a reaction force to the acceleration, since the fluid around the

wing should also be accelerated as the wing moves. Therefore, the accelerated fluid exerts an inertial-reaction force on the wing, which can be described as an enhancement in the inertia of the flapping wing. According to Ellington (1984), the added mass of an accelerating thin wing can be calculated as the mass of the fluid inside an imaginary cylinder, whose diameter is the wing's chord length (Figure 2.10). The equation is given below.

$$m_{\text{added}} = \frac{1}{4} \rho \pi c^2 \quad (2.2)$$

where, ρ and c represent the fluid density and wing chord length, respectively.

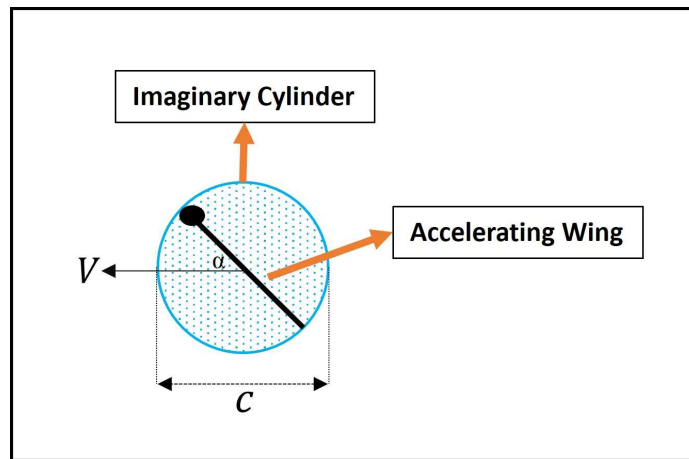


Figure 2.10. Added mass effect

2.3 Wing Flexibility

Several experimental and numerical studies are carried out in the literature to investigate the effects of wing flexibility on aerodynamic force generation during the flapping-wing motion. These studies can be divided into two main topics, which are spanwise flexibility and chordwise flexibility. In general, Combes and Daniel (2003) stated that the wings of the natural fliers are approximately 10 to 100 times more flexible in the chordwise direction than in the spanwise direction.

2.3.1 Spanwise Wing Flexibility

Spanwise flexible wings are rigid in the chordwise direction and deformable in the spanwise direction. The spanwise flexibility affects the resulting flapping velocity along the span direction, which results in a change in net flow direction and hence the effective angle of attack (Yang et al, 2012). To investigate the effects of spanwise flexibility on force generation Heathcote et al. (2008) did an experimental study in a water tank with three wings with different spanwise flexibility in a plunging motion at a Reynolds number of 30000.

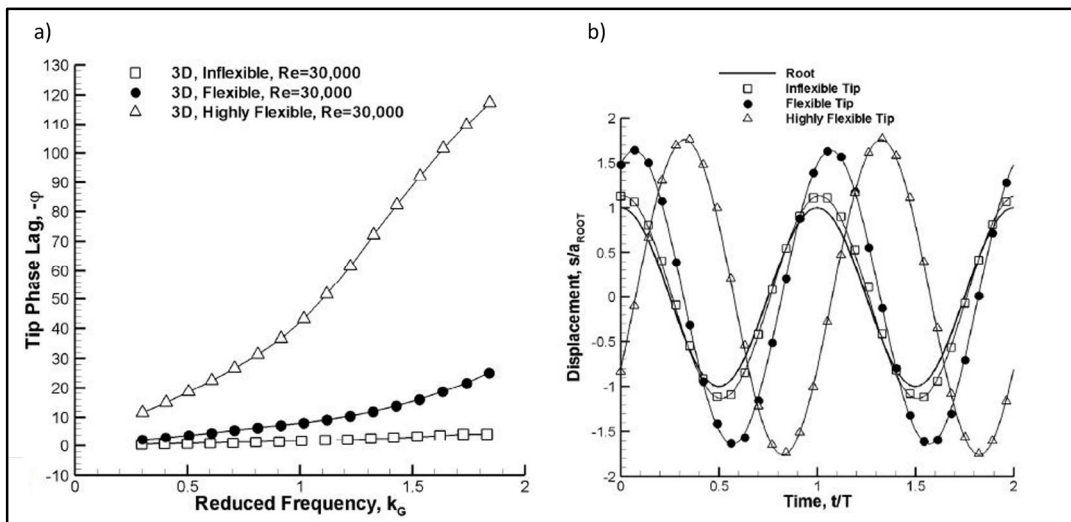


Figure 2.11. Effect of spanwise flexibility on phase lag and wing tip displacement (Adapted from Heathcote et al., 2008)

Their results revealed that the excessive spanwise flexibility of the wing causes large phase differences between the wing tip and root (Figure 2.11 a). This may lead the wing tip and root to start moving in opposite directions (Figure 2.11 b) resulting in oppositely directed vortices formation downstream of the wing tip and root. Therefore, a weak vorticity pattern that decreases the thrust force generation is observed. A wing with intermediate spanwise flexibility, on the other hand, increases the thrust force by approximately 50% compared to its rigid counterpart (Heathcote et al., 2008). The effect of spanwise flexibility on thrust force generation can be seen

in Figure 2.12. When the phase lag is less than 90% between the wing root and tip, the spanwise flexibility provides a favorable effect on thrust generation. That is, a suitable range of spanwise flexibility could enhance the instantaneous and mean thrust force generation by increasing the effective angle of attack at the wing tip (Aona et al, 2009). As a result, the spanwise flexibility should be limited to obtain favorable vortex formation in the span direction.

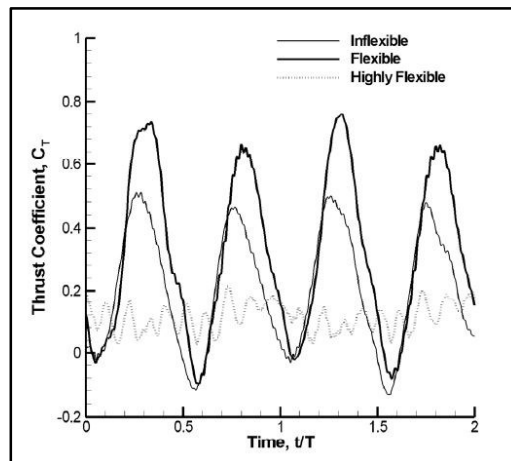


Figure 2.12. Effect of spanwise flexibility on thrust coefficient (Heathcote et al., 2008)

2.3.2 Chordwise Wing Flexibility

Chordwise flexible wings have sufficient bending stiffness in the spanwise direction and are deformable in the chordwise direction. They can be obtained by a rigid leading-edge preventing bending in the spanwise direction and a flexible membrane, which forms the wing surface, providing a flexible trailing edge. In other words, chordwise flexible wings are wings with compliant trailing-edge to the upcoming flow (Heathcote et al, 2004). To investigate the effects of chordwise flexibility on the lift and drag force generation Zhao et al. (2009) did an experimental study with six-teen wings with different chordwise flexibilities in a revolving motion. The difference in chordwise flexibility is provided by different wing membranes.

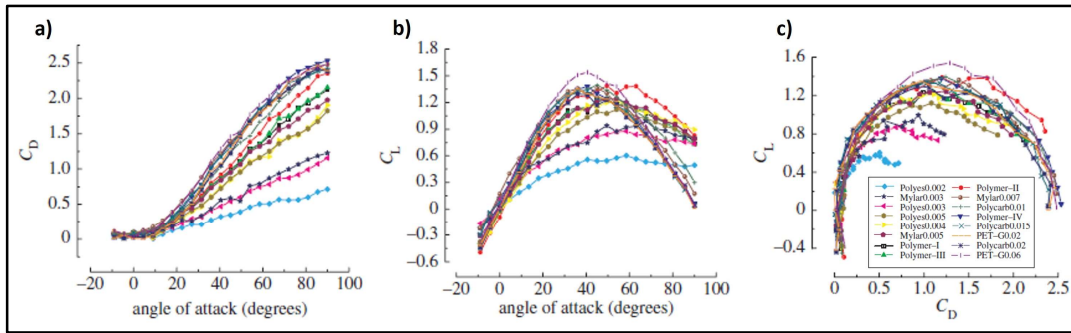


Figure 2.13. Influence of chordwise flexibility on force generation (Zhao et al., 2009)

Their results showed that as chordwise flexibility increases, the lift and drag forces generated decrease monotonically (Figure 2.13 a-b). That is, chordwise flexible wings generate lower lift force compared to their rigid counterparts. However, the lift-to-drag ratio, which is an important parameter for aerodynamic efficiency, increases as the chordwise flexibility increases because of the significant reduction in drag force generation due to the compliant trailing edge to the upcoming flow. Since smaller circulation is required at the trailing edge to establish the Kutta Condition, smaller TEV circulation at the trailing edge, thereby smaller LEV formation, is observed (Zhao et al, 2009). Moreover, in Figure 2.13 b, it is revealed that at an angle of attack greater than 40° , as the angle of attack increases the lift force generated decreases dramatically for rigid wings, whereas it stays almost constant for highly chordwise flexible wings.

In addition, Zhao et al. (2011) stated that as the chordwise flexibility increases, a negative camber generation is observed on the wing surface, since the trailing edge re-aligns in the flow direction with ease, which results in a smaller geometric angle of attack formation. The influence of chordwise flexibility on wing deformation is given in Figure 2.14. Note that, the chordwise flexibility of the wings increases from left to right.

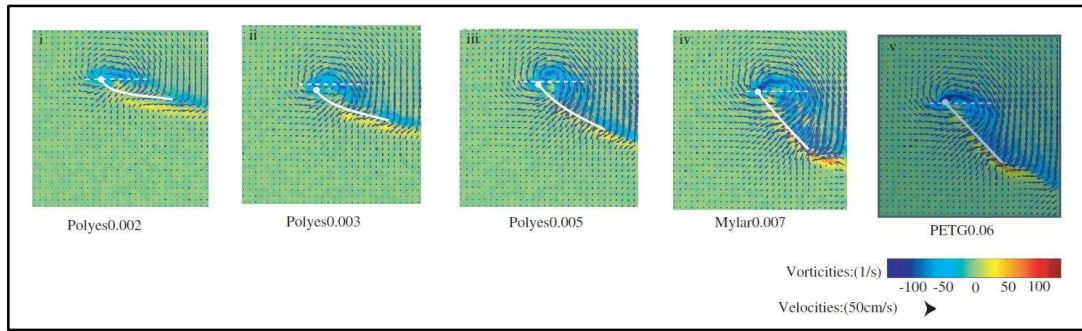


Figure 2.14. Effects of chordwise flexibility on the geometric angle of attack (Zhao et al., 2011)

Moreover, a smaller TEV generation is required to re-establish the Kutta condition because of the reduced geometric angle of attack. Therefore, smaller LEV generation was observed for the wings with high chordwise flexibility. Because of the negative camber formation and smaller LEV generation, the net force produced decreases as the chordwise flexibility increases (Figure 2.15). However, the resultant force vector is tilted more in the lift direction as the chordwise flexibility increases (Zhao et al, 2011).

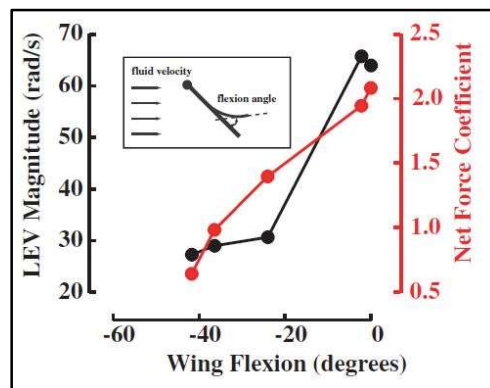


Figure 2.15. Variation of LEV magnitude and net force coefficient as the chordwise flexibility increases (Zhao et al., 2009)

These statements are supported by Yazdanpanah (2019), who did an experimental study with three wings with different chordwise flexibilities in translating motion. He stated that smaller leading-edge vortex generation results in a stable leading-edge

vortex for highly chordwise flexible wings. That is, the LEV on the rigid and moderately flexible wings grows in size, and at a point, they burst into smaller pieces, at which the flow re-attachment is no longer possible. For the highly flexible wing, on the other hand, the growth of the LEV is limited because of the smaller TEV generation as a result of the smaller geometric angle of attack during the motion. Therefore, enhancement in chordwise flexibility prevents the LEV from bursting (Yazdanpanah, 2019). Moreover, the flow re-attaches to the surface since the LEV stays close to the surface during the motion, which results in a less chaotic flow structure in the wake (Figure 2.16).

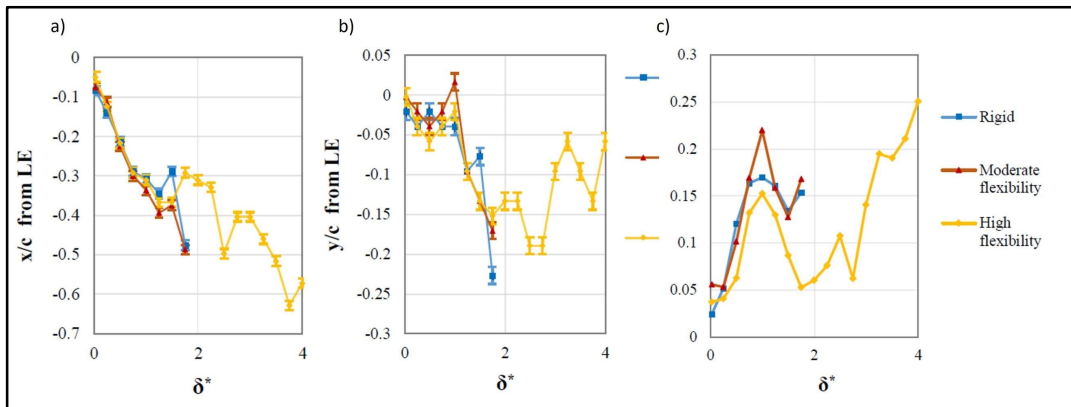


Figure 2.16. LEV position (Adapted from Yazdanpanah, 2019)

According to Vogel (1967) and Dudley (1987), positively cambered airfoils generate higher lift and drag forces with a greater L/D ratio compared to flat ones. Although high chordwise flexibility results in negative camber generation, the camber generated can be increased in the positive direction by additional supports connected to the leading edge with some angle, called stiffeners (Ennos, 1988). Note that, an aerodynamic force applied at a point, which has some distance between the torsional axis of the wing causes it to twist especially on the leading edge. Twist in the leading edge is transmitted to the stiffeners, which are connected to the leading edge with some angle, with the same twist angle per unit length, but in opposite direction (Figure 2.17), the relation between the twist of the leading edge and stiffener is given in Equation 2.3. That is, if the leading-edge pronates, the stiffener pronates.

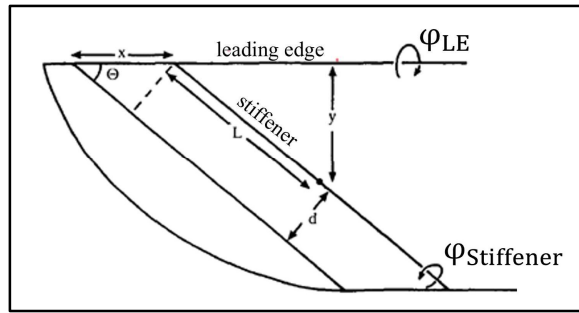


Figure 2.17. The twist mechanism of leading-edge and stiffener (Ennos, 1988)

$$\varphi_{LE} = -\varphi_{stiffener} \quad (2.3)$$

Moreover, the twist in the stiffener results in the camber generation in the chordwise direction as a result of the deformation of the wing membrane in the upward direction. Ennos (1988) stated that the camber generation can be formulated as a function of the twist angle of the leading edge, the wing chord length, and the angle between the stiffener and the leading edge. According to the formula given in Equation 2.4, the camber is inversely proportional to the angle between the stiffener and the leading edge and proportional to the chord length and the angle of the leading edge twist. That is, if the stiffener has 90 degrees angle with the leading edge (ie.: perpendicular), the smallest camber generation will be observed, whereas when the stiffener has a 0-degree angle with the leading edge (ie.: parallel), the highest camber generation will be observed.

$$\text{Camber} = \frac{\varphi_{LE} c}{4 \tan \theta} \quad (2.4)$$

where φ_{LE} is the angle of twist of the leading edge, c is the wing chord length and θ is the angle between the stiffener and the leading edge.

To investigate the effects of wing stiffeners on the aerodynamic performance of the revolving wings, Zhao et al. (2011) did an experimental study with three wings with

different stiffener orientations in a revolving motion. Note that, in this study, only one stiffener is placed on each wing surface (Figure 2.18).

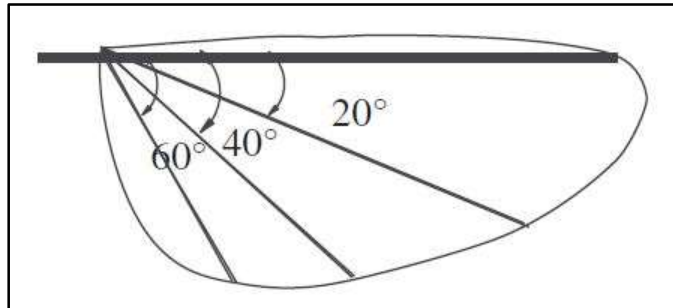


Figure 2.18. Wing with one of three stiffener configurations (Zhao et al., 2011)

The results showed that even the presence of a basic frame attached to the wing enhances the force generation significantly by increasing the wings' rigidity without a weight penalty (Zhao et al., 2011). According to Figure 2.19, a wing with stiffeners generates a higher lift force than a wing without a stiffener. Moreover, wings with 40° and 60° of stiffener orientation even produced more lift force than their rigid counterpart, while generating smaller drag force.

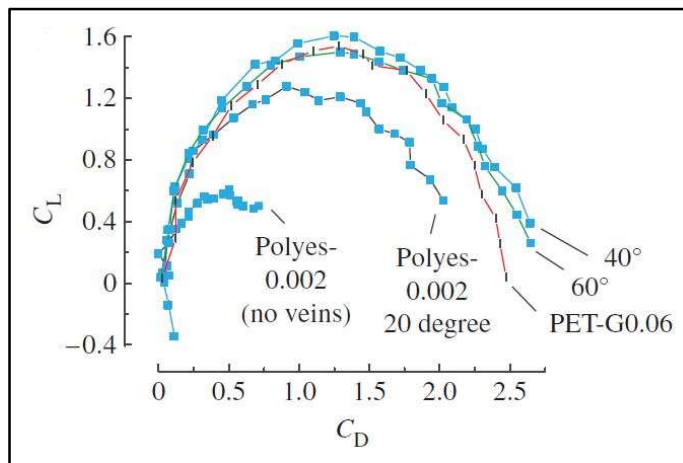


Figure 2.19. Lift versus drag coefficient graph for wings with different stiffener orientations (Zhao et al., 2011)

Camber generation, on the other hand, increased in the positive direction as the angle between the stiffener and the leading edge increased since the additional bending stiffness provided by the stiffener is enhanced as the stiffener angle increases. During

the revolving motion, the wing with a 20° stiffener angle had negative camber, whereas wings with 40° and 60° stiffener orientation had almost zero and zero camber, respectively (Figure 2.20).

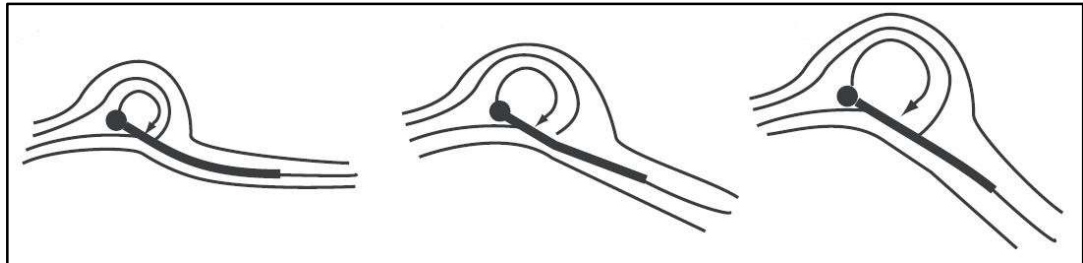


Figure 2.20. Schematic of chordwise deformation and LEV generation of the wings with different stiffener orientations (Zhao et al. 2011)

In addition, Zhao et al. (2011) showed an enhancement in LEV circulation as the camber increases from negative to zero. Therefore, they stated that as the camber generation increases in the positive direction (from negative to positive), the size and strength of the LEV enhances as well, because of the higher TEV circulation generation at the trailing edge. As a result, wings with almost zero and zero camber produced more lift force than wings with negative camber. Therefore, this result proves that the stiffener orientation influences the camber generation and modulates the size and strength of the LEV, thereby the aerodynamic force generation.

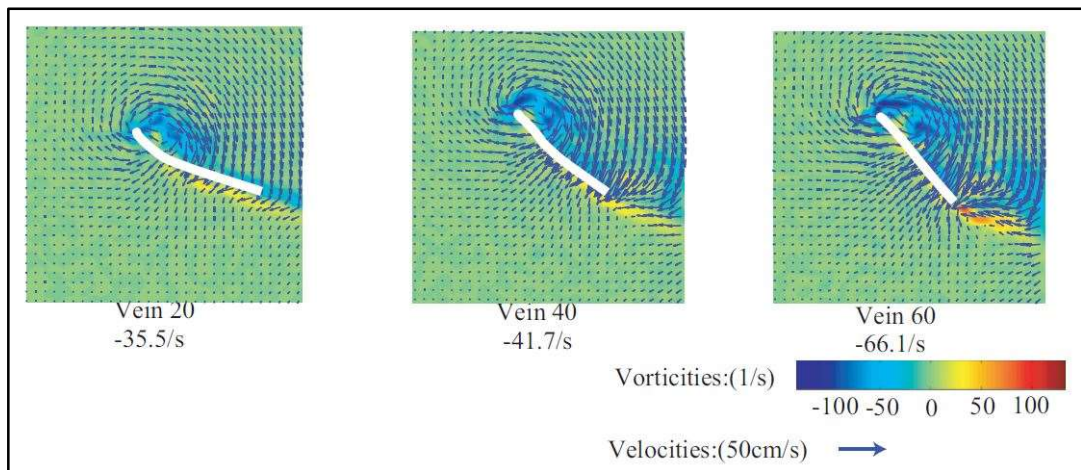


Figure 2.21. PIV image of wings with different stiffener orientations (Zhao et al. 2011)

This page is intentionally left blank

CHAPTER 3

EXPERIMENTAL METHODS & MANUFACTURING

In this chapter, the 3D printing manufacturing process of the test wings and the experimental methods that are used for the flow field visualization and the vector field calculations are explained. To acquire the planar flow field, which is at 75% of the wingspan position, the two-dimensional two-component particle image velocimetry (2D2C PIV) technique was performed. The experimental setup is given in Figure 3.1.

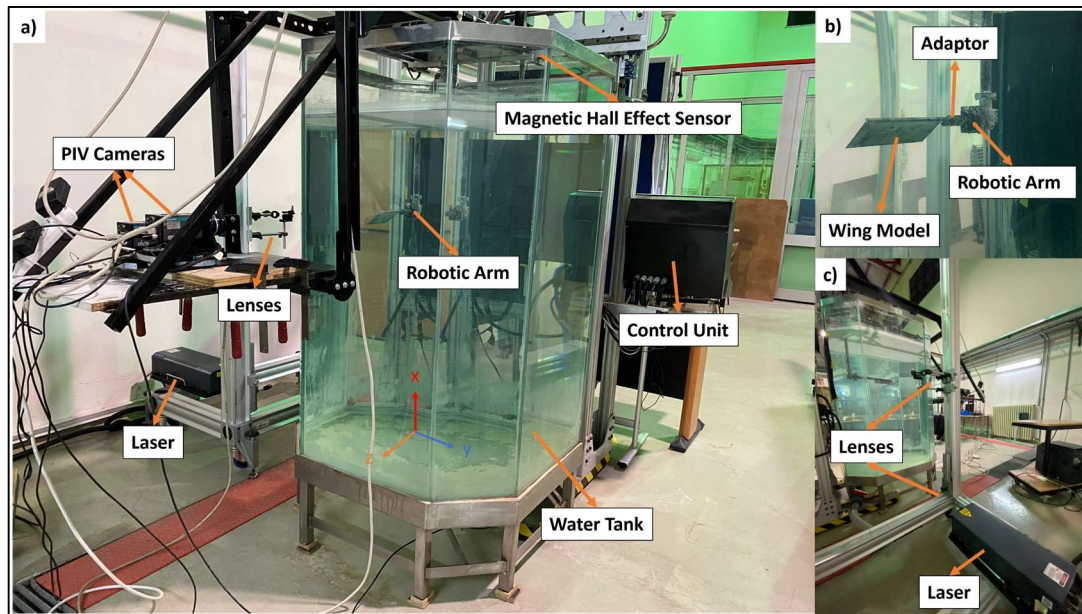


Figure 3.1. Experimental setup

3.1 Water Tank

The experiments were carried out in a water tank, which has an octagonal shape with a 1-meter distance between its parallel edges and 1.5m in height (Figure 3.1). The water tank is placed at the Aerodynamic Laboratory in the Hangar Building, which

is an annex building of the Aerospace Engineering Department of METU. Its surfaces are made of Plexiglass, which is a transparent material, for laser illumination purposes. Therefore, the laser can illuminate the region around the wing without any reflection from the water tank's surfaces.

3.2 Robotic Arm

The movement of the wing models was provided by a robotic arm, which is submerged in the water tank. The robotic arm is designed to translate in x and y axes and rotate around the z-axis, therefore it has three degrees of freedom (See Figure 3.2). It is driven by a control unit that is used for programming motion kinematics. The shaft of the robotic arm is directly connected to a camera board, in which the PIV cameras are placed. As a result, the PIV cameras have the same motion kinematics as the robotic arm, which provides zero relative velocity between the robotic arm and cameras. Therefore, the field of view is kept the same for all measurements during the motion.

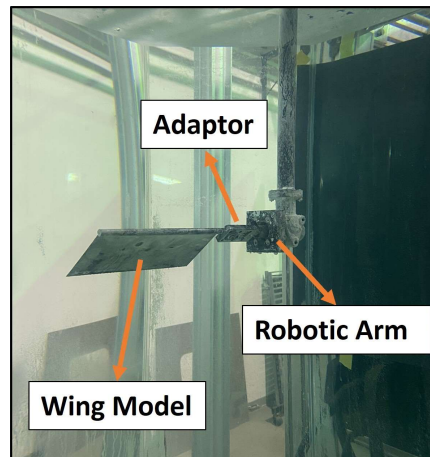


Figure 3.2. Robotic arm

3.3 Wing Models

The wing without a stiffener is shown in Figure 3.3a, whereas in Figures 3.3b, 3.3c, and 3.3d, the wings with different stiffener orientations are represented. Note that, among the wings with stiffeners, the only difference is the angle between the stiffener and the leading edge.

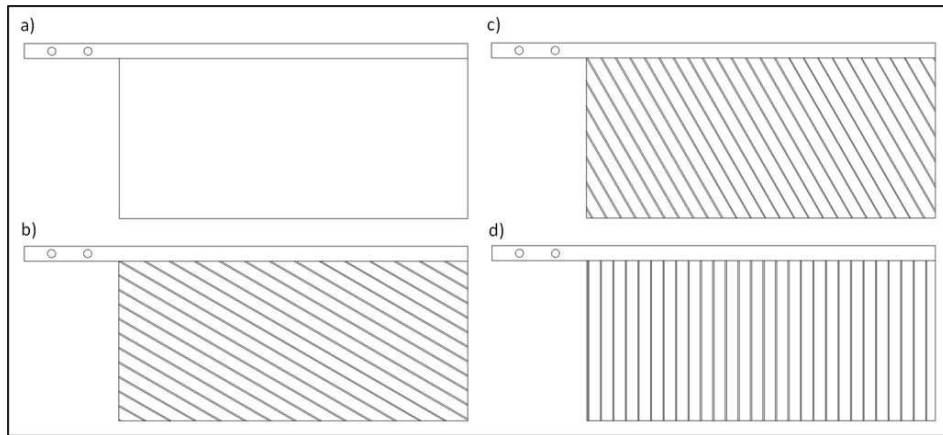


Figure 3.3. Schematic of wing models, a) Wing w/o stiffener, b) Wing w/ 30° Stiffener, c) Wing w/ 60° Stiffener, d) Wing w/ 90° Stiffener

All wings tested have a span length of 184 mm, while the chord length is 92 mm. Therefore, the AR of the wing is 2. In addition, the leading edge has a circular shape and its radius is determined as 4 mm. Note that, the leading edge is extended 50 mm to mount the wing to the adaptor, which connects the wing to the robotic arm. Detailed information about the wing dimensions is given in Table 3.1.

Table 3.1 Wing Size Parameters

Wing Size Parameters	
Chord Length	92 mm
Span Length	184 mm
Leading Edge Radius	4 mm
Surface Thickness	0.15 mm
Aspect Ratio	2

3.4 Wing Flexibility

The wings are designed to be rigid in the spanwise direction and deformable in the chordwise direction. Therefore, the leading edge should have been rigid enough to prevent any bending along the wing span. For this purpose, the radius of the leading edge, which has a circular cross-section, was selected as 4 mm. Note that, a leading-edge radius less than 4 mm failed to provide sufficient bending stiffness along the span, whereas a radius more than 4 mm caused the flow around the leading edge to be disrupted. Moreover, due to the thicker leading edge, the weight of the wings increased, which results in wing tip vibration.

The wing flexibility can be calculated by flexural stiffness (EI), where E is Young's modulus of the material of the wing surface and I is the area moment of the inertia of the wing geometry. Bending stiffness, on the other hand, is the ratio of the elastic dynamic forces to fluid dynamic forces on the wing surface. The equation of the bending stiffness parameter is given below (Shyy et al., 2010)

$$\Pi_1 = \frac{E h^3}{12 (1 - \nu^2) \rho V_t c^3} \quad (3.1)$$

The wings are printed by using Porima PLA filament, which has an Elastic Modulus of 2850 MPa. The surface thickness of the wing was determined as 0.15 mm to have proper chordwise flexibility. The structural properties of the wing without a stiffener are given in Table 3.2.

Table 3.2 Structural Properties of Wing w/o Stiffener

Structural Properties of Wing w/o Stiffener	
Flexural Stiffness	$1.24 \times 10^{-4} \text{ Nm}^2$
Bending Parameter	0.16
Elastic Modulus	2850 MPa

The additional bending stiffness provided by stiffeners can be modulated by changing the stiffener cross-section, radius, the distance between two consecutive stiffeners, and the angle they have with the leading edge. Since the objective of this study is the experimental investigation of the effect of stiffener orientations, the other three parameters are the same for all wings. Note that, stiffeners should provide sufficient flexibility so that the wing could deform and have a decent rigidity, therefore the effect of stiffeners on the wing deformation could be observed. That is, if the stiffeners are excessively rigid, the wings are not able to deform. Therefore, the effect of stiffener orientation on the wing deformation cannot be observed. However, if the stiffeners are over-flexible this time the wing can bend without any resistance provided by the stiffeners, in which the effect of stiffeners, again, cannot be analyzed. Therefore, several parametric studies were carried out to determine the stiffener parameters.

Table 3.3 Stiffener Parameters

Stiffener Parameters	
Stiffener Radius	0.3 mm
Stiffener Distance	6 mm
Stiffener Angle	30°, 60°, 90°

According to these studies, the cross-section of the stiffeners was determined as a semi-circular shape with a radius of 0.3 mm, and they were placed on the wing surface at a 6 mm constant distance apart from each other, which provides sufficient bending stiffness with deformable wing capability. For each wing, the stiffeners have different angles with the leading edge, which are 30°, 60°, and 90°, respectively. The stiffener parameters are shown in Table 3.3.

3.5 Manufacturing Method

To manufacture the wing models, the Raise 3D Pro Plus (Figure 3.4), which is FDM based 3D printing machine, was used to print test wings. The filament used was selected as Porima PLA Black because of its high printing quality. Moreover, the brand offers a data sheet, in which the mechanical properties of the filament can be found. To minimize the reflection of the laser sheet from the wing surface, black color was preferred.

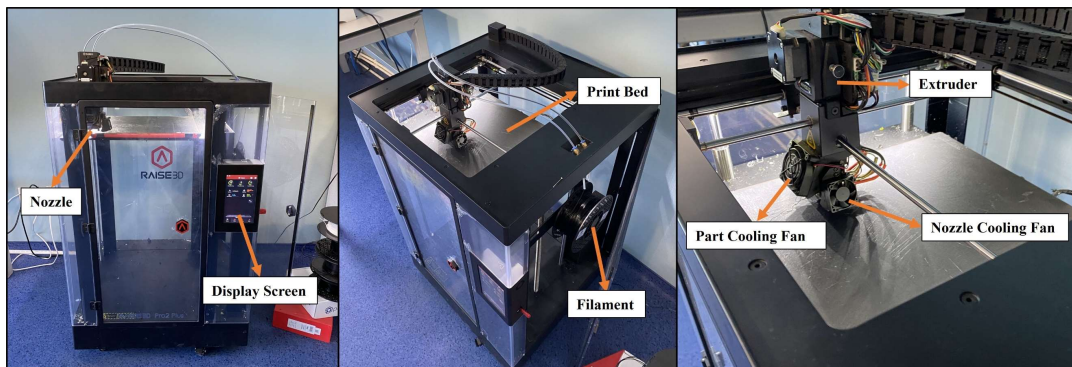


Figure 3.4. Raise 3D Pro Plus

The models were printed on a rough surface (Figure 3.5), which consists of four layers with layer heights of 0.5 mm, 0.38 mm, 0.22 mm, and 0.22 mm, and line orientations of 0°, 90°, 45°, and 45°, respectively. For the first two layers, the printing speed was 8 mm/s and 30 mm/s, respectively to achieve a shorter printing time with good sticking on the printing table, since it has a minor influence on the wing's surface quality. For the last two layers, which are called surface layers, on the other hand, the printing speed was reduced to 20 mm/s to obtain a surface with good quality, which is smooth and void-free, since the quality of the top layer of the rough surface directly affects the quality of the model surface (Figure 3.6).



Figure 3.5. Rough surface and wing model

Moreover, these two layers have the same printing orientation as the model's first layer, in which the contact surface of the two layers is minimized so that they can be separated from each other with ease. The models were removed from the rough surface with a help of a thin metal sheet, therefore no chemicals were used during the removal process.

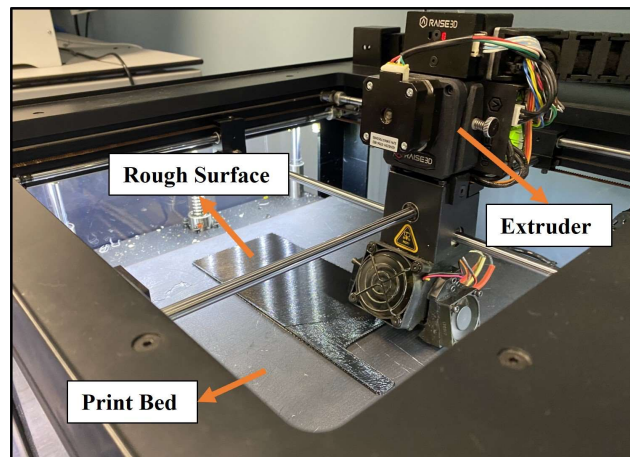


Figure 3.6. Printing the rough surface

The wing models consist of three layers with 0.05 mm layer height, therefore the total thicknesses of the different wing models, excluding the thickness of stiffeners, are the same and 0.15 mm. This value is the minimum thickness that can be printed by the aforementioned 3D printer. That is, a model with a layer thickness thinner than 0.05 mm had poor surface quality with some voids on it and a model with a surface thickness less than 0.15 mm could not be removed from the rough surface

properly since they were structurally very brittle. For all three layers, the printing speed was 30 mm/s and printing orientations were -45° , 90° , and 45° respectively. In this way, it is aimed to obtain extra bending stiffness throughout the wingspan, which is provided by the 90° printing orientation. The printing temperature of the nozzle was 220°C , and the platform temperature was 65°C . The printing parameters are given in Table 3.4.

Table 3.4 Printing Parameters

Printing Parameters	
Filament Type	PLA
Layer Height	0.05 mm
Printing Orientation	-45° , 90° , 45°
Printing Temperature	220°C

The leading edge was printed in two parts, where one half was printed together with the wing surface and the other half printed separately (Figure 3.7). Then, two symmetric parts were glued together with a help of a fixture that indicates the correct position of the two sides. The stiffeners, on the other hand, were printed on the wing's upper surface.

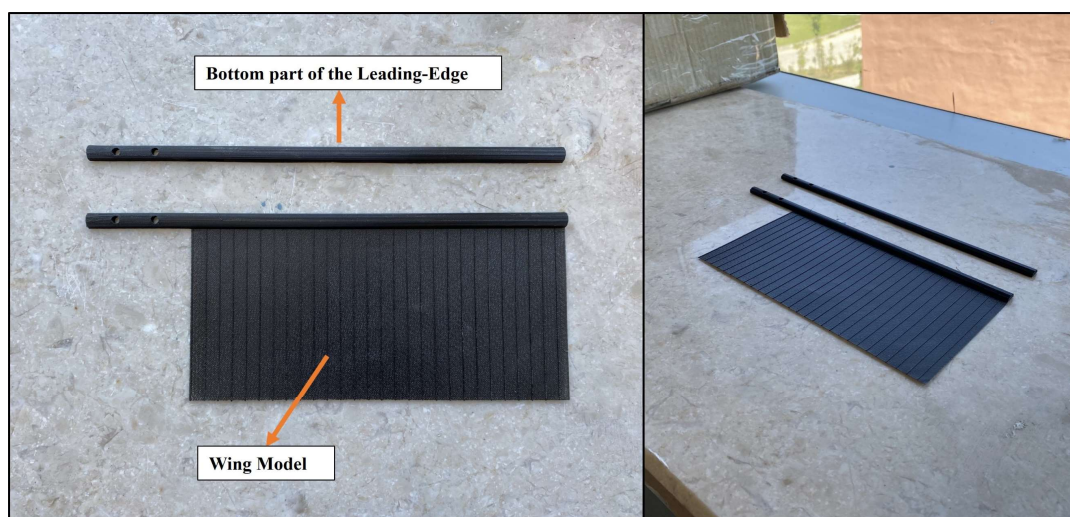


Figure 3.7. Two parts of the wing structure

To be sure that the wings are printed properly, three-stage production control was carried out. That is, in the first stage the printed wings were checked by eyes, in which any cracks or plastic deformation that may occur during the wing removing process from the rough surface were tried to be determined (Figure 3.8).



Figure 3.8. Defective wing and well-printed wing

In the second stage, the wings were measured with a help of a ruler (Figure 3.9). Therefore, all the wing models have predetermined sizes.

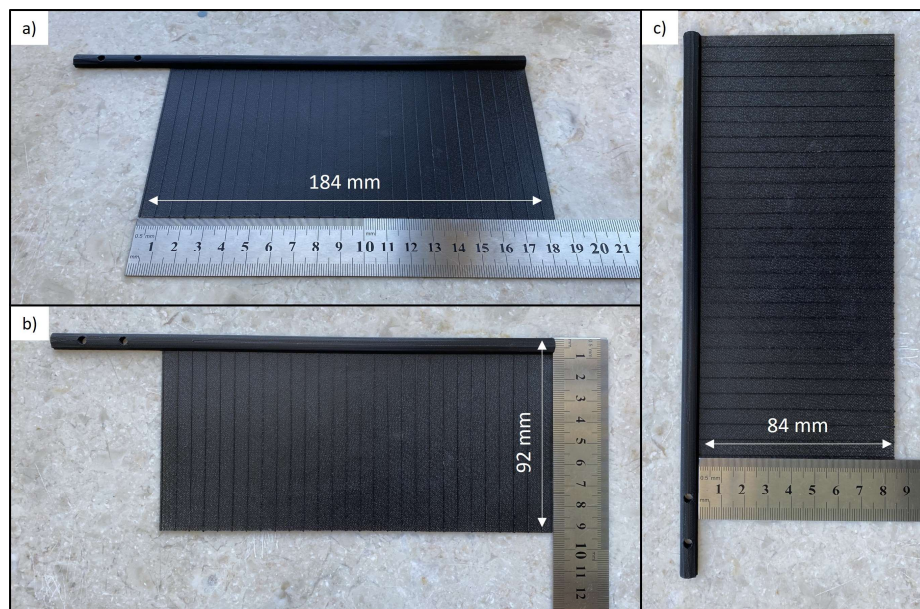


Figure 3.9. Wing size measurement

In the final stage, the wings were placed in a fixture (Figure 3.10), which was printed with the same process, to check whether the wing edges coincided with the fixture or not. Only wings passing three control stages were used in the experiment. A wing that failed in any step was identified as scrap and new wings were printed. Therefore, by this method, any cracks, voids, or plastic deformations on the wing surface were eliminated.



Figure 3.10. Wing fixture

Moreover, all wings have the same dimensional properties as they are designed. As a result, the only parameter that makes the wings to be distinguished from each other is the angle between the stiffener and the leading edge. Therefore the effect of stiffener orientation on the flow field around the wing can be analyzed properly. The complete wing models are shown in Figure 3.11.

Note that, the total printing and preparing time of each wing was approximately 10 hours.

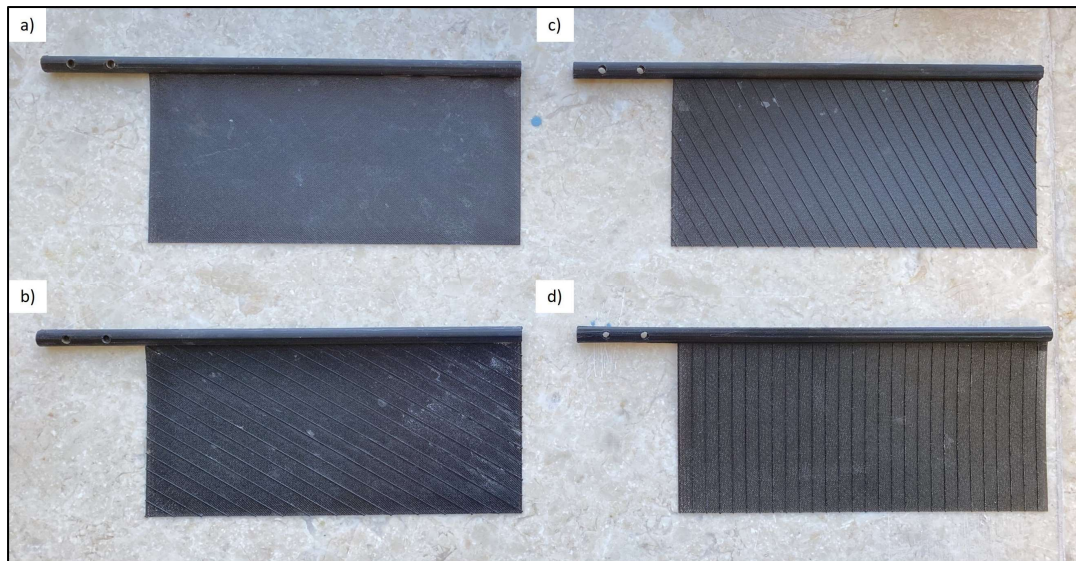


Figure 3.11. Printed wing models a) Wing w/o stiffener, b) Wing w/ 30° Stiffener, c) Wing w/ 60° Stiffener, d) Wing w/ 90° Stiffener

3.6 Motion Kinematics

The motion of the wing includes two phases. In the first phase of the motion of the wings ($0 \leq \delta^* < 1.0$), for one chord length of distance the wings start to accelerate with a constant acceleration, which is 0.035 mm/s^2 until the predefined terminal velocity of 0.08 m/s is achieved. In the second phase, ($1.0 < \delta^* \leq 3.8$), for a three-chord length of distance the wings keep translating with constant terminal velocity. The motion kinematics is shown in Figure 3.12. Note that, δ^* is the non-dimensional distance traveled by the wing, where $\delta^* = \delta/c$, and t^* is the convective time, where $t^* = t \times V_t/c$.

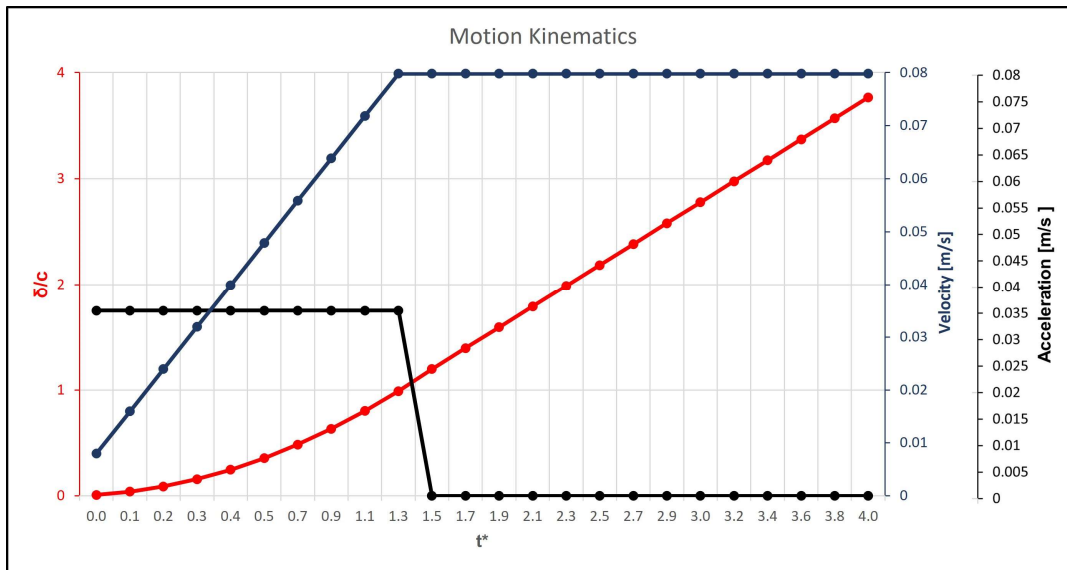


Figure 3.12. Motion kinematics

The Reynold number is 7360, where the wing chord length is 92 mm, and the terminal velocity is 0.08 m/s. The angle of attack is constant and 45° during the motion. However, the geometric angle of attack changes because of wing chordwise flexibility.

Table 3.5 Motion Kinematics

Wing Kinematics	
Terminal Velocity	0.08 m/s
Acceleration	0.035 m/s^2
Reynolds Number	7360
Angle of Attack	45°
Acceleration Phase	$0 \leq \delta^* \leq 1.0$
Constant Velocity Phase	$1.0 < \delta^* \leq 3.8$

3.7 Flow Field Measurements via Particle Image Velocimetry

To acquire planar flow fields at 75% of the wing span the two-dimensional two-component particle imaging velocity measurement technique (2D2C PIV) was used. During the PIV image recording, Dantec FlowManager v4.60 software was used. To process the recorded PIV images, DynamicStudio 2015a was preferred. The components PIV system are described in the following sections.

3.7.1 Field of View and Imaging

During the experiments, two 12-bit HiSense MK II CCD cameras, which have a pixel size of 6.45 nanometer, and an image resolution of $1344 \times 1024 \text{ pixel}^2$ individually, are used and to increase the size of the field of view they are placed side by side. PIV cameras used in experiments are given in Figure 3.13. For both cameras, Nikon 50 mm with an aperture size of $f\# = 2$ is used as the focal objective. To capture both LEV and TEV properly, the cameras are positioned at different heights. That is, the camera at the left is positioned at a lower height to capture the TEV, whereas the camera on the right is placed at a higher position to visualize the LEV properly.

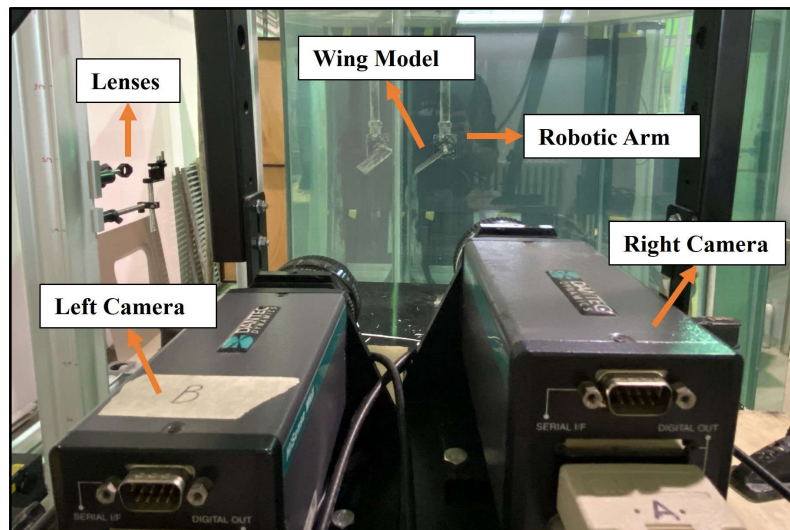


Figure 3.13. PIV cameras

Both cameras can be translated with the wing models since they are placed on the camera board, which is connected to the robotic arm. As a result, the field of view is kept constant during the translating motion.

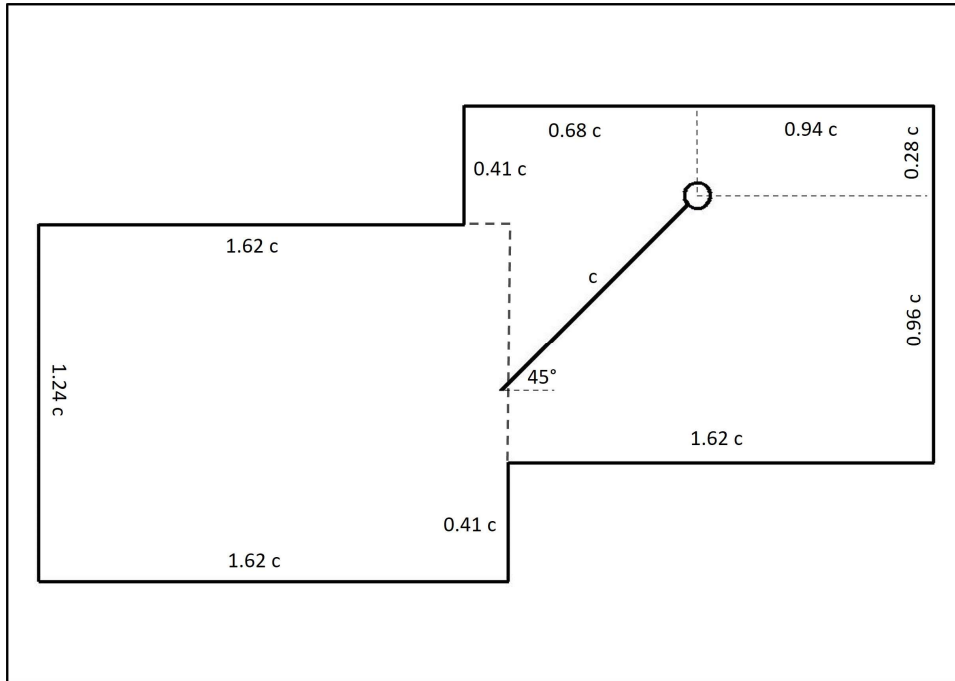


Figure 3.14. Schematic of the field of view

The PIV images obtained from each camera are stitched by a MATLAB code provided by the Dantec FlowManager v4.60 software, by simply importing the pixel coordinates of the calibration target image. As a result, stitched images with a pixel size of $2562 \times 1354 \text{ pixel}^2$ are achieved. By introducing the scale factor, which is 16.85 for both cameras, the field of view is obtained as $278.2 \text{ mm} \times 148.1 \text{ mm}$. The field of view is given in Figure 3.14.

3.7.2 Illumination

To illuminate the 75% span position, a double-pulsed Nd: YAG laser with a pulse energy of 120 mJ at a wavelength of 532 nm was used. Two consecutive laser pulses have a time interval of 9 ms. A Plano-Concave cylindrical lens having an effective focal length of -6.4 mm and a Plano-Convex spherical lens that has an effective focal

length of 500 mm are preferred for laser sheet generation at the predetermined span section (See Figure 3.19).

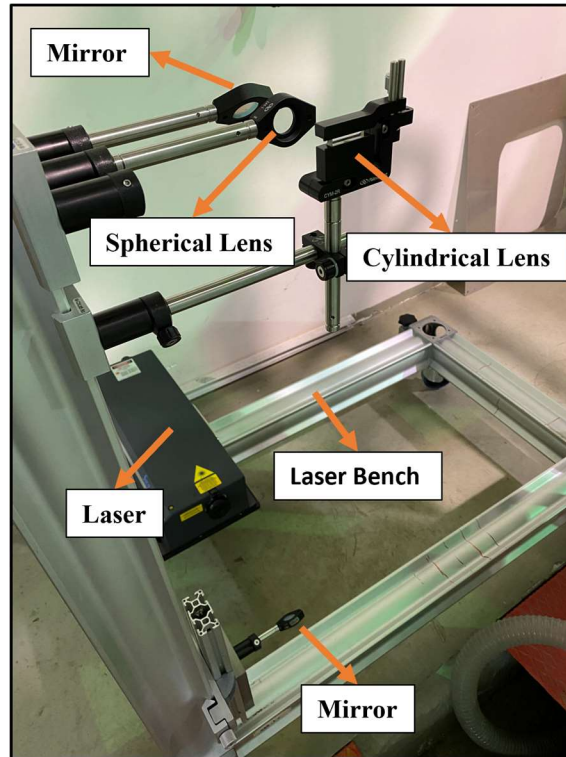


Figure 3.15. Spherical and cylindrical lenses and laser source

The optic system used in the experiment is shown in Figure 3.15. Note that, since PLA is not a transparent material, the laser sheet was not able to pass through the wing model, therefore bottom side of the wing model, which is the pressure side, was not illuminated. Detailed information about the components of the illumination is given in Table 3.6.

Table 3.6 The Components of illumination

Optics	
Cylindrical Lens	Plano-Concave
Effective Focal Length	-12.77 mm
Spherical Lens	Plano-Convex
Effective Focal Length	750 mm
Laser	
Model	Nd: YAG Laser, SOLO 120 XT
Maximum Energy	120 mJ/pulse
Wavelength	532 nm
Thickness	≈ 4-5 mm
Max Repetition Rate	21 Hz
Manufacturer	New Wave Research

3.7.3 External Trigger Mechanism

To obtain PIV images at the specific instant of motion, an external trigger mechanism containing a magnetic Hall sensor and 17 magnets that are placed at a distance of 0.2 chord length from two consecutive magnets were used. The sensor generates a TTL signal as it passes a magnet, which triggers the image acquisition. The components of the external trigger mechanism are given in Figure 3.16.

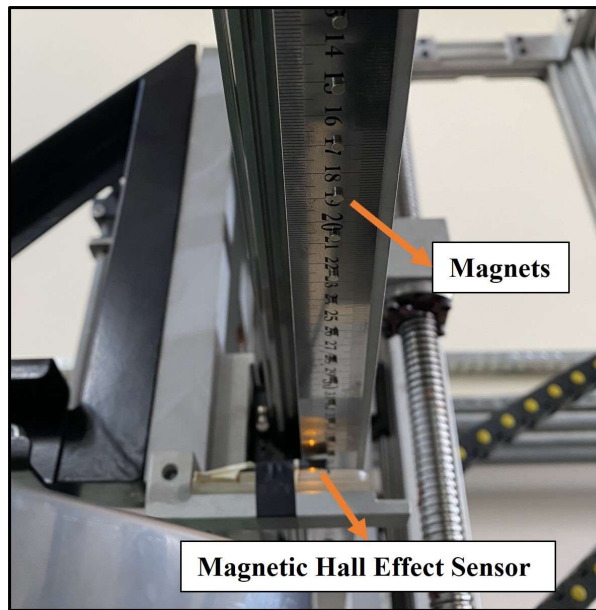


Figure 3.16. Magnets and magnetic hall effect sensor

3.7.4 Seeding

As a tracer particle, hollow glass spheres, which are a high-quality seeding material with desirable light scattering capability in the PIV industry, were used. They have a mean diameter of $65 \mu\text{m}$ with a density of 0.21 gr/cm^3 , which allows the particles to be suspended in the water for a longer time. The average seeding density was approximately 110 and 1000 in the 64×64 and 192×192 interrogation areas, respectively. In Figure 3.17, a PIV image showing the seeding particles is given.

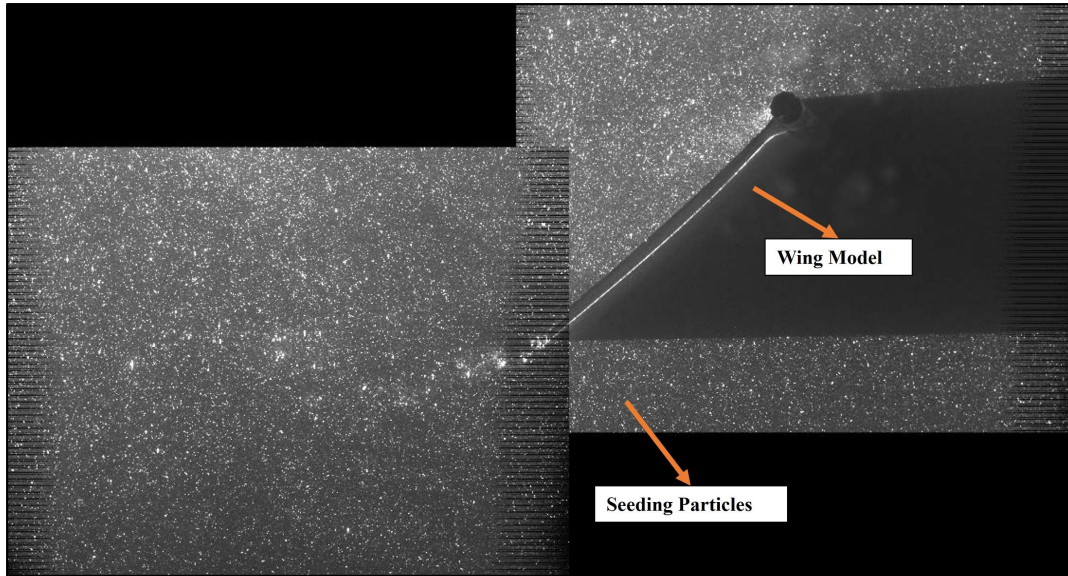


Figure 3.17. Seeding particles

3.7.5 Flow Condition

The laser was placed at the left side of the robotic arm, therefore the wings moved from left to right to obtain proper illumination on the wings' upper surface, which is the suction side. As the wing moves, it also sets the water in motion. Therefore, there was approximately five minutes pause between two consecutive runs to completely diminish the movement of the water. The waiting time started when the wing reached its initial position.

3.7.6 Image Acquisition

The PIV images obtained from each camera were stitched by a MATLAB code provided by the Dantec FlowManager v4.60 software, by simply importing the pixel coordinates of the calibration target image. Then, stitched images were imported to DynamicStudio 2015a. For the flow field measurements, an ensemble averaging of six images was performed to increase the signal-to-noise ratio, although the calculations converged after 4 numbers of samples were employed (Figure 3.18).

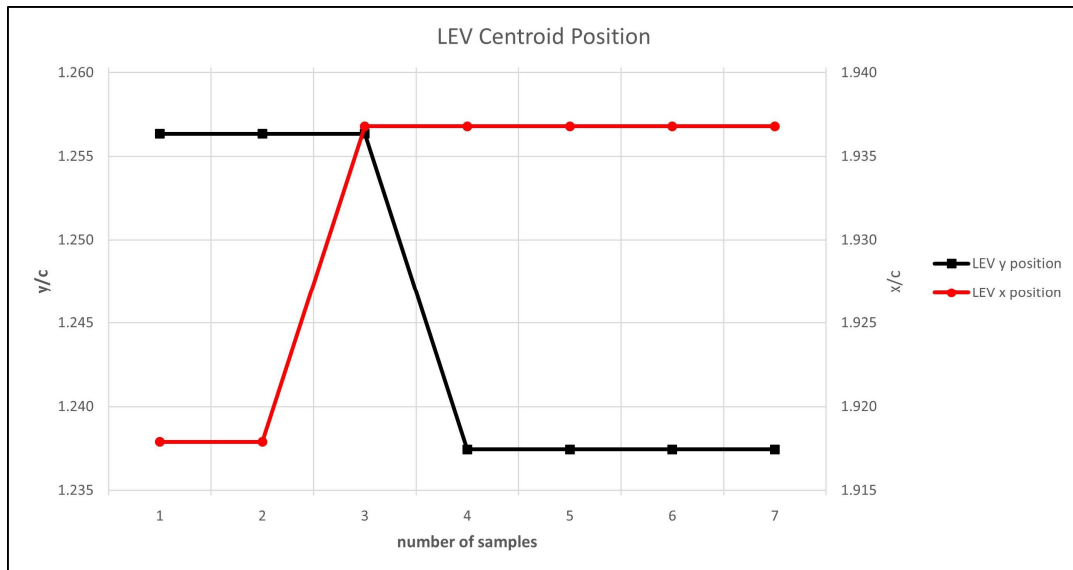


Figure 3.18. LEV centroid positions for different numbers of samples

3.8 Data Processing

3.8.1 Calibration

The calibration process was carried out in eight steps. First, a line at the 75% span position was marked on the wing surface, which is illuminated by the laser. Secondly, the marked wing was mounted to the robotic arm and it was moved to the initial point of the motion, and the movement was paused. In the third step, the laser sheet coincided with the line that was marked on the wing surface (Figure 3.19a). Note that, in Figure 3.19, unit b represents the wing span that is 184 mm. Then, the wing was moved according to the programmed motion, and the position of the laser sheet was checked at five control points as the wing moved and stopped so that the laser sheet has no angle with the direction of the motion. Therefore, the laser sheet always illuminates the 75% span position throughout the motion.

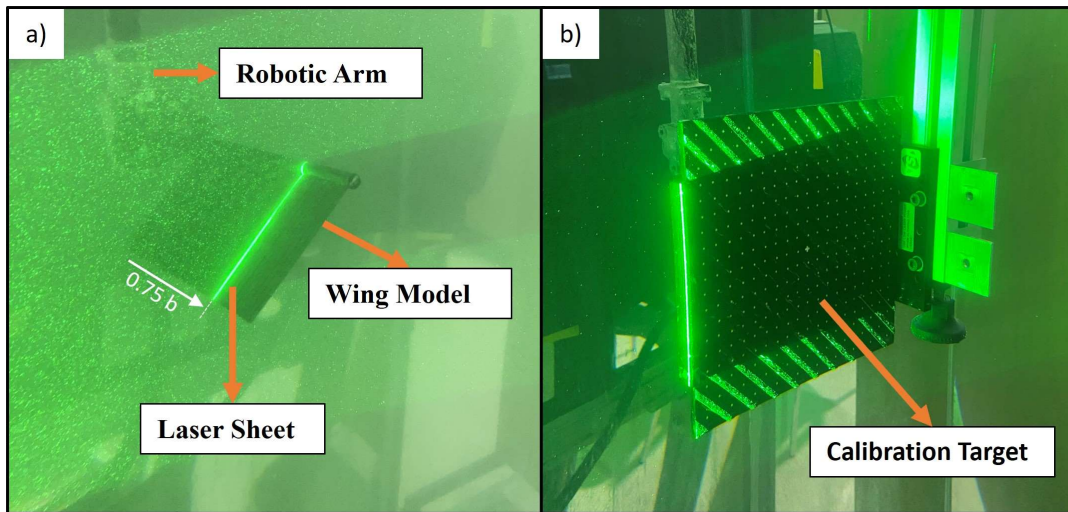


Figure 3.19. Laser sheet at the 75% wingspan

In the fifth step, the wing was removed from the robotic arm and the calibration target was submerged in the water tank. In the sixth step, the calibration target was placed at the 75% wing span position with a guideline of laser sheet, whose position was calibrated and fixed at the 75% span length (Figure 3.19b). In the seventh step, both cameras were focused on the dots on the calibration target (Figure 3.20), separately and a single image at the stationary position was taken from both cameras when the position of the calibration target was fixed at the 75% span position (Figure 3.21).

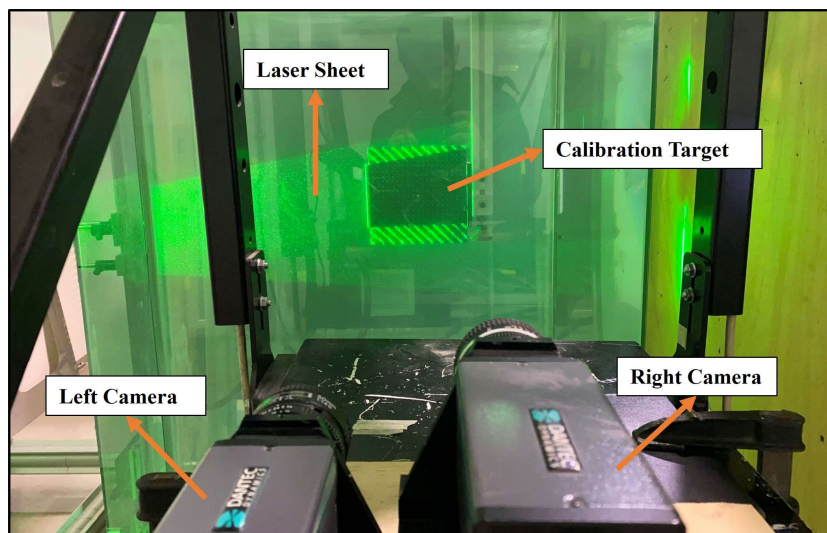


Figure 3.20. Focusing the PIV cameras

In the final step, by measuring the distance between the pixel values and white dots on the image of the calibration target acquired from PIV cameras, the scale factor was calculated as 16.85 for both cameras, individually.

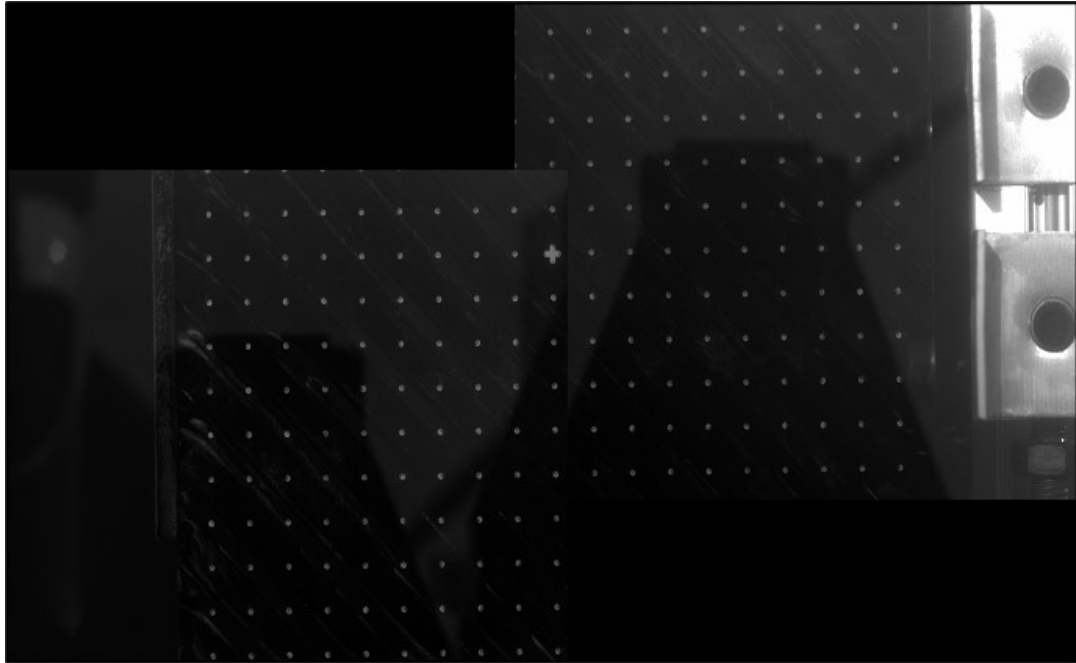


Figure 3.21. Stitched calibration image

3.8.2 Image Pre-Processing

The PIV images obtained from the two cameras at each time instant were stitched (Figure 3.22 a) by using the coordinates acquired from the dots on the calibration target and these images were imported to DynamicStudio 2015a. To improve the image quality first, a mask around the wings in each phase of the motion was defined (Figure 3.22 b). In the second step, all images were masked according to the defined mask corresponding to each image (Figure 3.22 c). In the third step, the mean minimum pixel values were calculated (Figure 3.22 d). In the fourth step, the corresponding mean minimum pixel values were subtracted from each masked image to extract the reflections and diminish the background noise (Figure 3.22 e). In the fifth step, image balancing was employed to the images to eliminate the CCD

leakage. In the sixth step, a light sheet balance map was created. In the final step, the corresponding light sheet balance map was performed on all PIV images and balanced images were obtained (Figure 3.22 f).

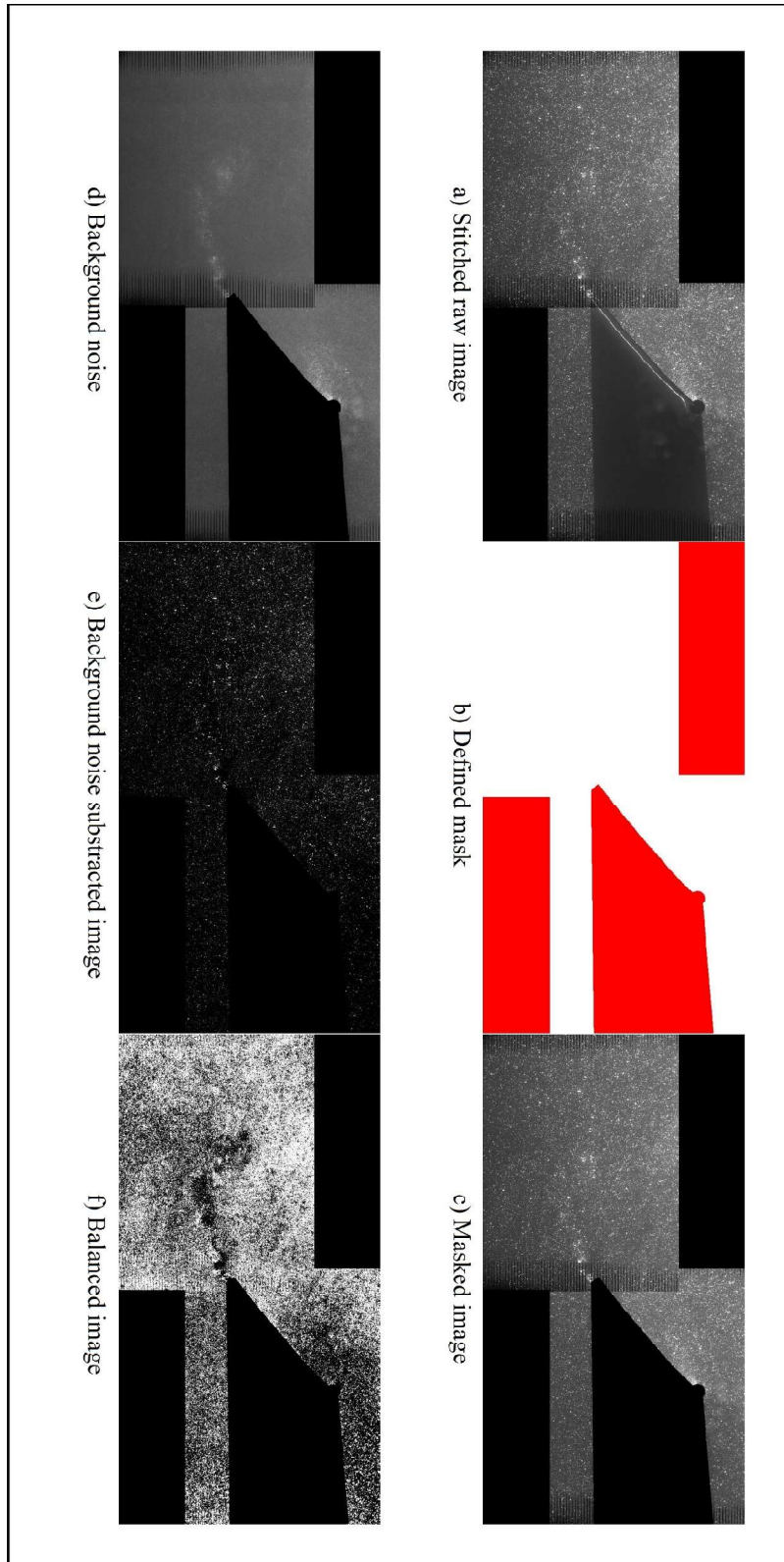


Figure 3.22. Steps of pre-processing

3.8.3 Vector Calculations (Processing)

The vector calculations were carried out in four steps. First, the stitched images were cross-correlated by using the adaptive correlation feature of DynamicStudio 2015a (Figure 3.23 a). The number of refinements was determined as two, where the initial interrogation area size was $256 \times 256 \text{ pixel}^2$ and the final interrogation area size was $64 \times 64 \text{ pixel}^2$ with 75% overlap. Moreover, high accuracy subpixel refinement was employed. Secondly, the predefined mask (Figure 3.23 b) defined in the second process of pre-processing is used to mask the velocity vectors obtained from adaptive correlation (Figure 3.23 c). In the third step, to modify the incompatible velocity vectors, the universal outlier detection method was performed twice on the velocity vectors (Figure 3.23 d-e). In the final step, an ensemble averaging of six images was performed by using six PIV images obtained from each phase of the motion (Figure 3.23 f).

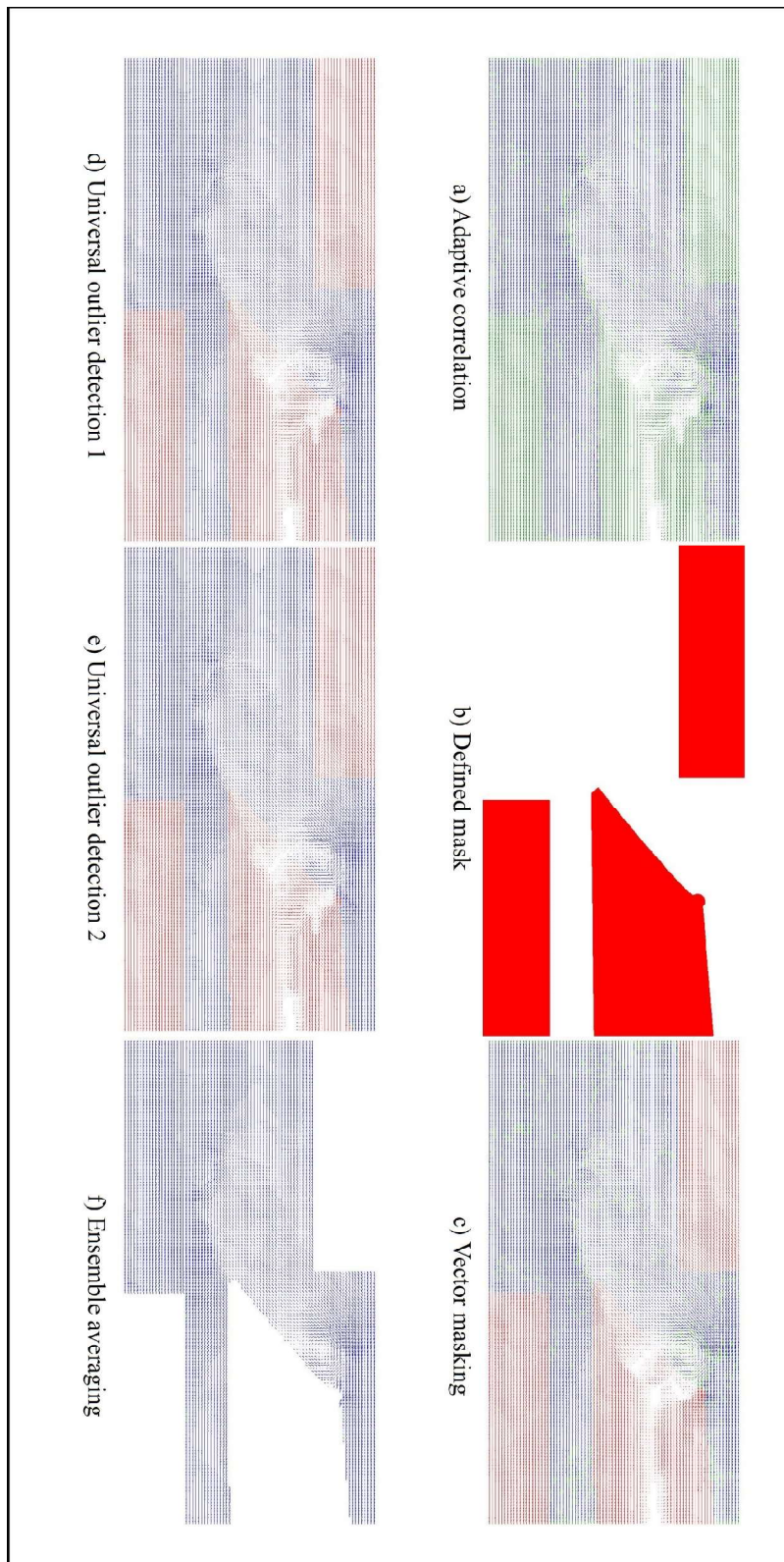


Figure 3.23. Steps of vector calculation

3.9 LEV & TEV Circulation

The circulation can be defined as a line integral of the velocity around a closed curve, C in the flow (Anderson, 1984). The circulation is related to the vorticity, ω_z and the calculation of the LEV and TEV circulation around the wing can be done by using the formula given in Equation 3.2.

$$\Gamma = \oint_C \omega_z \, dx \, dy \quad (3.2)$$

The circulation value can be non-dimensionalized by the terminal velocity, V_t and wing chord length, c as it is expressed in Equation 3.3.

$$\Gamma^* = \frac{\Gamma}{V_t c} \quad (3.3)$$

Note that, the LEV and TEV circulations are calculated by the γ_2 function, which will be described in the following section.

3.10 LEV & TEV Centroid Detection Method

The γ_1 function was used to capture the vortex centroid, whereas γ_2 function was employed to detect the vortex boundary. These are scalar functions that are derived from the velocity fields. The location of the vortex centroid and the vortex boundary can be characterized by these methods, where only the topology of the velocity field is considered (Graftieaux et al., 2001).

γ_1 function:

γ_1 is a non-dimensional scalar function its magnitude is bounded by a closed interval $[0, 1]$. It calculates the relative rotation around the points inside a defined flow domain. To do that, firstly it determines a point and draws radius vectors from it to

the velocity vectors around this point. Secondly, it calculates the angle between the velocity vectors and radius vectors by the formula given in Equation 3.4. That defined point is determined as a vortex center if the velocity vectors are perpendicular to the radius vectors.

$$\begin{aligned}\gamma_1(P) &= \frac{1}{N} \sum_S \frac{(\vec{R}_{PM} \times \vec{V}_M) \cdot \vec{z}}{\|\vec{R}_{PM}\| \|\vec{V}_M\|} \\ &= \frac{1}{N} \sum_S \sin \theta_M\end{aligned}\quad (3.4)$$

where N is the number of points M inside the two-dimensional area S that surrounds M and P . \vec{V}_M and \vec{R}_{PM} are the velocity vectors and the radius vector between the point P and velocity vectors, respectively. θ_M is the angle between the velocity vector, \vec{V}_M and the radius vector, \vec{R}_{PM} . \vec{z} is the unit vector that is normal to the measurement plane.

Note that, the numerator is a cross product of the velocity vector, \vec{V}_M and the radius vector, \vec{R}_{PM} , whereas in the denominator, the magnitudes of these two vectors are multiplied. Therefore, the result of this fraction operation is nothing but the $\sin \theta_M$. A point where the γ_1 has its maximum value, which is 1, is identified as the vortex centroid. In addition, γ_1 function provides information about the rotation sign of the detected vortex.

γ_2 function:

To identify the vortex boundary, γ_2 function. Although γ_1 and γ_2 functions have the same algorithm while calculating the γ_2 the local convection velocity, \vec{V}_P is taken into account. In addition, unlike γ_1 function, γ_2 function is a Galilean invariant, which states that the laws of motion are the same in all inertial frames (Graftieaux et al., 2001). The formula of the γ_2 function is given in Equation 3.5.

$$\gamma_2(P) = \frac{1}{N} \sum_S \frac{[\vec{R}_{PM} \times (\vec{V}_M - \vec{V}_P)] \cdot \vec{z}}{\|\vec{R}_{PM}\| \|\vec{V}_M - \vec{V}_P\|} \quad (3.5)$$

Note that, in a region where $|\gamma_2| > 2/\pi$, the rotation dominates the flow locally and a vortex core can be represented (Graftieaux et al., 2001). Therefore, the circulation is integrated over a chordwise oriented region where $|\gamma_2| > 2/\pi$.

3.11 Analysis of Measurement Errors

3.11.1 Uncertainty in Velocity Vectors

The particle displacement in pixels is determined in the range of 0.05-0.1 pixel for uncertainty calculations in the literature (Brossard et al., 2015). It is taken as 0.1 in this study. The uncertainty in the velocity vectors is calculated as 0.82%.

$$\varepsilon_U = \frac{\varepsilon_{\Delta x}/\Delta t}{SF} \quad (3.6)$$

where, ρ and c represent the fluid density and wing chord length, respectively.

$$\begin{aligned} \varepsilon_U &= \frac{(0.1 / 9 \times 10^{-3}) \text{ pixel/sec}}{16.85 \text{ pixel/mm}} \quad (3.7) \\ &= 6.53 \times 10^{-4} \text{ m/s} \end{aligned}$$

The percent uncertainty:

$$\alpha_{\text{velocity}}\% = \frac{6.53 \times 10^{-4} \text{ m/s}}{0.08 \text{ m/s}} \times 100 \quad (3.8)$$

$$= 0.82 \%$$

Therefore, for terminal velocity, the percent uncertainty is calculated as 0.82%.

3.11.2 Uncertainty in the LEV & TEV Circulation

To calculate the uncertainty of the LEV and TEV circulation, as a first step, the circulation values of each phase of the motion are computed for each wing. Secondly, the mean value of each circulation value is calculated by the formula given in Equation 3.9.

Mean value:

$$\bar{\Gamma} = \frac{1}{N} \sum_{i=1}^N \Gamma_i \quad (3.9)$$

$$\bar{\Gamma}_{LEV} = 6.71 \times 10^{-3} \text{ m}^2/\text{s}$$

$$\bar{\Gamma}_{TEV} = 3.93 \times 10^{-3} \text{ m}^2/\text{s}$$

Thirdly, the standard deviations of LEV and TEV circulations are calculated according to the formula given in Equation 3.10 for all wings at each phase of the motion.

Standard deviation:

$$\sigma_{\text{circulation}} = \left[\frac{1}{N} \sum_{i=1}^N (\Gamma_i - \bar{\Gamma})^2 \right]^{\frac{1}{2}} \quad (3.10)$$

$$\sigma_{LEV_{\text{circulation}}} = 3.98 \times 10^{-4} \text{ m}^2/\text{s}$$

$$\sigma_{TEV_{\text{circulation}}} = 2.19 \times 10^{-4} \text{ m}^2/\text{s}$$

Finally, the uncertainty of LEV and TEV circulation is calculated based on the formula given in Equation 3.11. Note that, k, which is the coverage factor, is taken as 1.96 for a 95% confidence level.

Uncertainty:

$$\alpha_{\text{circulation}} = \pm \frac{k \sigma_{\text{circulation}}}{\sqrt{N}} \quad (3.11)$$

$$\alpha_{\text{LEV}_{\text{circulation}}} = \pm 1.25 \times 10^{-3} \text{ m}^2/\text{s}$$

$$\alpha_{\text{TEV}_{\text{circulation}}} = \pm 1.75 \times 10^{-4} \text{ m}^2/\text{s}$$

Percent uncertainty:

$$\alpha_{\text{circulation}} \% = \frac{|\alpha_{\text{circulation}}|}{\bar{\Gamma}} \times 100 \quad (3.12)$$

$$\alpha_{\text{LEV}_{\text{circulation}}} = 4.75\%$$

$$\alpha_{\text{TEV}_{\text{circulation}}} = 4.45\%$$

The percent uncertainty of LEV and TEV circulations are calculated as 4.75% and 4.45%, respectively.

3.11.3 Uncertainty in LEV & TEV Centroid

The uncertainty values of the centroid of the LEV and TEV centroid are computed in the x and y-axis, individually. Similar to the uncertainty of circulation calculations, first, the mean values of the x and y positions of the LEV and TEV centroids are calculated for each phase of the motion for each wing. Secondly, the standard deviation of the x and y positions of the LEV and TEV centroids are calculated, and the maximum values of each calculation are taken. Finally, the uncertainty values of LEV and TEV circulations are conducted by the equations

given below. For uncertainty calculations, k , which is the coverage factor, is taken as 1.96 for a 95% confidence level.

In x position:

Mean Value:

$$\bar{x}_{\text{centroid}} = \frac{1}{N} \sum_{i=1}^N x_i \quad (3.13)$$

$$\bar{y}_{\text{LEV}_{\text{centroid},x}} = 1.79 \times 10^{-1} \text{ m}$$

$$\bar{y}_{\text{TEV}_{\text{centroid},x}} = 4.45 \times 10^{-1} \text{ m}$$

Standard Deviation:

$$\sigma_{\text{centroid},x} = \left[\frac{1}{N} \sum_{i=1}^N (x_i - \bar{x})^2 \right]^{\frac{1}{2}} \quad (3.14)$$

$$\sigma_{\text{LEV}_{\text{centroid},x}} = 1.67 \times 10^{-3} \text{ m}$$

$$\sigma_{\text{TEV}_{\text{centroid},x}} = 1.56 \times 10^{-3} \text{ m}$$

Uncertainty:

$$\alpha_{\text{centroid},x} = \pm \frac{k \sigma_{\text{centroid}}}{\sqrt{N}} \quad (3.15)$$

$$\alpha_{\text{LEV}_{\text{centroid},x}} = \pm 1.33 \times 10^{-3} \text{ m}$$

$$\alpha_{\text{TEV}_{\text{centroid},x}} = \pm 1.25 \times 10^{-3} \text{ m}$$

Percent uncertainty:

$$\alpha_{\text{centroid},x} \% = \frac{|\alpha_{\text{centroid},x}|}{\bar{x}_{\text{centroid}}} \times 100 \quad (3.16)$$

$$\alpha_{\text{LEV}_{\text{centroid},x}} \% = 0.74\%$$

$$\alpha_{\text{TEV}_{\text{centroid},x}} \% = 2.80\%$$

The percent uncertainty values of LEV and TEV centroid in the x-axis is computed as 0.74 % and 2.80 %, respectively.

In y position:

Mean Value:

$$\bar{y}_{\text{centroid}} = \frac{1}{N} \sum_{i=1}^N y_i \quad (3.17)$$

$$\bar{y}_{\text{LEV}_{\text{centroid},y}} = 1.17 \times 10^{-1} \text{ m}$$

$$\bar{y}_{\text{TEV}_{\text{centroid},y}} = 6.46 \times 10^{-2} \text{ m}$$

Standard deviation:

$$\sigma_{\text{centroid},y} = \left[\frac{1}{N} \sum_{i=1}^N (y_i - \bar{y})^2 \right]^{\frac{1}{2}} \quad (3.18)$$

$$\sigma_{\text{LEV}_{\text{centroid},y}} = 1.64 \times 10^{-3} \text{ m}$$

$$\sigma_{\text{TEV}_{\text{centroid},y}} = 8.20 \times 10^{-4} \text{ m}$$

Uncertainty:

$$\alpha_{\text{centroid,y}} = \pm \frac{k \sigma_{\text{centroid,y}}}{\sqrt{N}} \quad (3.19)$$

$$\alpha_{\text{LEV}_{\text{centroid,y}}} = \pm 1.31 \times 10^{-3} \text{ m}$$

$$\alpha_{\text{TEV}_{\text{centroid,y}}} = \pm 6.56 \times 10^{-4} \text{ m}$$

Percent uncertainty:

$$\alpha_{\text{centroid,y}} \% = \frac{|\alpha_{\text{centroid,y}}|}{\bar{y}_{\text{centroid}}} \times 100 \quad (3.20)$$

$$\alpha_{\text{LEV}_{\text{centroid,y}}} \% = 1.12\%$$

$$\alpha_{\text{TEV}_{\text{centroid,y}}} \% = 1.02\%$$

The percent uncertainty values of LEV and TEV centroid in the x-axis is computed as 1.12% and 1.02%, respectively.

The results obtained by the uncertainty calculations are given in Table 3.7.

Table 3.7 Uncertainty Values

	Velocity (V_t)	LEV Circulation ($\bar{\Gamma}_{\text{LEV}}$)	LEV y Position (\bar{Y}_{LEV})	LEV y Position (\bar{Y}_{LEV})	TEV Circulation ($\bar{\Gamma}_{\text{TEV}}$)	TEV x Position (\bar{X}_{TEV})	TEV y Position (\bar{Y}_{LEV})
Uncertainty [%]	0.82	4.75	0.74	1.12	4.45	2.80	1.02

3.11.4 Accuracy of Robotic Arm

To determine the accuracy of the robotic arm, the displacement error was calculated by an oscilloscope provided in the control unit, which is given in Figure 3.24. In the acceleration phase, the robotic arm displacement error decreased as the wing moved, whereas, in the constant velocity phase, it was approximately constant during the motion.

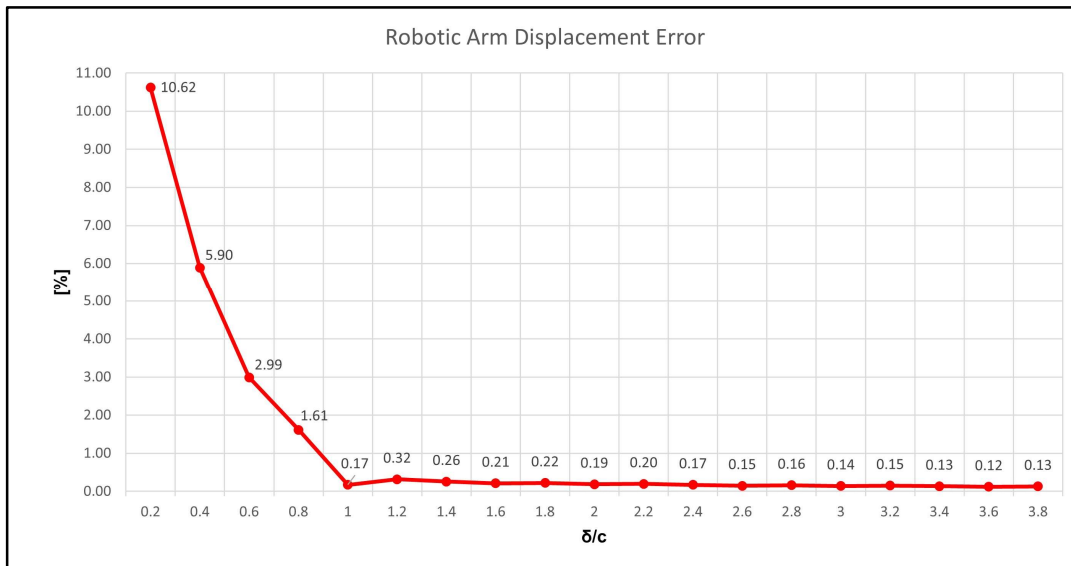


Figure 3.24. Robotic arm displacement error at each stage of the motion

CHAPTER 4

RESULTS AND DISCUSSION

In this chapter, the results of the experiments are presented. In the first two sections, variations of the geometric angle of attack and camber generation obtained at the 75% of span position are given. In the third section, the flow characteristics, which are divided into two parts as the out-of-vorticity and the velocity contours, are explained. In the fourth section, the characteristics of LEV and TEV are discussed in terms of circulation and vortex centroid. In the fifth section, the results obtained from this study are compared with the previous studies carried out by Meerendonk (2016), and Yazdanpanah (2019) for wings with different chordwise flexibility in revolving and translating motion, respectively.

4.1 Geometric Angle of Attack

The geometric angle of attack can be determined as an angle between the wing movement direction and the wing chord line connecting the leading edge and trailing edge (Figure 4.1).

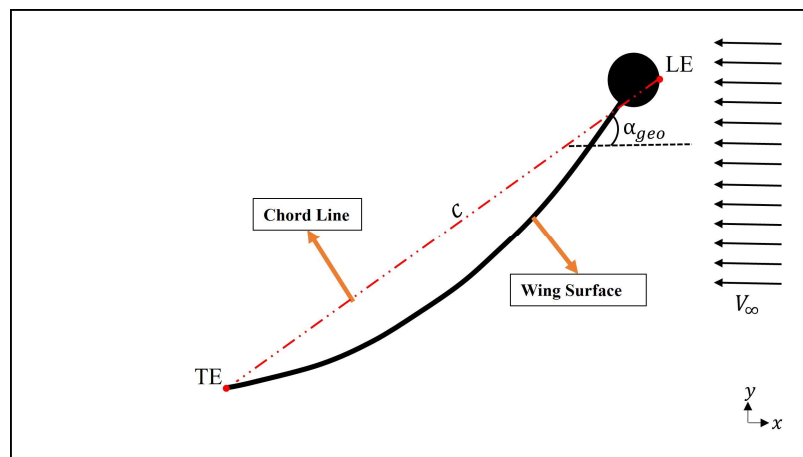


Figure 4.1. Geometric angle of attack

The geometric angle of attack can be calculated by the formula shown in Equation 4.1. To calculate the geometric angle of attack, the pixel values acquired from the PIV images are used as the position of leading and trailing edges.

$$\alpha_{\text{geo}} = \arctan\left(\frac{Y_{\text{LE}} - Y_{\text{TE}}}{X_{\text{LE}} - X_{\text{TE}}}\right) \quad (4.1)$$

The variation of the geometric angle of attack during the translating motion is given in Figure 4.2. According to the figure, as expected, the wings are deformed differently during the motion, since they have different chordwise flexibility provided by stiffeners placed on the wings' upper surface.

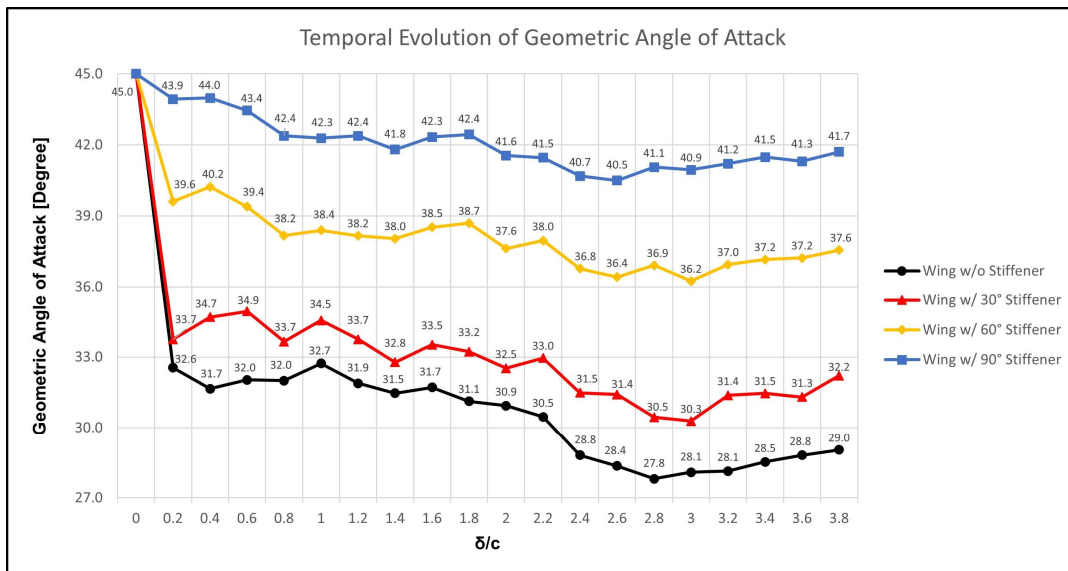


Figure 4.2. Variation of the geometric angle of attack

At the beginning of the motion ($0 \leq \delta^* \leq 0.2$), where the added mass effect is the dominant force that deforms the wing geometry, a sudden decrease in the geometric angle of attack is observed for the wing without a stiffener and the wing with 30° and 60° stiffeners because of the impulsive motion. That is, approximately 12.4° drop is obtained for the wing without a stiffener, whereas it becomes 11.3° and 5.4° for the wing with 30° and 60° stiffeners, respectively. Wing with 90° stiffeners, on the other hand, showed the lowest decrease in the geometric angle of attack. In the following stages of the acceleration phase of the motion ($0.2 \leq \delta^* \leq 1.0$), where the

influence of the circulatory terms became more significant on the wing deformation, the geometric angle of attack kept decreasing for the wings with 60° and 90° stiffener angles, whereas it was approximately constant for the wing without stiffener and the wing with 30° stiffener angle.

In the constant velocity phase ($1.0 < \delta^* \leq 3.8$) where the circulatory effects are the dominant forces deforming the wing surface, on the other hand, the decreasing tendency of the geometric angle of attack is observed for all wings. In the first part of this stage ($1.0 < \delta^* \leq 2.0$), the geometric angle of attack is reduced monotonically for the wing without stiffener and the wing with a 30° stiffener angle, whereas it was approximately constant for the wing with a 60° and 90° stiffener angle. In the middle part of this phase ($2.0 < \delta^* \leq 3.0$), the geometric angle of attack decreased for all wings and the minimum geometric angle of attack values was observed for each wing at the end of this part ($2.6 \leq \delta^* \leq 3.0$). The wing without a stiffener had the lowest geometric angle of attack (27.8°), whereas the wing with a 90° stiffener angle performed the highest geometric angle of attack (40.5°). Moreover, the wings with 30° and 60° stiffener angle generated the second lowest (30.3°) and third lowest (36.3°) geometric angle of attack, respectively. In the last part of this phase ($3.0 < \delta^* \leq 3.8$), the geometric angle of attack increased slightly for all wings.

According to Figure 4.2, it can be stated that the presence of the stiffener changes the wing chordwise flexibility by increasing the bending stiffness of the wing in the chord direction. Therefore, the wing without stiffener showed the lowest geometric angle of attack during the motion since it has the highest chordwise flexibility. Moreover, the stiffener orientation affects the chordwise flexibility of the wing. When the angle between the stiffener angle and the leading-edge increases, it enhances the wing bending stiffness. Therefore, the wing structure provides more resistance to wing deformation. As a result, among the wings with stiffeners, the wing with a 90° stiffener angle generated the highest geometric angle of attack during the motion since it has the highest bending stiffness in the chord direction,

whereas the wing with 30° performed the lowest geometric angle of attack because it has the highest chordwise flexibility.

During the motion, the average geometric angle of attack of the wings without a stiffener was approximately 31.1° on average, whereas, for the wings with a 30° , 60° , and 90° stiffener angle the average geometric angle of attack was 33.3° , 38.3° , and 42.1° , respectively. Compared to the wing without a stiffener, the average geometric angle of attack increased by almost 26.35%, 21.27%, and 8.60% for the wings with a 90° , 60° , and 30° stiffener angle, respectively.

In addition, the average geometric angle of attack is calculated as 34.3° and 29.9° for the wing without a stiffener in acceleration and constant velocity phase, respectively. The increments in the average geometric angle of the attack were approximately 21.21%, 16.45%, and 5.12% in the acceleration phase, and 28.55%, 23.32%, and 7.52% in the constant velocity phase, for the wings with a 90° , 60° , and 30° stiffener angle, respectively compared to wing without a stiffener. Therefore, it can be concluded that the presence of stiffener increases the geometric angle of attack during the motion. Furthermore, by altering the stiffener orientation, the bending stiffness of the wing in chord direction, thereby the change in geometric angle of attack, can be modulated.

4.2 Camber Generation

Camber is defined as the convexity of the curve of a wing surface from the leading edge to the trailing edge. It can be calculated as the distance between a point, P selected on the wing surface where the curve of the wing surface's first derivative is zero, and the wing chord line (Figure 4.3). Note that, since the wing surface is a thin flat plate the mean camber line is taken as the wing surface. Moreover, since the surface has its minimum point at point P, the maximum distance between the wing surface and the chord line is obtained.

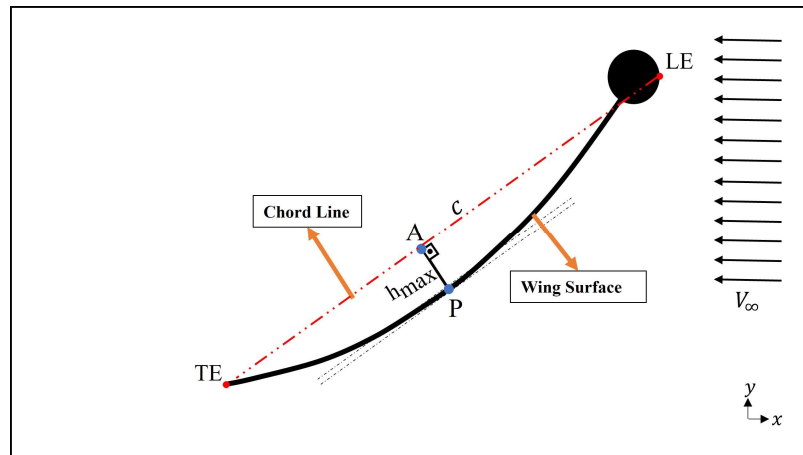


Figure 4.3. Wing camber

The camber can be calculated based on the formula given in Equation 4.2.

$$\text{camber \%} = \frac{h_{\max}}{c} \times 100 \quad (4.2)$$

Similar to the change in angle of attack, the camber is generated differently for the wings with different chordwise flexibility. That is, the wing without a stiffener showed the maximum camber generation because of the least force resistance capability to the motion. Wing with 90 degrees of the stiffener, on the other hand, produced the lowest camber since has the greatest bending stiffness value compared to the other wings tested. The wings with 30 and 60 degrees of stiffener have the second most and third most camber generation, respectively. Therefore, it can be stated that the stiffener orientation modulates the camber generation during the motion of the wing. The presence of the wing stiffener decreases the camber generation and the magnitude of the camber can be modulated by changing the stiffener orientation. The temporal variation of the magnitude of the camber generation is given in Figure 4.4. Note that, all wings are deformed to create negative camber in the chordwise direction, in which the amount of the negative camber formation depends on the chordwise flexibility provided by the stiffeners.

In the acceleration phase, ($0 \leq \delta^* \leq 1.0$), because of the added mass effect, even at the first stages of the movement ($0 \leq \delta^* \leq 0.2$), all wings showed sudden deformation in terms of camber because of the impulsive motion. The magnitude of the camber generation is altered depending on the wing chordwise flexibility. The wing without a stiffener, for example, displayed the highest camber generation (6.42%), whereas the wing with 90 degrees of stiffener angle generated the least camber (0.90%).

In the following stages of the acceleration phase ($0.2 \leq \delta^* \leq 1.0$), almost a 50% decrease in camber is observed for the wing without stiffener and the wing with a 30° stiffener angle. For the wings with 60° and 90° stiffener angle, on the other hand, the camber kept increasing. The camber was increased by approximately 20% for the wing with a 60° stiffener angle, whereas it almost doubled its value for the wing with a 90° stiffener angle.

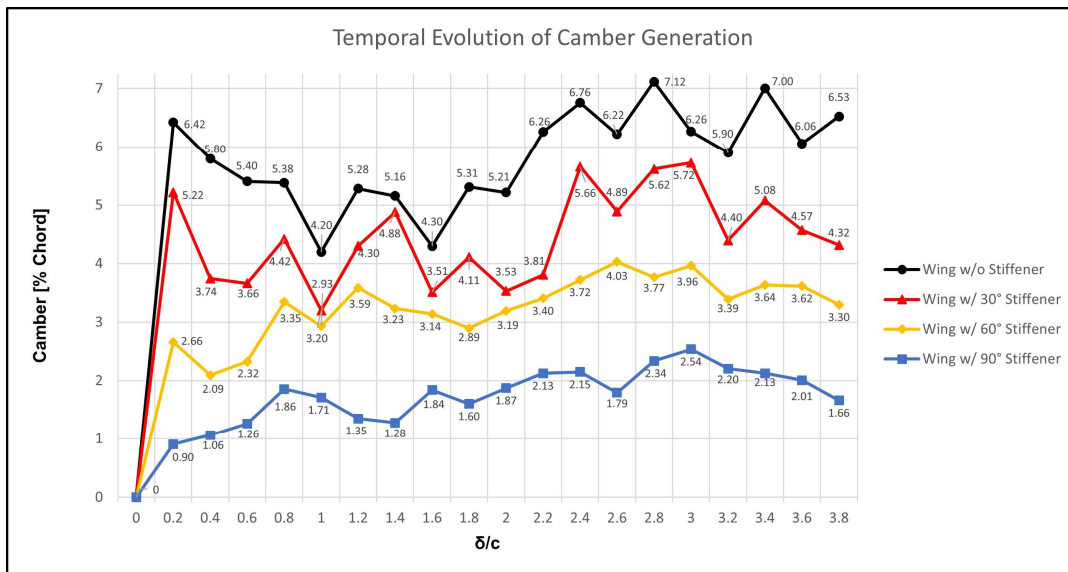


Figure 4.4. Variation of camber generation

In the constant velocity phase ($1.0 < \delta^* \leq 3.8$), on the other hand, the circulatory terms became the dominant force that deforms the wings since the effect of the added mass was diminished. In the first part of this phase of the motion ($1.0 < \delta^* \leq 2.0$),

the effect of the dominant force transition can be observed. According to Figure 4.4, the wings with 60° and 90° stiffener angle showed smooth variation in camber during this transition, whereas for the wing without stiffener and wing with 30° stiffener angle the camber changed abruptly. In the middle part of this phase ($2.0 < \delta^* \leq 3.0$), for all wings, the camber kept increasing and all wings reached their maximum camber generation at the end of this part ($2.6 \leq \delta^* \leq 3.0$). In general, similar to the acceleration phase, the wings generated camber depending on their chordwise flexibility. The wing without a stiffener showed the maximum camber generation (7.12%), whereas the wing with a 90° stiffener angle performed the lowest one. Moreover, for the wings with 30° and 60° stiffener, the maximum value of the camber became 5.72% and 4.03%, respectively. In the last part of this phase ($3.0 \leq \delta^* \leq 3.8$), for all wings the camber generation showed decreasing tendency. To visualize the graph better, the sixth-order polynomial curve fitting algorithm was employed to camber generation data. The curve-fitted version of Figure 4.4 is given in Figure 4.5.

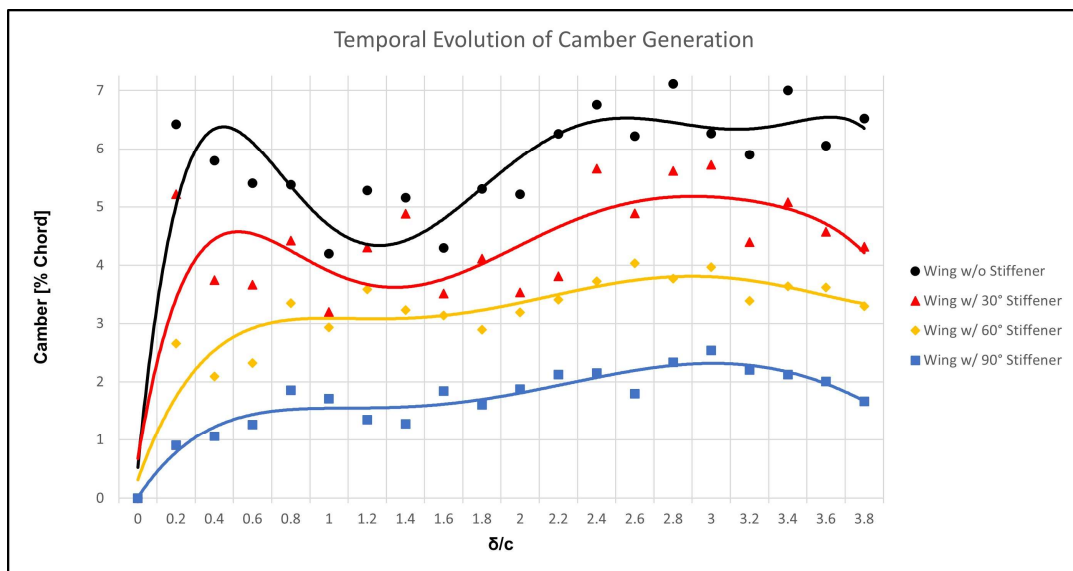


Figure 4.5. Curve-fitted version of variation of camber generation

During the motion, the average camber generation in magnitude was 5.52% c for the wing without a stiffener, whereas, it was 4.23% c, 3.11% c, and 1.7% c for the wing

with a 30°, 60°, and 90° stiffener angle, respectively. Compared to the wing without a stiffener, the average camber in magnitude decreased by 23.46%, 43.73%, and 69.53% for the wings with a 30°, 60°, and 90° stiffener angle. During the acceleration phase reduction of camber in magnitude became 25.59%, 50.92%, and 75.01%, whereas it was calculated as 22.77%, 41.38%, and 67.74% in the constant velocity phase, respectively.

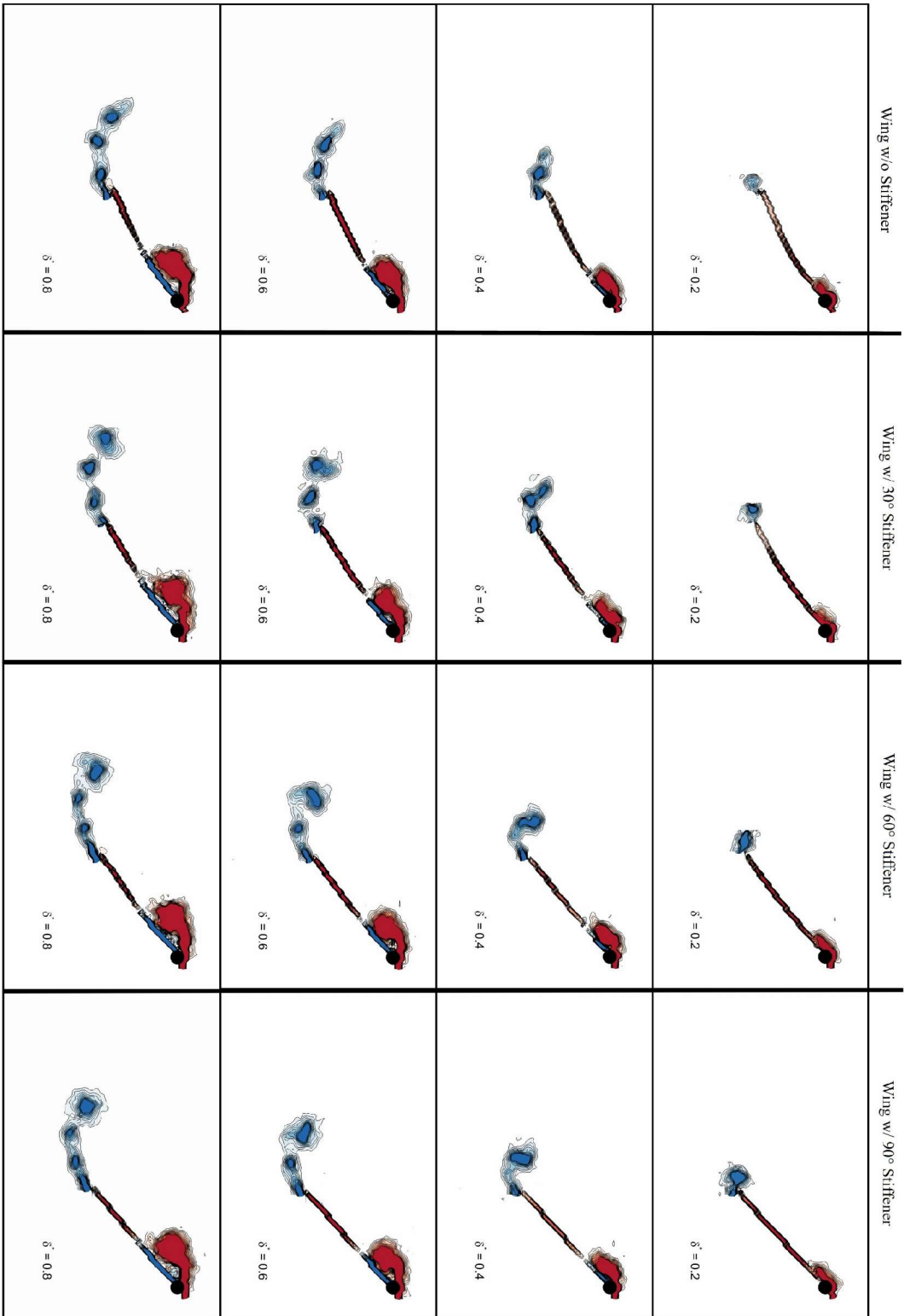
According to the results, it can be stated that the stiffener orientation influences the camber generation during the motion. Even the presence of the stiffener decreases the magnitude of the negative camber generation. In other words, although the magnitude of the camber is reduced, the camber generation increase in the positive direction. As the angle between the stiffener and the leading edge increases, the camber generation decrease because of an increase in chordwise bending stiffness.

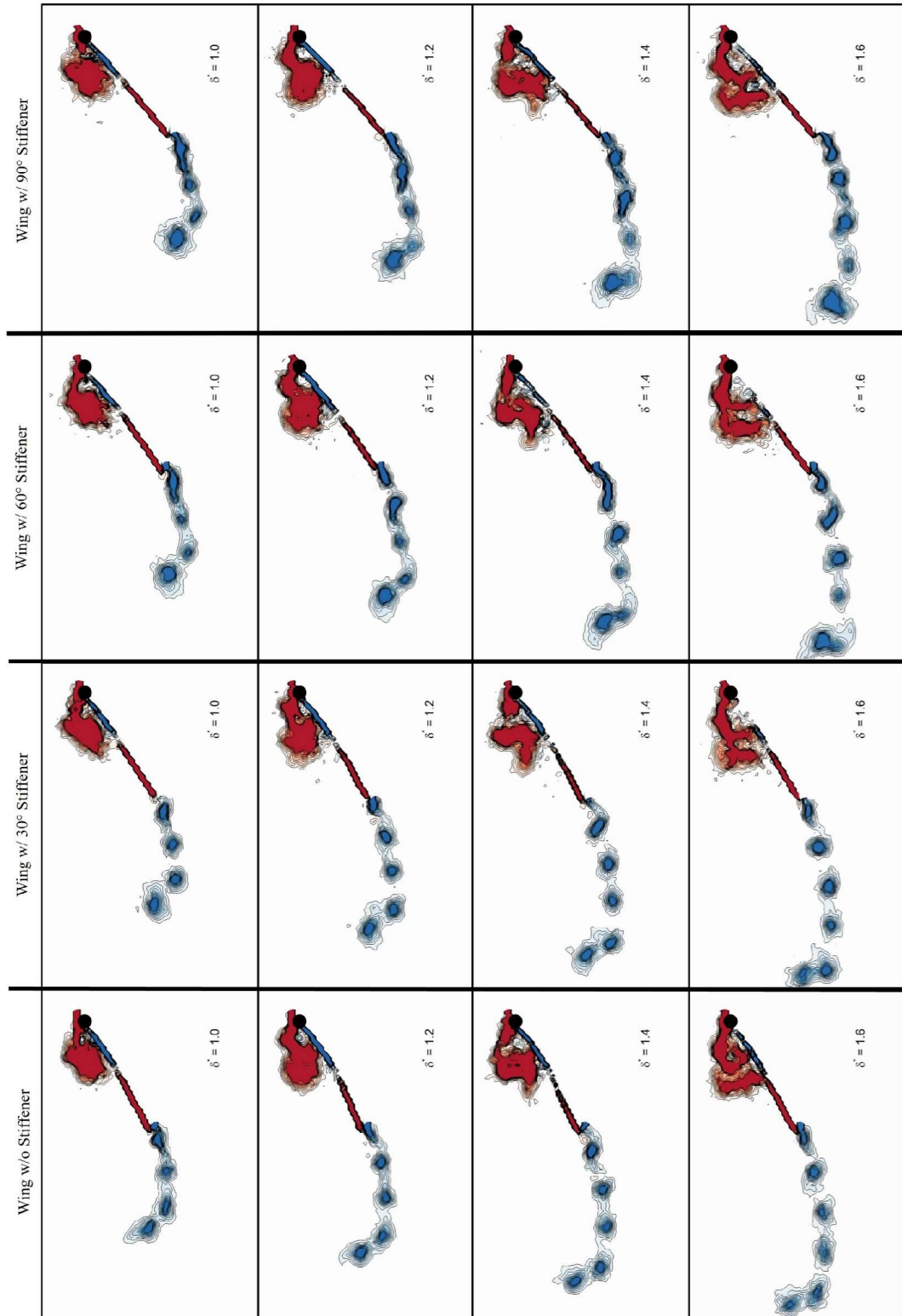
Note that, for all phases of the motion, the camber generation changed abruptly for the wing without stiffener and the wing with a 30° stiffener angle, whereas smooth alteration is observed for the wings with a 60° and 90° stiffener angle. This may be observed because the wing without stiffener and the wing with a 30° stiffener angle have the least resistance capability to wing deformation. Therefore, their deformation characteristics are more sensitive to the flow field around the wing than the wings with 60° and 90° stiffener. That is, because of the high deformability, the wing structures of those wings may tend to respond to all changes in the flow field around the wing surface. The wings with 60° and 90° stiffener angle, on the other hand, may be more resistive to the change in flow field around the wing because of their bending stiffness in the chordwise direction provided by the stiffeners.

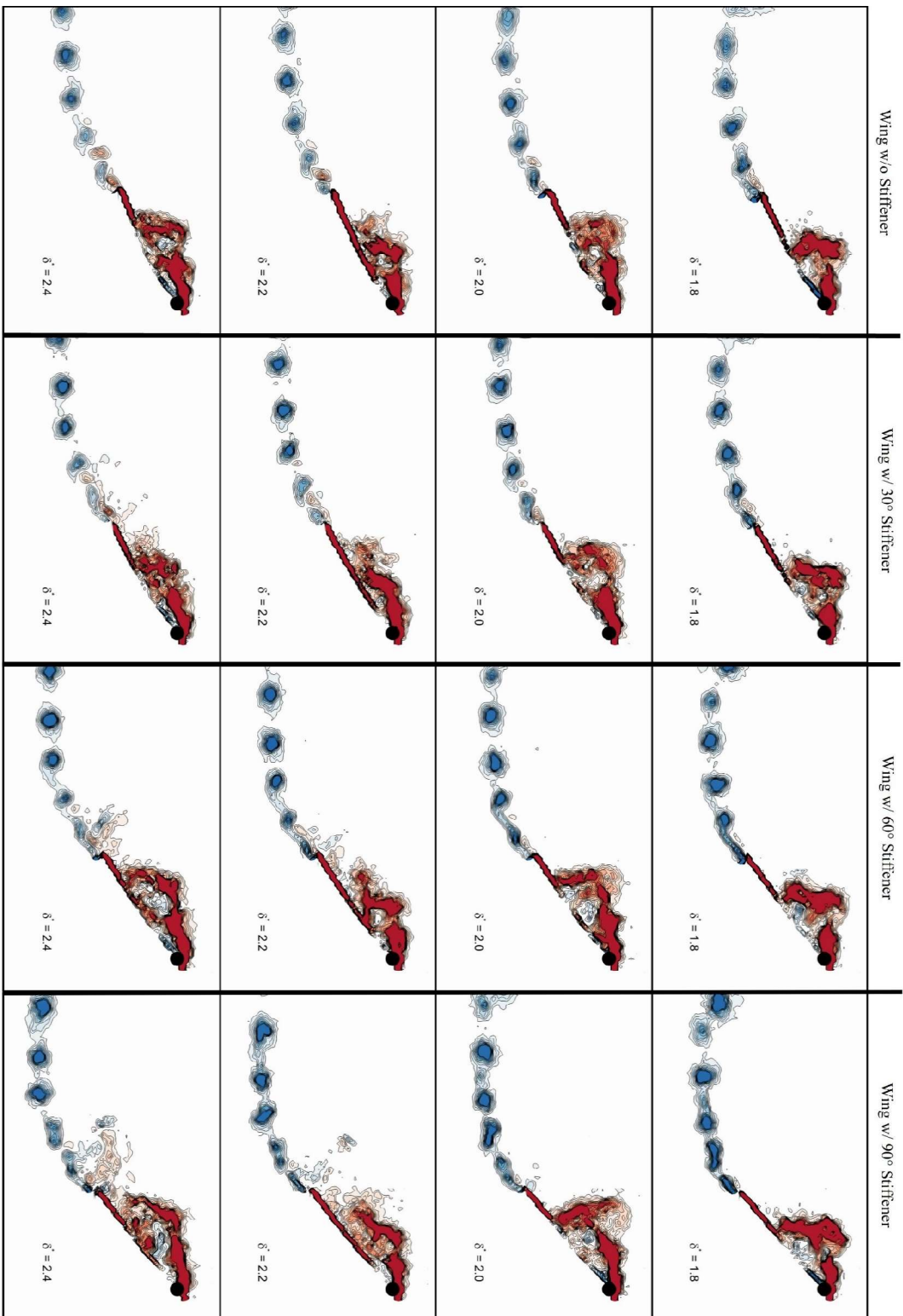
4.3 Flow Characteristics

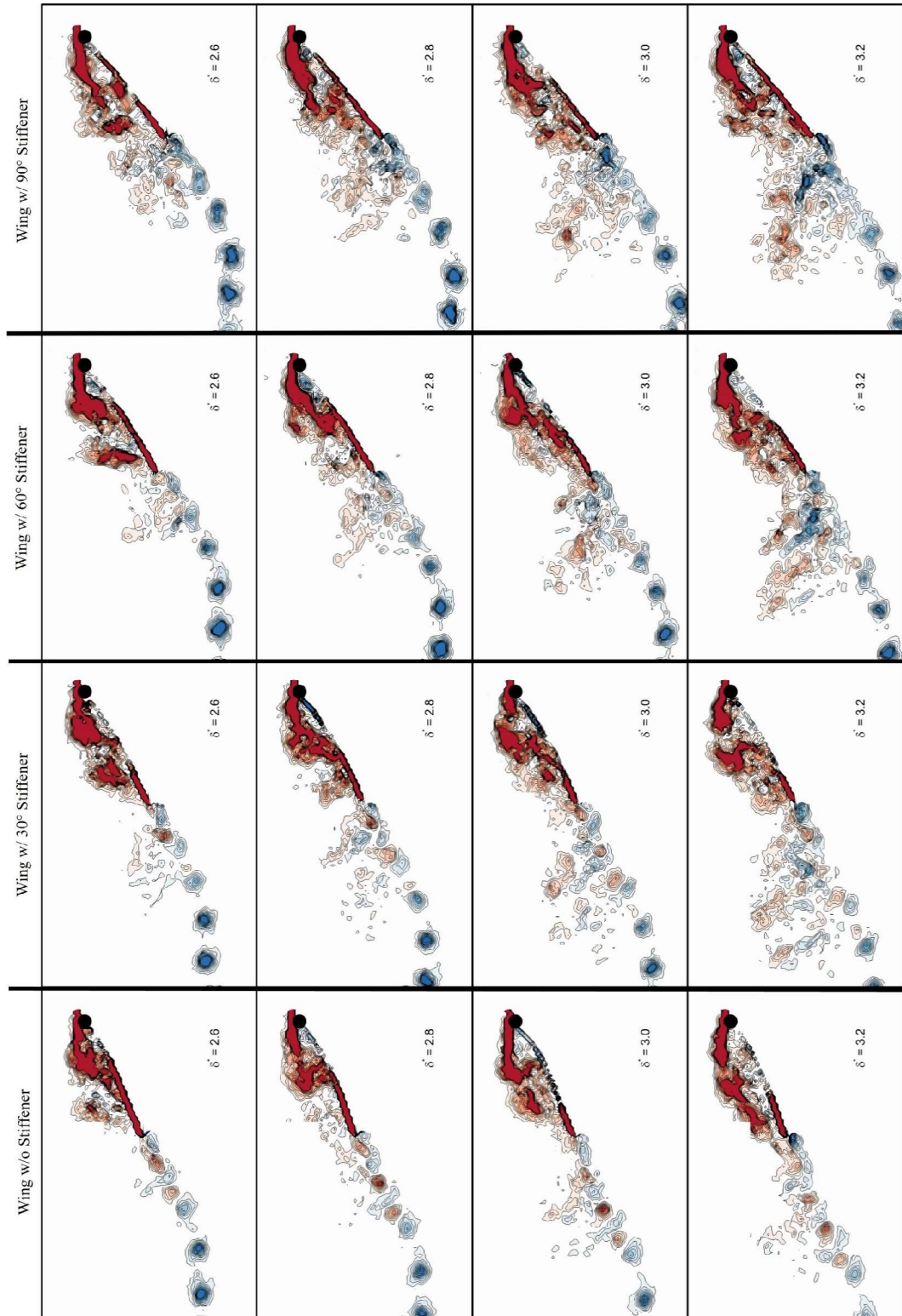
For all wings tested, the out-of-plane vorticity at the 75% wingspan positions was calculated and out-of-plane vorticity contours are given in Figure 4.6. According to Figure 4.6, it can be said that at the initial phases of the motion, a coherent leading-

edge vortex was formed for all the wings tested in the experiment and LEV remained stable over a long period of movement. For approximately 2.4 chord lengths of travel ($0 \leq \delta^* \leq 2.4$), the flow fields of vortical structures have similar characteristics for all wings. However, after 2.4 chords length of travel ($2.4 < \delta^* \leq 3.8$), the vortical structures started to be distinguished from each other because of the different geometric angle of attack and camber generation depending on the wings' chordwise flexibility, which is modulated by the stiffener angle. At $\delta^* = 2.4$, for example, for wings with a 60° and 90° stiffener angle, the shear layers that emanated from the LE and TE started interacting with each other, which results in the formation of small-scale vorticity structures in the wake. This interaction is observed after 2.6 and 3.0 chord lengths of travel for a wing with a 30° stiffener angle and a wing without a stiffener, respectively. These interactions of the shear layers continued until the end of the motion, which results in a more chaotic flow in the wake during the time. Note that, after 3.0 chord lengths of travel ($3.0 < \delta^* \leq 3.8$), fully chaotic flow in the wake is observed for the wings with a 60° and 90° stiffener angle. Among all wings tested, the wing without a stiffener generated less chaotic flow in the wake because of the smaller geometric angle of attack. Furthermore, since the wing re-aligns in the flow direction with ease, the closest LEV motion to the surface is observed around the wing without a stiffener. It is followed by the wings with a 30° and 60° stiffener angle. Expectedly, the LEV could not remain a close motion to the surface of the wing with a 90° stiffener angle. Therefore, it can be concluded that the presence of the stiffener influences the flow field around the wing by providing additional bending stiffness in the chordwise direction, which increases the geometric angle of attack of the wing compared to its flexible counterparts. Moreover, by altering the stiffener orientation, a flow field with different characteristics around the wing can be obtained.









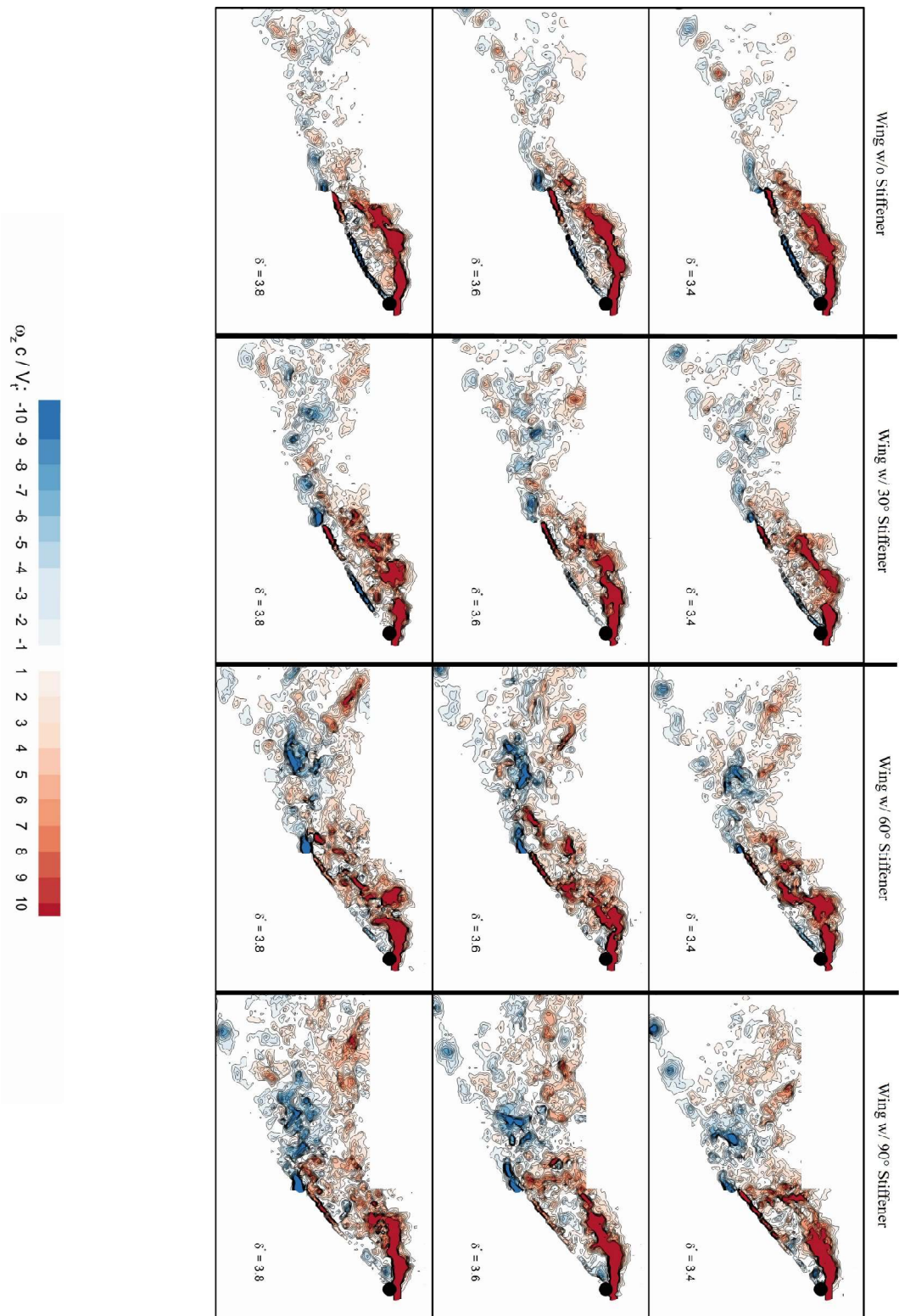
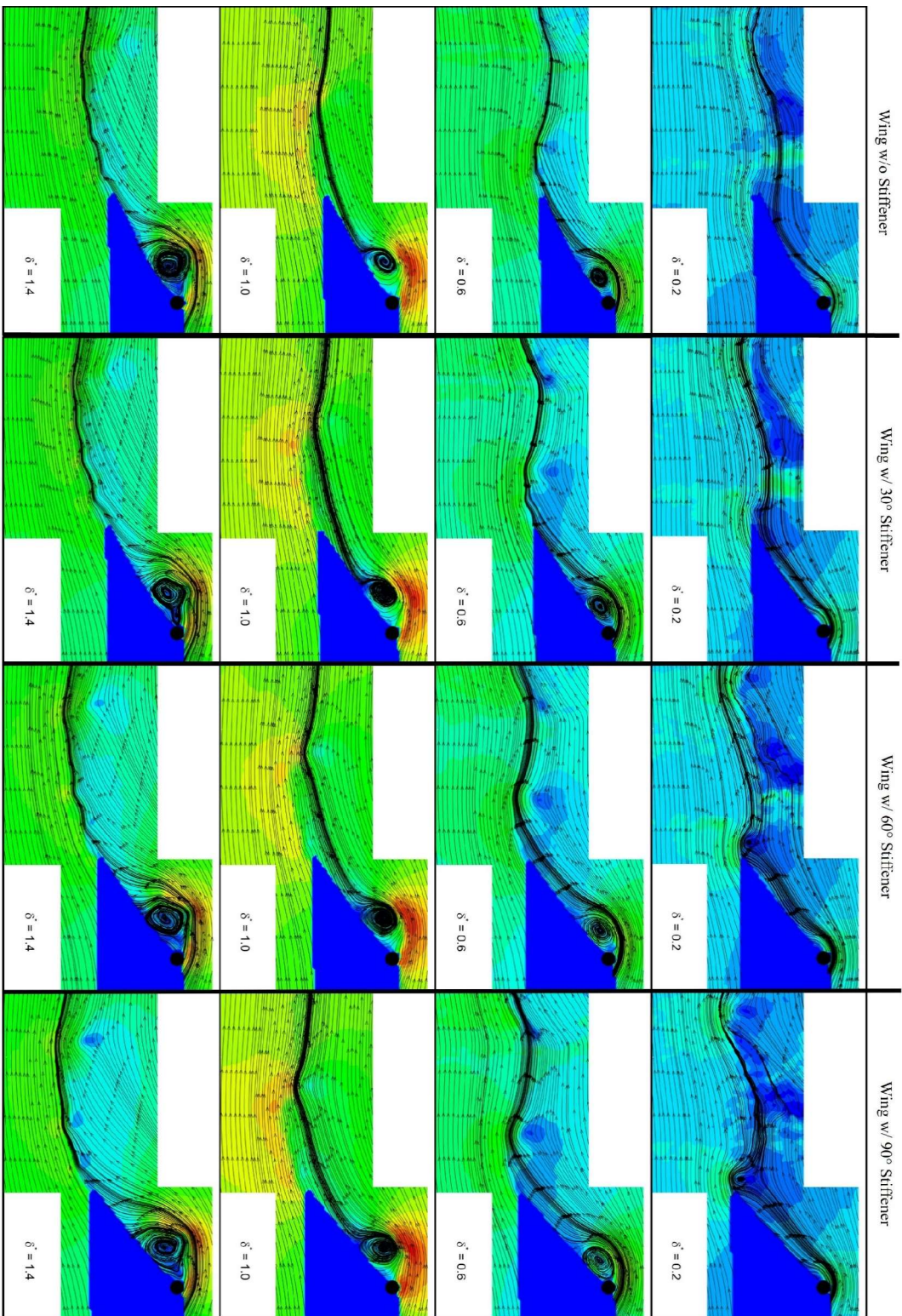
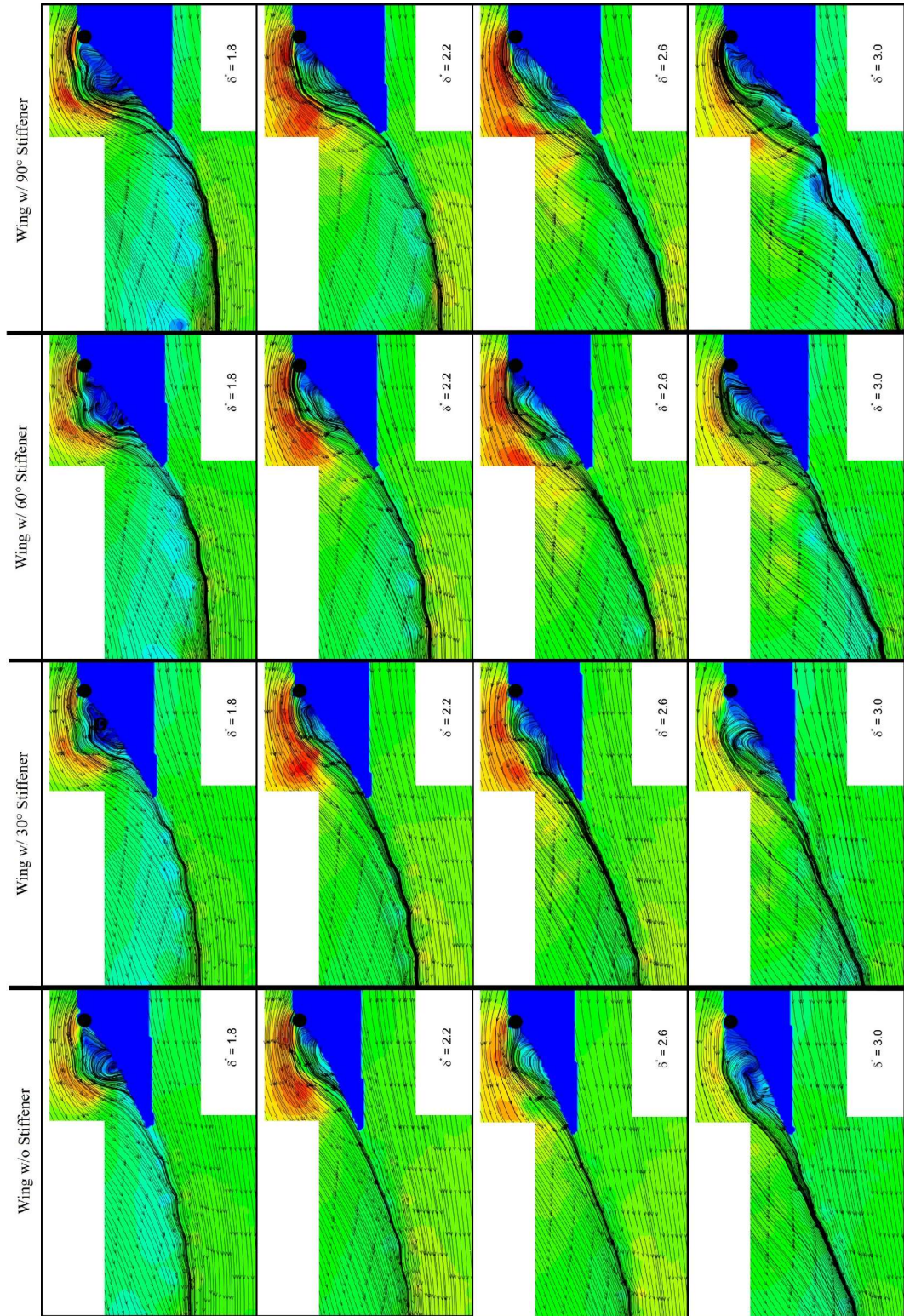


Figure 4.6. Out-of-vorticity contours

For all wings tested, the velocity contours and the streamlines at the 75% wingspan positions are given in Figure 4.7. In the initial stages of the acceleration phase ($0 \leq \delta^* \leq 0.6$), an attached leading-edge vortex formation was observed for all wings tested. Throughout the acceleration phase ($0 \leq \delta^* \leq 1.0$), the LEV kept attached to the surface for all wings, therefore the flow was not detached from the surface, whereas, in the constant velocity phase the flow remained attached to the surface and left the trailing edge tangentially for a 3.0 chord length of travel ($0 \leq \delta^* \leq 3.0$) for all wings tested. However, after 3.4 chord length of travel ($3.4 \leq \delta^* \leq 3.8$), because of the LEV staying close to the trailing edge, the flow detached from the surface for the wing without a stiffener. This situation was observed for wings with a 30° and 60° stiffener angle after 3.8 chord length of travel ($3.8 \leq \delta^*$).





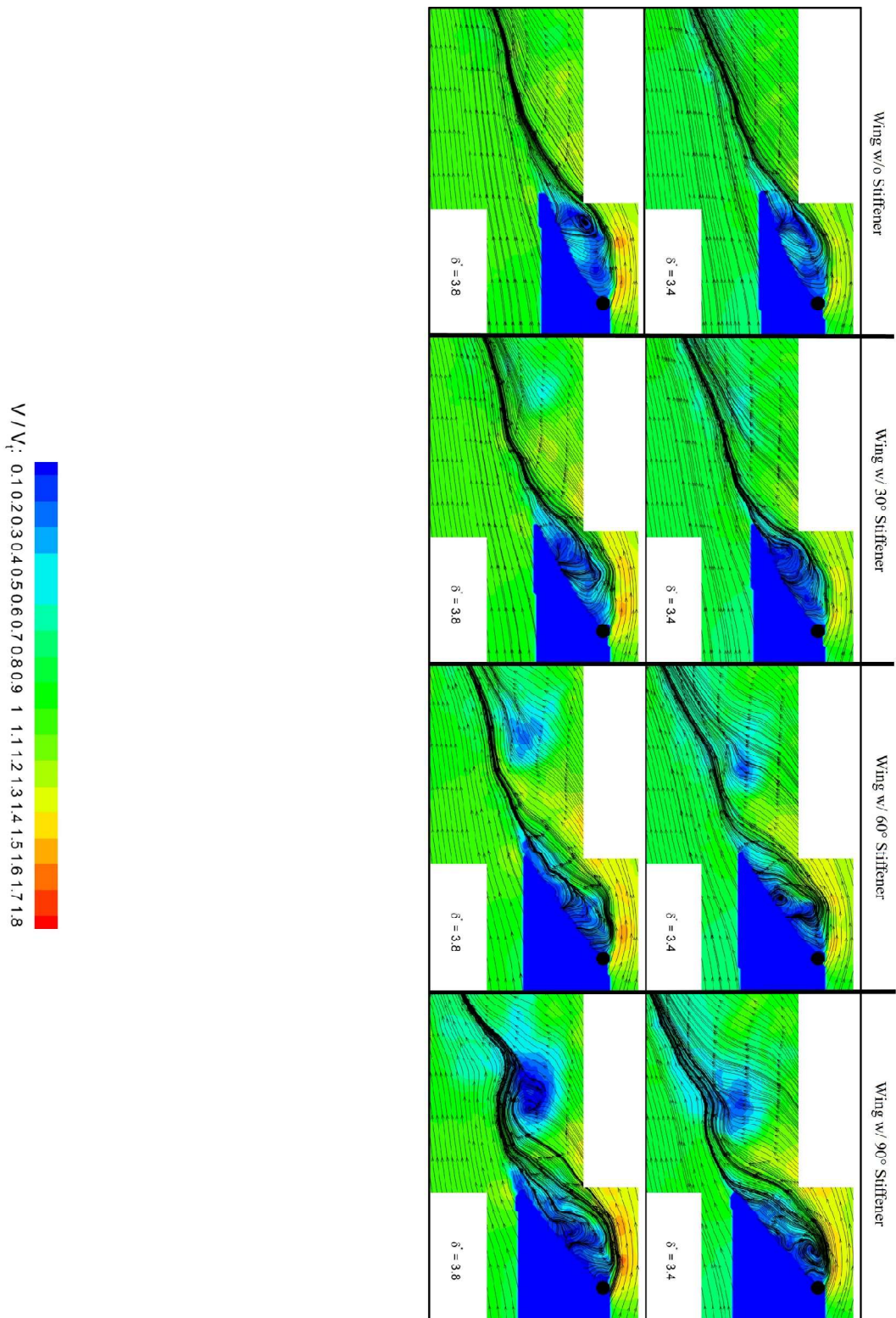


Figure 4.7. Velocity contours and streamlines

4.4 LEV & TEV Characteristics

4.4.1 LEV Circulation

The schematic representation of the LEV circulation is given in Figure 4.8. Note that, the LEV circulation is non-dimensionalized by the wing chord length and the terminal velocity.

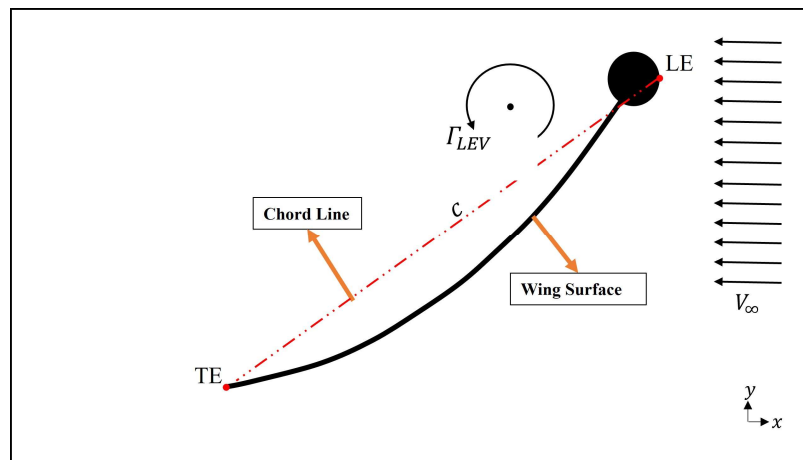


Figure 4.8. LEV circulation

The variation of LEV circulation during the motion is given in Figure 4.9. At the acceleration phase of the motion ($0 \leq \delta^* \leq 1.0$), the LEV circulation increases monotonically for all wings with an approximately constant slope. Expectedly, at that instant wing with the 90° stiffener generates the highest LEV circulation value, which is followed by the wing with 60° stiffener producing the second highest one. In addition, the wing without a stiffener and the wing with 30° stiffeners revealed similar circulation values. Note that, during the acceleration phase, the LEV circulation is built up rapidly for all wings tested.

At the beginning of the constant velocity phase of the motion ($1.0 < \delta^* \leq 1.4$), the LEV circulation kept increasing for all wings. After 1.4 chord lengths of travel of the wing ($1.4 < \delta^*$), all wings revealed a similar trend in terms of LEV circulation, which is approximately constant during the motion. However, the magnitude of the

LEV circulations is distinguished from each other depending on the existence of the stiffener and the stiffener angle, which modulates the chordwise flexibility, thereby the effective angle of attack and camber generation.

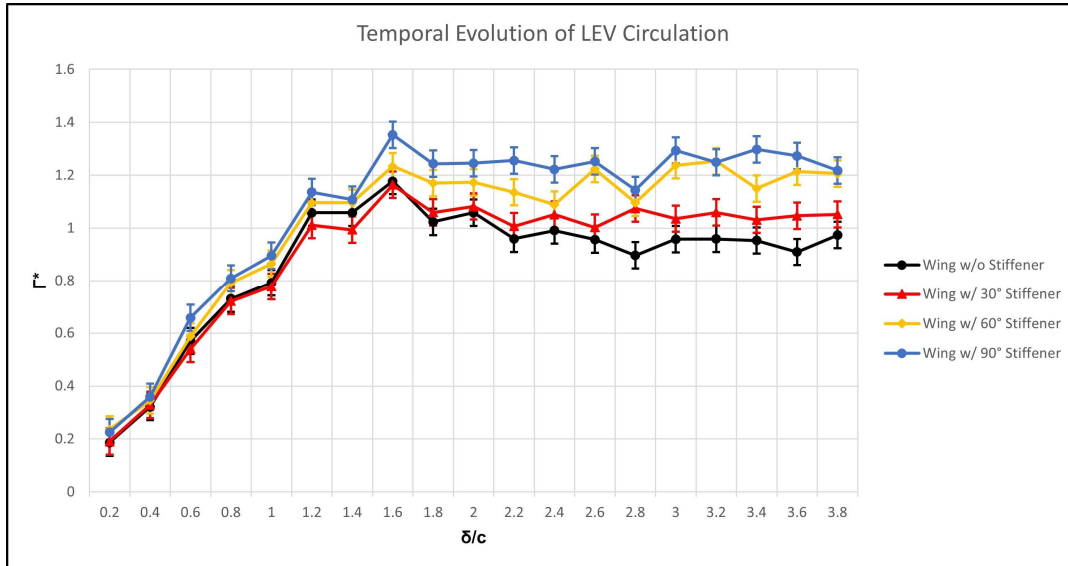


Figure 4.9. Variation of LEV circulation

Among the wings with stiffeners, the wing with 90° stiffener, which has the greatest bending stiffness in the chordwise direction, generated the highest LEV circulation, in which it is again followed by the wing with 60° stiffener that has the second biggest bending stiffness value in the chordwise direction. Wing with 30° stiffener having the least bending stiffness, on the other hand, produced the lowest LEV circulation value. Therefore, it can be clearly stated that the orientation of the stiffeners affects the flow field around the wing in terms of LEV circulation. By altering the angle between the stiffener and the leading edge, the circulation value of the LEV can be modulated. When the angle between the stiffener and the leading edge increases, it enhances the bending stiffness of the wing in the chord direction providing a higher geometric angle of attack formation during the motion, which results in greater LEV circulation.

Furthermore, the average non-dimensional LEV circulation produced by the wing without a stiffener was 0.87, whereas it became 1.07, 1.01, and 0.91 for the wings

with a 90°, 60°, and 30° stiffener angle. Therefore, compared to the wing without a stiffener, approximately 17.97%, 13.14%, and 4.03% enhancements in average LEV circulation are observed.

In addition, according to Figure 4.9, LEV circulation around the wings with 60° and 90° stiffeners, for example, are quite close to each other, although the wing with 60° stiffener completed its motion with a smaller geometric angle of attack formation. In the acceleration phase, the average reduction in LEV circulation is approximately 3.07%, whereas, in the constant velocity phase it becomes almost 6.16% when the stiffener orientation is changed from 90° to 60°. Throughout the whole motion, the LEV circulation produced by the wing with a 60° stiffener angle is 5.34% less than the wing with a 90° stiffener angle. The geometric angle of attack, on the other hand, is diminished significantly when the stiffeners are oriented at 60° rather than 90° by approximately 9.37% and 9.75% in the acceleration phase and constant velocity phase, respectively. Throughout the whole motion, the wing with a 60° stiffener angle completed its motion with 9.65% less in the geometric angle of attack formation than the wing with a 90° stiffener angle. Therefore, it can be concluded that by altering the stiffener angle it is possible to obtain similar LEV circulation, which can be achieved with a higher bending stiffness, with a smaller geometric angle of attack formation reducing the drag force generated. As a result, an increment in the L/D ratio, which enhances the aerodynamic efficiency, can be achieved by modulating the stiffener orientations.

Similarly, although the wing with a 30° stiffener angle generated lower LEV circulation than the wing with a 60° stiffener angle, it completed its motion with a smaller geometric angle of attack. That is, the wing with a 30° stiffener angle produced approximately 10.23% and 9.25% less LEV circulation on average than the wing with a 60° stiffener angle in the acceleration phase and constant velocity phase, respectively. Throughout the whole motion, approximately 9.51% less LEV circulation on average is generated by the wing with a 30° stiffener angle than the wing with a 60° stiffener angle. The geometric angle of attack, however, is reduced by 12.35% and 14.41% in the acceleration phase and constant velocity phase of the

motion, respectively as the stiffener orientation is tilted from 60° to 30° . It can be stated that a smaller geometric angle of attack formation, thereby smaller trailing edge generation diminishing the drag force, can be achieved by decreasing the stiffener orientation with a small penalty in LEV circulation.

Therefore, this result proves that even the presence of the stiffener enhances the LEV circulation and by altering the stiffener orientation the LEV circulation can be managed.

4.4.2 TEV Circulation

TEV circulation and centroid measurements were only carried out for only 1.4 chord length of travel ($0 \leq \delta^* \leq 1.4$), because after that the starting vortex was no longer in the field of view (Figure 4.10). Note that, the TEV circulation is non-dimensionalized by the wing chord length and the terminal velocity.

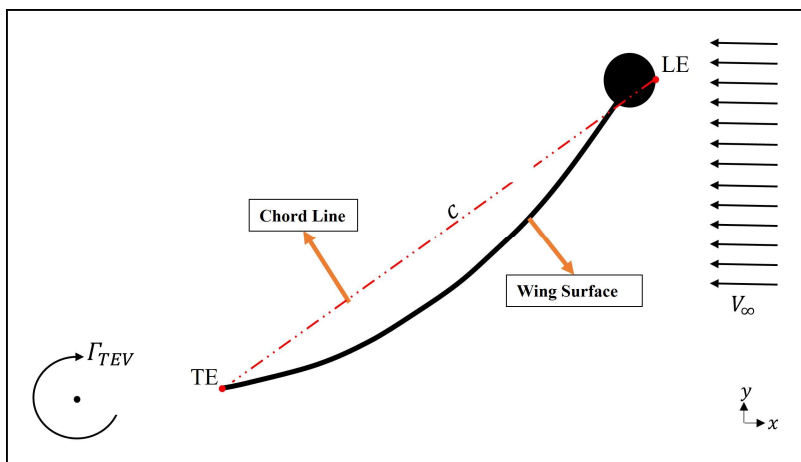


Figure 4.10. TEV circulation

Expectedly, the wing with the 90° stiffener generated the highest TEV, whereas the wing without a stiffener produced the lowest one. Wing with 60° stiffener and 30° stiffener generated the second and third biggest TEV circulation values, respectively. Note that, as the chordwise flexibility increases, the wing realigns in the flow direction with ease resulting in a smaller geometric angle of attack formation as

shown in Figure 4.2. Therefore a smaller TEV is required to re-establish the Kutta condition, which can be seen in Figure 4.11. Moreover, when the angle between the stiffener and the leading edge increases, because of the higher geometric angle of attack formation, higher TEV circulation is observed. Therefore, it can be concluded that the stiffener orientation affects the TEV circulation and by altering the stiffener orientation the magnitude of the TEV circulation can be modulated.

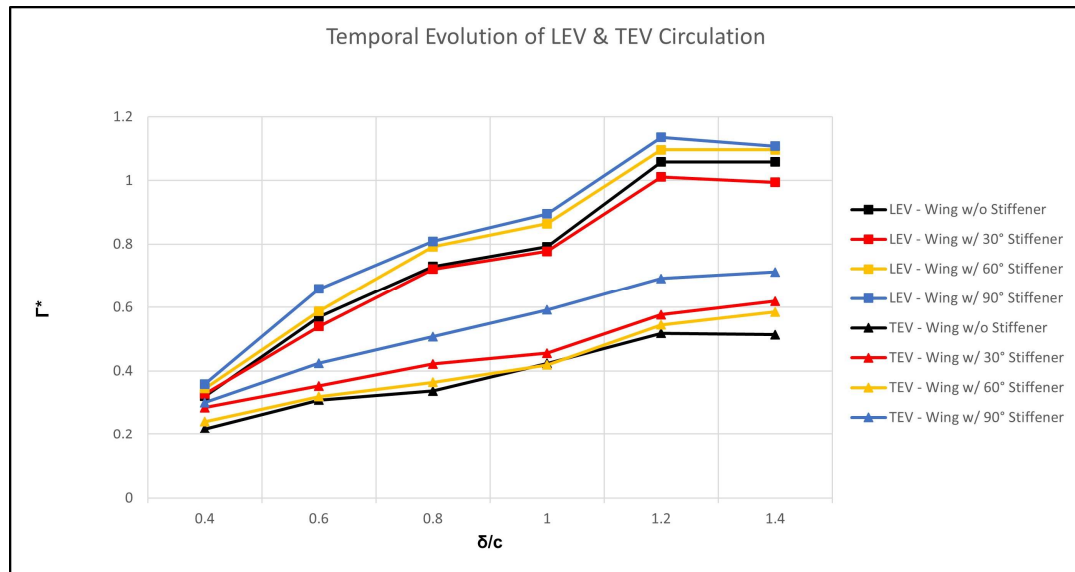


Figure 4.11. Variation of LEV & TEV Circulation

In addition, According to Figure 4.11, it can be stated that LEV circulation, on the other hand, is quite correlated with the TEV at the initial phase of the motion of the wing ($0 \leq \delta^* \leq 1.4$). This relation may suggest that a bound circulation or another circulation source is required to satisfy Kelvin's circulation theorem, which is consistent with Yazdanpanah's (2019) study. In addition, it can be concluded that the LEV and TEV circulations are related to each other and higher TEV circulation results in higher LEV circulation.

Note that, although LEV and TEV have opposite directions thereby oppositely signed magnitudes, to compare the LEV and TEV properly, the TEV circulation values are multiplied by -1.

4.4.3 LEV Position

As aforementioned, the position of the LEV centroid in the x and y axes are calculated separately by the γ_1 function (Figures 4.12 and 4.15). The results are non-dimensionalized by the wing chord length.

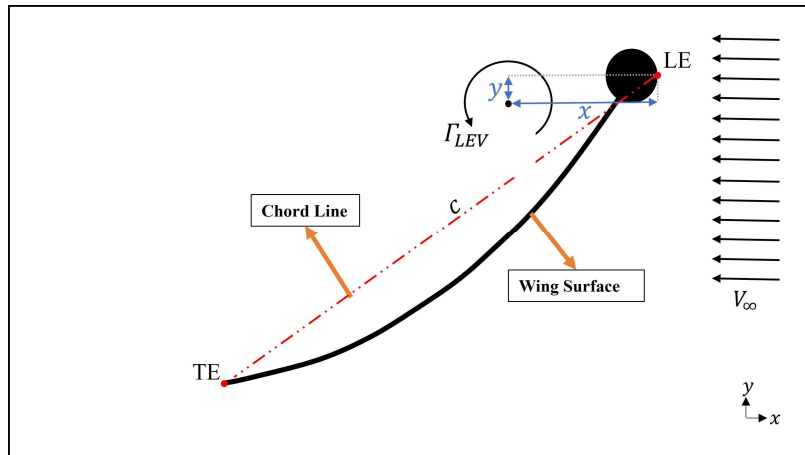


Figure 4.12. LEV centroid

In Figures 4.13 and 4.14, the temporal variation of the LEV centroid in the y and x axes for each wing is given, respectively. In Figure 4.16, on the other hand, the total distance between the LEV centroid and the leading edge is shown.

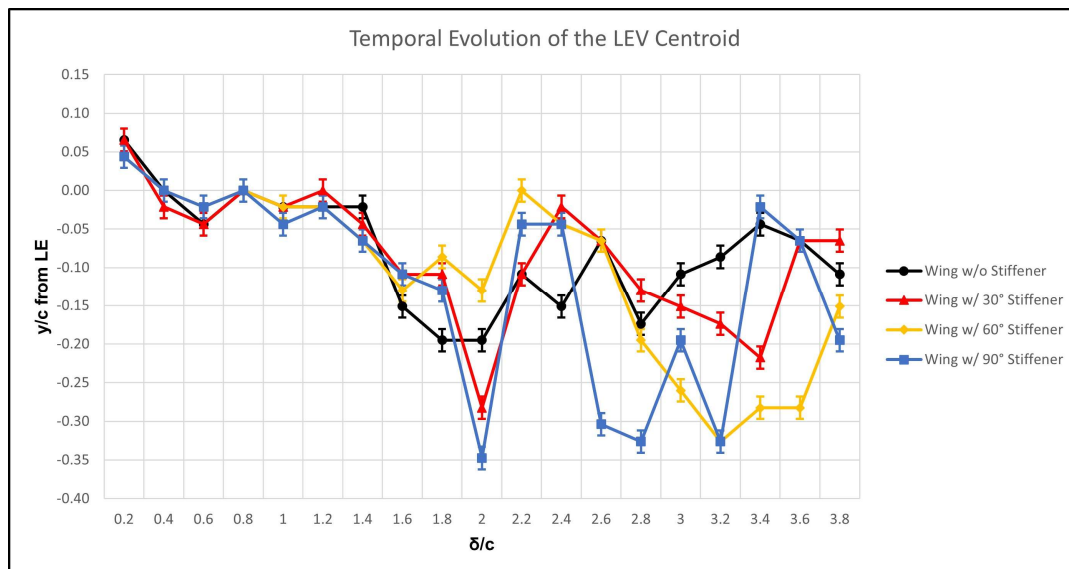


Figure 4.13. Variation of the LEV Centroid in the y-axis

According to Figures 4.13, 4.14, and 4.16, it can be stated that in the acceleration phase of the motion ($0 \leq \delta^* \leq 1.0$), the LEV centroid has the same movement relative to the leading edge. In constant velocity phase ($1.0 < \delta^* \leq 3.8$), on the other hand, at the beginning of the motion ($1.0 < \delta^* \leq 1.6$), the LEV centroid in the y-axis had a similar trajectory. However, they were differentiated from each other after 1.8 chord length of travel. In contrast, the positions of the LEV centroid in the y-axis converged each other at the end of the motion ($\delta^* = 3.8$).

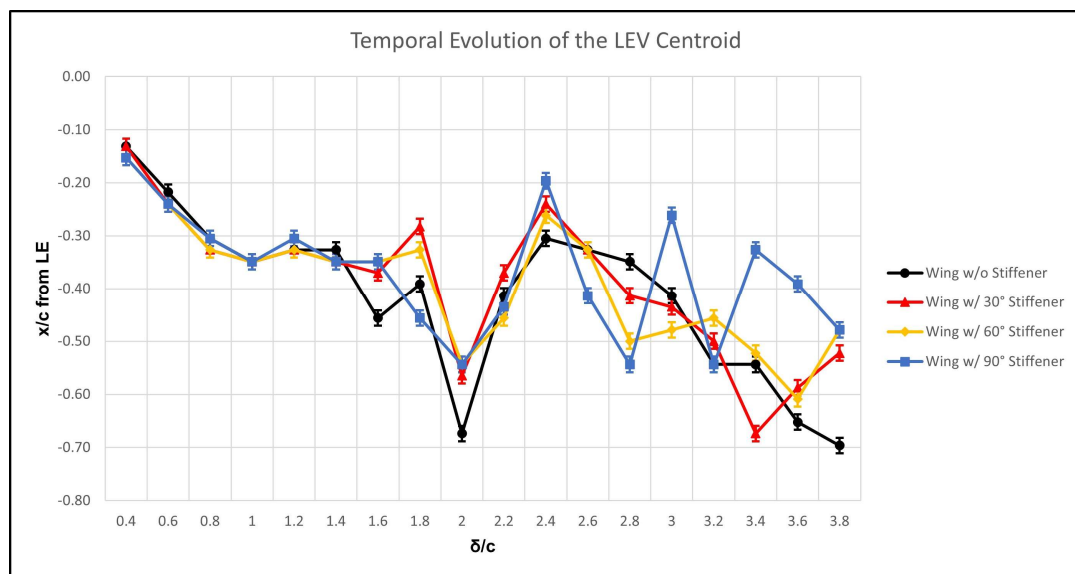


Figure 4.14. Variation of the LEV Centroid in the x-axis

In the x-axis, on the other hand, the position of the LEV centroids remains similar for a 2.8 chord length of travel ($1.0 < \delta^* \leq 2.8$). After 2.8 chord length of travel, the position of the LEV centroid of the wing without a stiffener and with a 30° and 60° stiffener angle changes with a similar trend for 0.6 chord length of travel ($2.8 < \delta^* \leq 3.4$). At the end of the motion ($3.6 \leq \delta^* \leq 3.8$), the position LEV centroid of the wings with a stiffener converged with each other, whereas for the wing without a stiffener, the LEV centroid was positioned at a far distance in the x-axis.

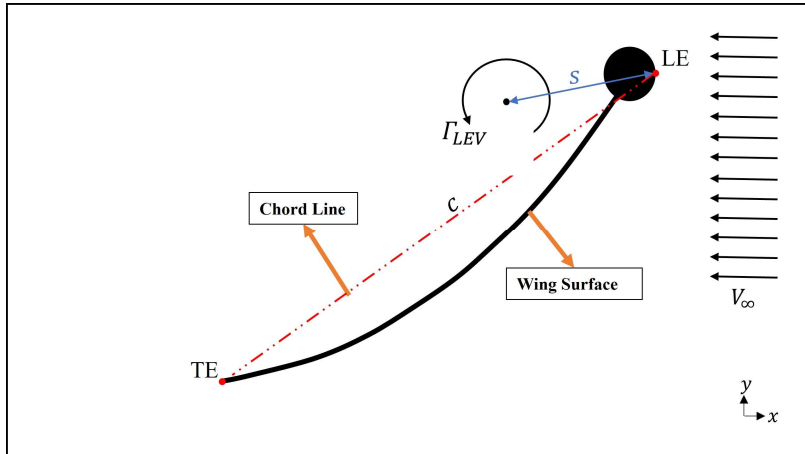


Figure 4.15. The total distance between the LEV centroid and the leading edge

The total distance between the LEV centroid and the leading edge was approximately the same for wings without a stiffener and wings with a 30° and 60° stiffener. For the wing with a 90° stiffener, on the other hand, while the total distance was calculated in the same way as the other wings, the length started to change suddenly after 2.8 chord length of travel ($2.8 < \delta^* \leq 3.8$).

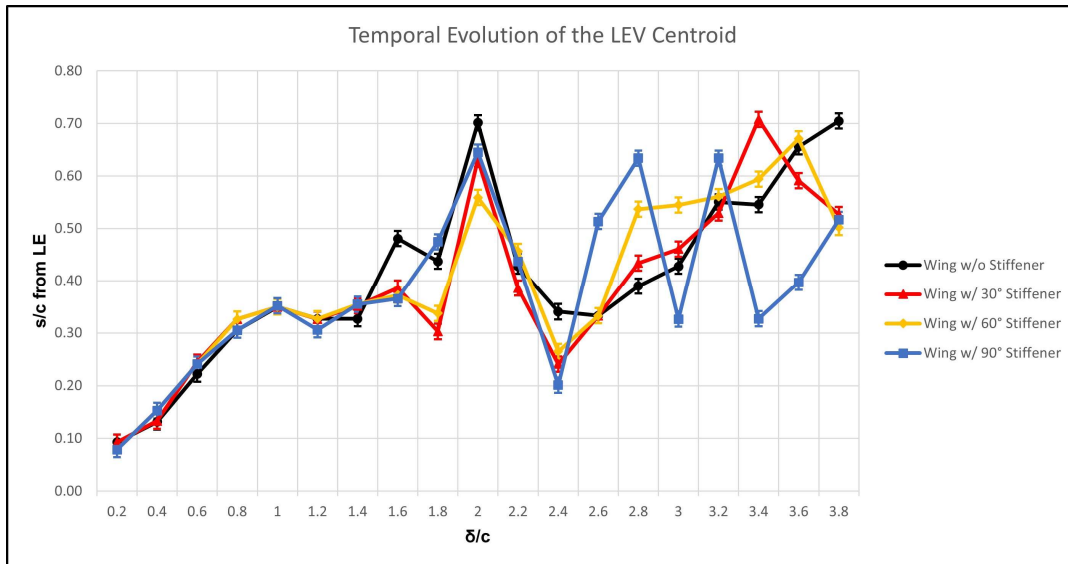


Figure 4.16. Variation of the distance between the LEV centroid and the leading edge

4.4.4 TEV Position

Similar to the LEV position, the position of the TEV centroid was calculated by γ_1 function in the y and x axes, separately (Figures 4.17 and 4.20). Note that, for TEV centroid calculations, only the starting vortex is tracked.

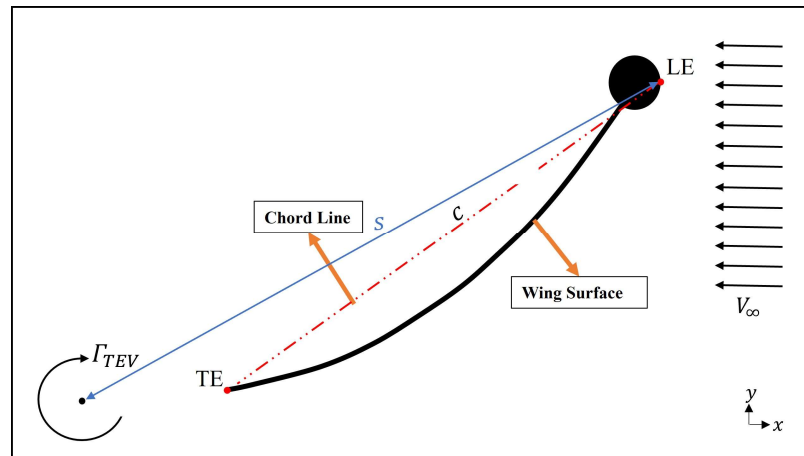


Figure 4.17. TEV centroid

The variations of TEV centroids in the y and x axes are given in Figure 4.18, and Figure 4.19, respectively. In Figure 4.21, on the other hand, the total distance between the TEV centroid and the LE is shown. Note that, the TEV centroid was calculated for 1.4 chord length of travel since after that the TEV is no longer in the field of view and the calculations were carried out for starting vortex only. Moreover, the 3D movement of the TEV was neglected.

The TEV positions in the x-axis showed the same trend throughout the motion, whereas the position of the TEVs in the y-axis are distinguished from each other. As aforementioned, the position of the trailing edge changes during the motion because of the chordwise flexibility, which affects the geometric angle of attack. Since the trailing edge vortex is formed at the trailing edge, the position of the TE is crucial for the TEV trajectory.

Note that, as the geometric angle of attack decreases, the distance between the trailing edge and leading edge decreases in the y-axis, whereas it increases in the x-

axis. During the motion, the biggest deflection of the trailing edge was observed for the wing without a stiffener since it has the most compliant trailing edge to the upcoming flow, and deflection was reduced from the wing with a 30° stiffener to 90° stiffener.

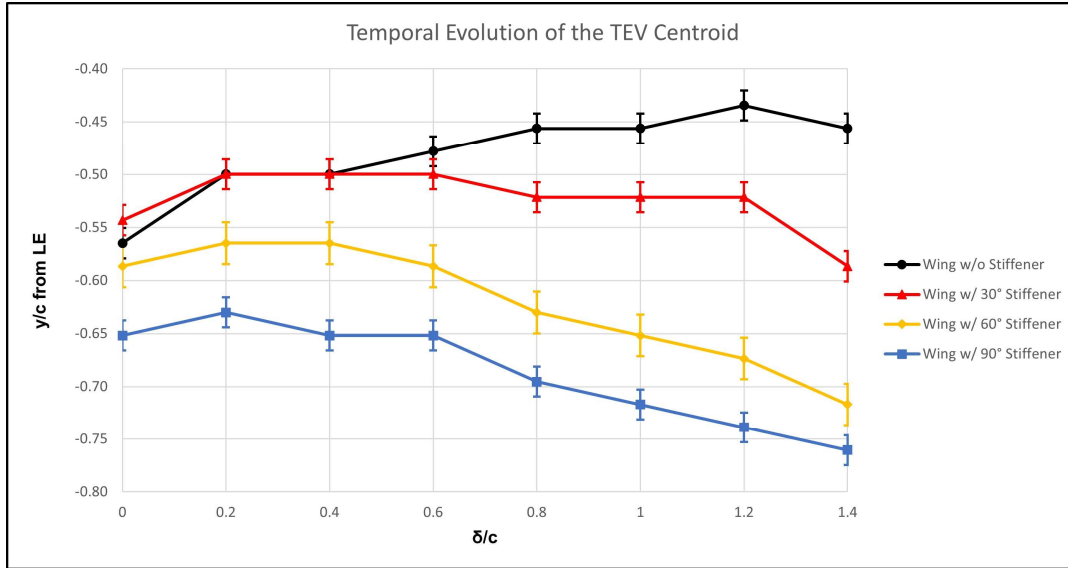


Figure 4.18. Variation of the TEV Centroid in the y-axis

Therefore, throughout the motion, in the y-axis, the TEV centroid for the wing without a stiffener was positioned in the closest position for the wing without a stiffener, compared to the other wings. Similarly, among the wings with a stiffener, the distance between the TEV centroid and the leading edge decreased from the wing with a 90° stiffener to a 30° stiffener.

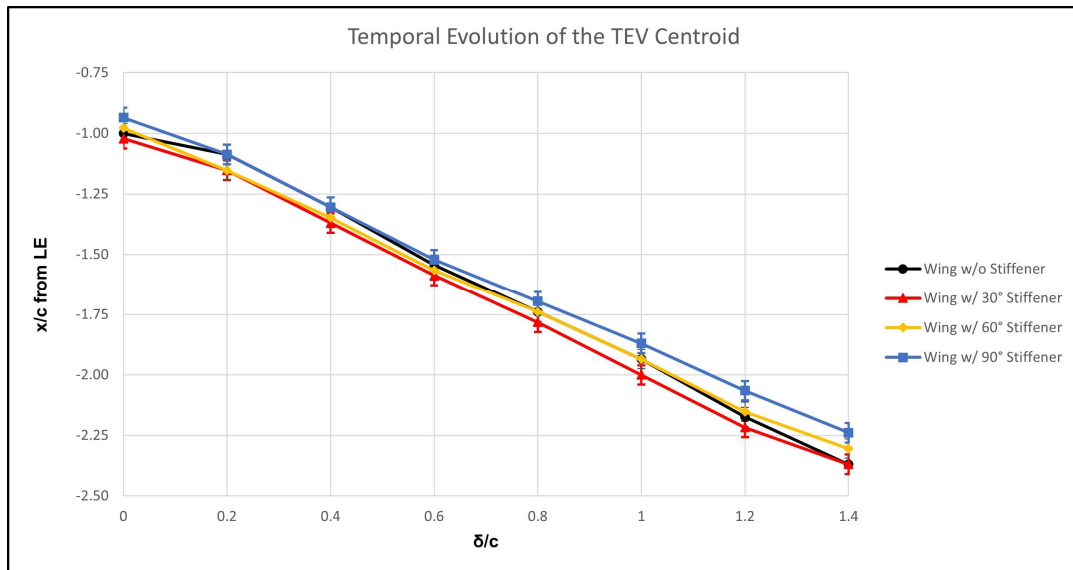


Figure 4.19. Variation of the TEV Centroid in the x-axis

In the x-axis on the other hand, throughout the motion, the TEV centroid was in the closest position to the LE for the wing with a 90° stiffener, whereas the biggest distance was measured for the wing with a 30° stiffener.

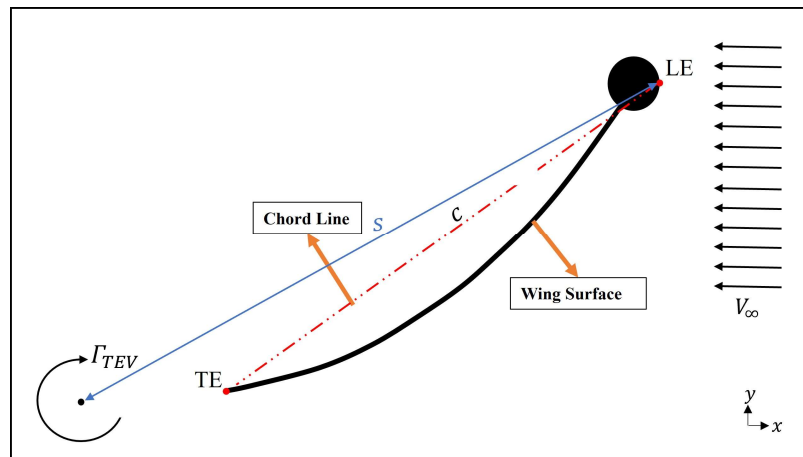


Figure 4.20. The total distance between the TEV centroid and the LE

Furthermore, the total distance between the TEV centroid and the LEV was calculated as approximately the same for all wings. Therefore, it can be concluded that, although the position of the TEV centroid with respect to the LE changes in the

y and x axes differently, the total distance between the TEV centroid and LE remains approximately constant for the tested wings.

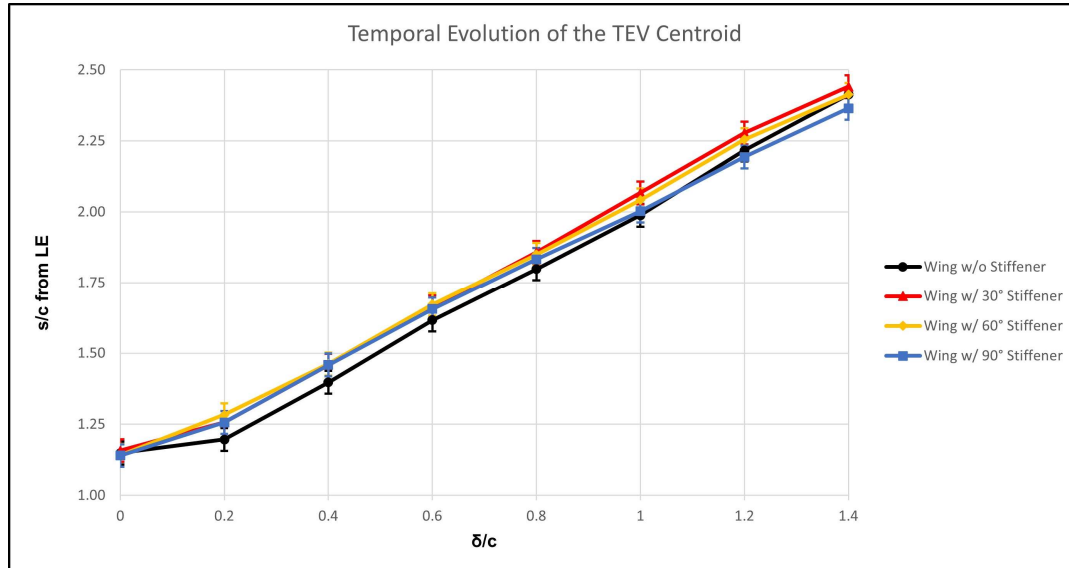


Figure 4.21. Variation of the distance between the TEV Centroid and the trailing edge

4.5 Comparison with previous studies

In this section, the comparisons with the previous studies that are performed by Yazdanpanah (2019) and Meerendonk (2016) are presented. The results showed that wings are deformed according to their chordwise flexibility. That is, the wing without a stiffener having the highest chordwise flexibility showed the biggest deformation in the chordwise direction with the smallest geometric angle of attack and greatest camber in magnitude generation. Among the wings, on the other hand, the geometric angle of attack increased and the magnitude of the camber was reduced as the chordwise flexibility decreased from the wing with a 30° stiffener to a 90° stiffener. The LEV circulation, on the other hand, was influenced by the chordwise flexibility provided by the stiffeners. The presence of the stiffener increased the LEV circulation and an increment in stiffener angle resulted in enhancement of LEV circulation. Therefore, the highest LEV circulation was generated by the wing with

a 90° stiffener, whereas the wing without a stiffener produced the lowest LEV circulation. These results are consistent with the studies carried out by Meerendonk (2016) and Yazdanpanah (2019) in terms of geometric angle of attack and LEV circulation. In contrast to Yazdanpanah’s study, there is no sudden drop in LEV circulation observed in wings with a 60° and 90° stiffener, which have the second highest and highest chordwise rigidity compared to the tested wings and completed their movement at 38.3°, and 42.1° angle of attack on average, respectively.

Note that, as aforementioned, the wings perform deformations because of the forces acting on the wing surface. At the beginning of the acceleration phase ($0 \leq \delta^* \leq 0.2$), the wings deformed by the inertial-reaction forces, which are nothing but the added mass term. While keeping accelerating, the wing deformed because of the added mass and circulatory terms ($0.2 < \delta^* \leq 1.0$). In the constant acceleration phase ($1.0 < \delta^* \leq 3.8$), because of the motion without an acceleration the effect of added mass was eliminated and the LEV deforms the wings surface, only. Therefore, it can be concluded that the magnitude of the camber is proportional to the resultant force generated around the wing. The generation of camber in magnitude can be expressed as a function of the resultant force acting on the wing surface as follows:

Note that, the angular deformation of a beam because of the torque applied to it is defined as the angle of twist (Beer et al., 2019), and its magnitude is proportional to the beam length and torque applied, whereas it is inversely proportional to the modulus of rigidity, G of the beam material and the polar moment of inertia, J of the beam cross-section, which is given in Equation 4.3.

$$\varphi = \frac{TL}{JG} \quad (4.3)$$

Assume that, the leading edge is straight and has a uniform circular crosssection, the leading edge deforms elastically and the twist along the leading edge is uniform. Therefore, under these assumptions, according to Equation 4.3 the angle of twist of the leading edge can be derived as:

$$\varphi_{LE} = \frac{F_R d_R 2c}{J G} \quad (4.4)$$

where, F_R is the resultant force acting on the wing surface, d_R is the distance between the leading edge and the point where the resultant force is applied, $2c$ is the length of the leading edge, J is the polar moment of inertia of the leading edge, and G is the modulus of rigidity of the leading edge.

By putting Equation 4.4 into Equation 2.3, the camber can be expressed as a function of the resultant force acting on the wing surface as follows:

$$\begin{aligned} \text{Camber} &= \frac{2 F_R d_R c}{J G} \frac{c}{\tan\theta} \quad (4.5) \\ &= \frac{2 c^2}{J G \tan\theta} F_R d_R \\ &= \frac{2 c^2}{J G \tan\theta} F_R d_R \end{aligned}$$

$$\therefore \text{Camber} = f(F_R) \quad (4.6)$$

The resultant force generated by the wings with different chordwise flexibility in revolving motion was measured by Meerendonk (2016). Note that the wings started accelerating from rest for one chord length of travel ($0 \leq \delta^* \leq 1.0$), and after that kept revolving with a constant rotational velocity ($1.0 < \delta^*$). The variation of the resultant force coefficient during the motion is given in Figure 2.22 b.

According to Figure 4.22 b, it can be stated that the resultant force generated around the wing surface increased as the chordwise bending stiffness increased. The variation of the resultant force coefficient showed a similar trend for all wings tested.

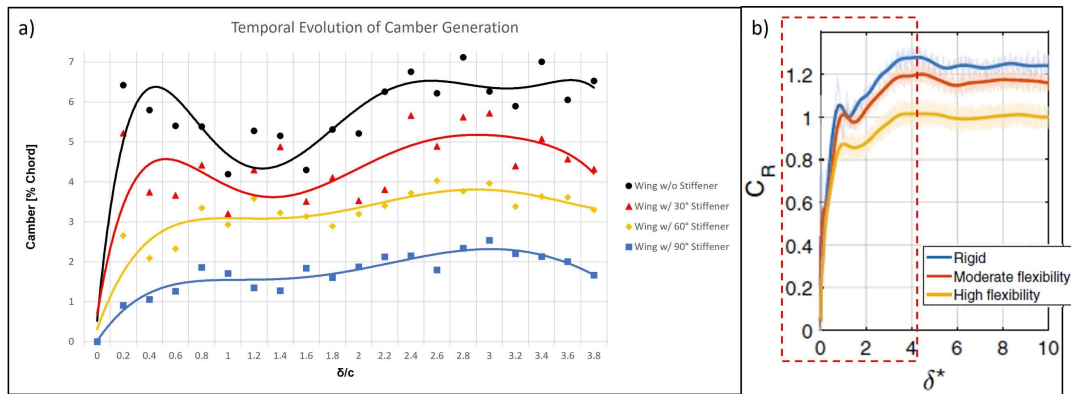


Figure 4.22. a) Variation of camber generation in magnitude, b) Variation of resultant force coefficient during the revolving motion (Adapted from Meerendonk, 2016)

At the beginning of the acceleration phase of the motion ($0 \leq \delta^* \leq 1.0$), the resultant force acting on the wing surface was enhanced monotonically with a constant slope. At the earlier phase of the accelerating motion ($0 \leq \delta^* \leq 0.2$), because of the added mass term the camber increased drastically. According to Meerendonk (2016), the added mass term, whose magnitude was proportional to the acceleration, acted normal to the wing surface. Since the flexible wings deformed during the motion, the component of the acceleration was tilted from the wing normal, whereas it remained constant for the rigid wings. Therefore, in the acceleration phase of the motion ($0 \leq \delta^* \leq 1.0$), the rigid wing produced the highest force generation, whereas the lowest force was generated by the highly flexible wing. Moreover, at the beginning of the constant velocity phase ($1.0 \leq \delta^* \leq 1.2$), the contribution of the added mass was eliminated since wings were translating with no acceleration. Therefore, the resultant force acting on the wing surface decreased slightly for all wings tested. After that, for three-chord lengths of travel of the wings ($1.2 < \delta^* \leq 4.0$), because of the development of the LEV on the wing surface, the net force generated was enhanced significantly for all wings tested. Similar to the acceleration phase, the rigid wing produced the highest force, whereas the lowest force was measured for the highly flexible wing. After four chord lengths of travel of the wings ($4.0 < \delta^*$), the net force produced decreased slightly and became almost constant

for all wings because the wings achieved their approximately steady-state conditions (Meerendonk, 2016).

According to Figure 4.22, it can be stated that the variation of the camber in magnitude for the wing without a stiffener obtained in this study showed a similar trend to the variation of the resultant force generated by three wings tested by Meerendonk (2016). By assuming that a similar force generation will be observed for the translating and revolving wings, which have common motion kinematics (i.e., acceleration phase for one chord length of travel and constant velocity phase for at least three chord length of travel), it can be expected that the variation of the resultant force acting on the wing surface may also be similar during the translating and the revolving motions. Therefore, it can be concluded that the chordwise flexibility reduces the net force production because of a smaller geometric angle of attack and a greater camber in magnitude formation during the translating motion. As a result, the wing without a stiffener, which has the lowest geometric angle of attack and the highest camber, generated the smallest force during the experiments. In the acceleration phase, for example, a smaller force value was transmitted to the force measurement sensor, and the force generated by the wing was dumped because of the wing deformation forming a high camber. In the following phases of the motion, where the added mass effect was completely diminished, due to the lower geometric angle of attack the wing without a stiffener kept producing less force compared to the wings with a stiffener, which have an additional bending stiffness provided by the stiffeners. The wing with a 90° stiffener, on the other hand, completed its motion with the highest geometric angle of attack and the smallest camber in magnitude, which resulted in the highest force generation. Moreover, since the energy loss for the wing deformation was the smallest, the highest force value was transmitted to the force measurement sensor.

Note that, based on this assumption the variation of the net force acting on the wing surface during the translating motion may be explained in detail. In the acceleration phase ($0 \leq \delta^* \leq 1.0$), because of the added mass and the circulatory terms around the

wing surface, the net force generated increases drastically with an almost constant slope. At the beginning of the constant velocity phase ($1.0 < \delta^* \leq 1.2$), the resultant force decreased slightly because the wing started moving without acceleration, where the effect of the added mass term was diminished completely. While the wing was translating with a constant velocity, the resultant force increased with the development of the LEV and reached its maximum value. After that, it remained approximately constant at the end phases of the motion. In addition, for the wings with a stiffener, the effect of the variation of the resultant force diminished as the bending stiffness in the chordwise direction increased. For example, the camber generation in magnitude for the wing with a 30° stiffener, which has the highest chordwise flexibility among the wings with a stiffener, showed the closest trend to the camber generation of the wing without a stiffener. That is, at the beginning of the acceleration phase ($0 \leq \delta^* \leq 0.2$), the influence of the added mass effect on the camber was observed clearly. When the wing kept accelerating ($0.2 < \delta^* \leq 1.0$), the camber increased monotonically with a smaller slope compared to the wing without a stiffener, whereas it starts decreasing when the wing started moving without an acceleration ($1.0 < \delta^* \leq 1.2$). With the development of the LEV, the camber started increasing in magnitude as the wing continues to move with a constant velocity. Furthermore, for the wings with a 60° and 90° stiffener, the influence of the force generation on the camber was diminished since the wing has more resistivity to the deformation because of the additional bending stiffness in the chordwise direction provided by the stiffeners. Although the effect of the added mass term was observed at the beginning of the acceleration phase ($0 < \delta^* \leq 0.2$), for two wings, the slope of camber variation became lowest and second lowest for the wing with a 90° and 60° stiffener. Similarly, at the beginning of the constant velocity phase ($1.0 < \delta^* \leq 1.2$), there is no decrease in the camber generation was observed for two wings even though the added mass term was eliminated. After that ($1.2 < \delta^*$), the camber was increased slightly for two wings because of the development of the LEV around the wing surface.

As a result, it can be concluded that, for the translating and revolving wings, which start accelerating from rest with constant acceleration for one chord length of travel, then keep translating or revolving with a constant velocity, may have similar temporal evolution of the resultant force generated by the wings. Moreover, the variation of camber is a function of the resultant force acting on the wing surface and the chordwise flexibility of the wing influences its magnitude. As the chordwise flexibility increases the wing becomes more compliant to the deformation, which means that the wing has less resistance capability to the net force acting on its surface. Therefore, the wing deforms according to the variation of the resultant force during the motion. The wings with an additional chordwise bending stiffness, on the other hand, resist the sudden variation of the net force generation, which results in a smooth change of the camber generation during the motion. These results prove that the presence of the stiffeners enhances the bending stiffness of the wing in a chordwise direction since the wing with a stiffener shows more resistance to the variation of the resultant force compared to the wing without a stiffener. In addition, the stiffener orientation influences the bending stiffness of the wing in a chordwise direction. As the angle between the stiffener and leading-edge increases, in which the stiffener is tilted more in the chord direction, the chordwise rigidity of the wing increases.

CHAPTER 5

CONCLUSION

In this study, for the linear translating motion, the significance of the stiffener angle between the leading edge on the flow characteristics is experimentally investigated. By changing the orientations of stiffeners that are consecutively integrated into the wing surface, wings with bending stiffness in different directions were obtained. When the angle between the stiffener and leading-edge increases, in which the stiffeners on the wing surface are tilted more in the chord direction, the wing flexibility in the chordwise direction decreases. Therefore, the wing with the highest chordwise flexural stiffness was obtained by placing the stiffeners that have a 90° angle with the leading edge. Similarly, wings with stiffeners having 60° and 30° angles between the leading edge, were ordered as second and third wings in terms of the chordwise flexural stiffness, respectively. Moreover, the wing without a stiffener displayed the highest chordwise flexibility since there was no stiffener integrated on the wing surface resisting wing deformation in a particular direction. The wing motion consisted of two stages, which were the constant acceleration stage, and the constant velocity stage. In the first phase of the motion, the wing starts accelerating from rest with constant acceleration for one chord length of travel ($0 \leq \delta^* \leq 1.0$). At the end of the first phase, the wing achieves the terminal velocity, whereas, in the second phase of the motion, the wing translates with constant terminal velocity, which is achieved at the end of the acceleration phase, for three-chord lengths of travel ($1.0 < \delta^* \leq 3.8$). The angle of attack was set to 45 degrees at the beginning of the motion for all of the wings. The flow field around the wings with different chordwise flexibility provided by the different stiffener orientations was investigated experimentally via two-dimensional two-component particle image velocimetry (2D2C PIV).

The temporal evolution of the geometric angle of attack during the motion showed that the presence of stiffener increases the wings' flexural stiffness in a chordwise direction. That is, a wing without a stiffener reveals the lowest geometric angle of attack compared to the wings with stiffeners, since it realigns in the flow direction with ease as a result of more deformation capability in the chordwise direction. Moreover, the angle between the leading edge and the stiffener alters the flexibility in the chordwise direction. Wing with a 90° stiffener, for example, performed the highest geometric angle of attack compared to the other wings with a lower stiffener angle at each phase of the motion. Expectedly, the wing with a 60° and 30° stiffener, on the other hand, showed the second and the third highest geometric angle of attack, respectively. Throughout the motion, the average angle of attack of the wing without a stiffener and wings with a 30° , 60° , and 90° stiffener is 31.1° , 33.3° , 38.3° , and 42.1° , respectively.

Camber generation in magnitude, on the other hand, enhances as the chordwise flexure increases. Note that, the wing with high chordwise flexibility deforms in a way that the wing has negative camber generation, which is not favorable since it results in a decrease in lift and drag force. Experiments showed that the presence of stiffener increases the camber generation in a positive direction by increasing the resistivity of the wing to the forces acting on the wing surface. Therefore, placing stiffeners on the wing surface may enhance the wing lift and drag generation by providing additional bending stiffness in the chord direction, which diminishes the negative camber generation in magnitude. In addition, although a wing with a 90° stiffener produces the highest leading-edge vortex circulation, which is the dominant force generation mechanism in flapping-wing flight, it showed the least camber generation during the motion. This result also summarized that the presence of a stiffener increases the chordwise flexibility, where the amount of enhancement depends on the angle between the stiffener and the leading edge. By increasing the angle between the leading edge and the stiffener, the wings with enhanced chordwise flexural stiffness can be obtained since the stiffeners are tilted more in the chord direction. Throughout the motion, the average camber in the magnitude of the wing

without a stiffener and wings with a 30°, 60°, and 90° stiffener is 5.52% c, 4.23% c, 3.11% c, and 1.7% c, respectively.

PIV measurements showed that at the initial phases of motion, a coherent leading-edge vortex is formed for all the wings tested in the experiment and LEV remains stable over a long period of movement. For approximately 2.4 chord lengths of travel ($0 \leq \delta^* \leq 2.4$), the flow fields of vortical structures have similar characteristics for all wings. However, after 2.4 chords length of travel ($2.4 < \delta^* \leq 3.8$), the vortical structures started to be distinguished from each other as a result of the different geometric angle of attack and camber generation depending on the wings' chordwise flexibility, which is modulated by the stiffener angle. After 3.0 chord lengths of travel ($3.0 < \delta^* \leq 3.8$), fully chaotic flow in the wake was observed for the wings with a 60° and 90° stiffener angle. Among all wings tested, the wing without a stiffener generated less chaotic flow in the wake because of the smaller geometric angle of attack. Furthermore, the flow remained attached to the surface and left the trailing edge tangentially for a 3.0 chord length of travel ($0 \leq \delta^* \leq 3.0$) for all wings tested. However, after 3.4 chord length of travel ($3.4 \leq \delta^* \leq 3.8$), because of the LEV staying close to the trailing edge, the flow detached from the surface for the wing without a stiffener. This situation was observed for wings with a 30° and 60° stiffener angle after 3.8 chord length of travel ($3.8 \leq \delta^*$).

The LEV circulation was enhanced monotonically in the acceleration phase of the motion ($0 \leq \delta^* \leq 1.0$) with an almost constant slope for all wings tested. Moreover, in the constant velocity phase ($1.0 < \delta^* \leq 3.8$), for all wings the LEV circulation kept increasing in the following 0.6 chord length of travel ($1.0 < \delta^* \leq 1.6$). After that, it decreased slightly ($1.6 < \delta^* \leq 2.8$), then remained approximately constant until the end of the motion ($2.8 < \delta^* \leq 3.8$). Throughout the motion, the wings that have a stiffener on their surface produced higher LEV circulation compared to the wing without a stiffener. Therefore, it can be concluded that the presence of stiffener increased the LEV circulation around the wing, by increasing the geometric angle of

attack and reducing the negative angle of attack formation. Among the wings with a stiffener, the wing with a 90° stiffener angle produced the greatest LEV circulation, where it was followed by the wing with a 60°, and 30° stiffener angle. Therefore, it can be stated that the stiffener angle influences the LEV circulation. By altering the stiffener orientation, the LEV circulation can be modulated. The average non-dimensional LEV circulations generated by the wing without a stiffener was 0.87, whereas it was calculated as 1.07, 1.01, and 0.91 for the wings with a 90°, 60°, and 30° stiffener, respectively. Similarly, the TEV circulation decreased as the chordwise flexibility increased since a smaller TEV was required to re-establish the Kutta condition. Moreover, according to the TEV and LEV circulations, it can be stated that the LEV and TEV circulations are related to each other and higher TEV circulation results in higher LEV circulation.

Since the wing re-aligns in the flow direction with ease, the closest LEV motion to the surface is observed around the wing without a stiffener. It is followed by the wings with a 30° and 60° stiffener. Moreover, the position of the LEV centroid had a similar movement for all wings in the acceleration phase ($0 \leq \delta^* \leq 1.0$), whereas, in the constant velocity phase ($1.0 < \delta^* \leq 3.8$), at the beginning of the motion ($1.0 < \delta^* \leq 1.6$), the LEV centroid in the y-axis had a similar trajectory. However, they were differentiated from each other after 1.8 chord length of travel. In contrast, the positions of the LEV centroid in the y-axis converged each other at the end of the motion ($\delta^* = 3.8$). In the x-axis, on the other hand, the position of the LEV centroids remains similar for a 2.8 chord length of travel ($1.0 < \delta^* \leq 2.8$). After 2.8 chord length of travel, the position of the LEV centroid of the wing without a stiffener and with a 30° and 60° stiffener angle changes with a similar trend for 0.6 chord length of travel ($2.8 < \delta^* \leq 3.4$). At the end of the motion ($3.6 \leq \delta^* \leq 3.8$), the LEV centroid of the wings with a stiffener converged with each other, whereas for the wing without a stiffener, the LEV centroid was positioned at a far distance in the x-axis. The total distance between the LEV centroid and the leading edge was approximately the same for wings without a stiffener and wings with a 30° and 60°

stiffener. For the wing with a 90° stiffener, on the other hand, while the total distance was calculated in the same way as the other wings, the length started to change suddenly after 2.8 chord length of travel ($2.8 < \delta^* \leq 3.8$). The TEV positions in the x-axis showed the same trend throughout the motion, whereas the position of the TEVs in the y-axis are distinguished from each other. During the motion, in the y-axis, the TEV centroid for the wing without a stiffener was positioned in the closest position for the wing without a stiffener, compared to the other wings. Similarly, among the wings with a stiffener, the distance between the TEV centroid and the leading edge decreased from the wing with a 90° stiffener to a 30° stiffener. In the x-axis on the other hand, during the motion, the TEV centroid was in the closest position to the LE for the wing with a 90° stiffener, whereas the biggest distance was measured for the wing with a 30° stiffener. Furthermore, the total distance between the TEV centroid and the LEV was calculated as approximately the same for all wings. Therefore, it can be concluded that, although the position of the TEV centroid with respect to the LE changes in the y and x axes differently, the total distance between the TEV centroid and LE remained approximately constant for all wings tested.

According to the comparison between the study carried out by Meerendonk (2016), it can be concluded that for the translating and revolving wings, which start accelerating from rest with constant acceleration for one chord length of travel, then keep translating or revolving with a constant velocity, may have similar temporal evolution of the net force generated by the wings. An increase in chordwise flexibility results in a reduction of the net force since the deformation of the wing structure dumps the force generation by the wing. Moreover, the variation of camber is a function of the resultant force acting on the wing surface and the chordwise flexibility of the wing influences its magnitude. As the chordwise flexibility increases the wing becomes more compliant to the deformation, which means that the wing has less resistance capability to the net force acting on the surface. Therefore, the wing deforms according to the variation of the resultant force during the motion. In contrast, the wings with a chordwise bending stiffness, resist the

sudden variation of the net force generation, which results in a smooth change of the camber generation during the motion. Furthermore, these results prove that the presence of the stiffeners enhances the bending stiffness of the wing in a chordwise direction since the wing with a stiffener shows more resistance to the variation of the resultant force increases compared to the wing without a stiffener. The stiffener orientation, on the other hand, influences the bending stiffness of the wing in a chordwise direction. As the angle between the stiffener and leading-edge increases, in which the stiffener is tilted more in the chord direction, the chordwise rigidity of the wing increases.

This study showed that 3D printing technology provides an enormous opportunity to manufacture flexible wings with complex geometric designs and variable structural properties along the wingspan in a short time with a low tolerance in production. Moreover, by altering the stiffener properties, such as their orientations, and geometric and structural properties, of the 3D printed wings systematically, the camber and geometric angle of attack, thereby the LEV circulation around the wing surface can be adjusted. As a result, the optimum wing structure that offers the best flight performance in terms of aerodynamic efficiency can be designed and manufactured for the necessary flapping-wing micro aerial vehicle operations.

As a future work, the studies written below can be done:

- The influence of stiffener and its orientation can be investigated during a revolving motion.
- The stroke reversal mechanism can be performed at the end of the motion kinematics to observe the effect of stiffeners on rotational forces and the wake capture effect.
- To investigate the influence of stiffeners on force generation, force measurements can be performed.
- A flapping-wing micro aerial vehicle can be completely designed and manufactured.

REFERENCES

A. (2021). 3D Printer | Raise3D. Raise3D: Reliable, Industrial Grade 3D Printer. <https://www.raise3d.com/3d-printers/>

Ahmed, M., Islam, M.R., Vanhoose, J., Hewavitharana, L., Stanich, A., & Hossain, M. (2016). Comparisons of Bending Stiffness of 3D Printed Samples of Different Materials. Volume 9: Mechanics of Solids, Structures and Fluids.

Anderson, J. (2011). Fundamentals of Aerodynamics. Anderson series. McGraw-Hill.

Aono, H., Chimakurthi, S., Cesnik, C., Liu, H., & Shyy, W. (2009). Computational Modeling of Spanwise Flexibility Effects on Flapping Wing Aerodynamics. 47th AIAA Aerospace Sciences Meeting Including The New Horizons Forum and Aerospace Exposition.

Beer, F., Johnston, E., DeWolf, J., & Mazurek, D. (2019). Mechanics of Materials (8th ed.). McGraw Hill.

Birch, J. M., & Dickinson, M. H. (2001). Spanwise flow and the attachment of the leading-edge vortex on insect wings. *Nature*, 412(6848), 729.

Brossard, C., Monnier, J. C., Barricau, P., Vandernoot, F. X., Le Sant, Y., Champagnat, F., & Le Besnerais, G. (2009). Principles and applications of particle image velocimetry.

Daniel, T. L. (2002). Flexible wings and fins: Bending by inertial or fluid-dynamic forces? *Integrative and Comparative Biology*, 42(5), 1044–1049.

Combes, S. A., & Daniel, T. L. (2003). Flexural stiffness in insect wings I. Scaling and the influence of wing venation. *Journal of experimental biology*, 206(17), 2979–2987.

Dickinson, M. H. and Götz, K. G. (1993). Unsteady aerodynamic performance of model wings at low Reynolds numbers. *J. Exp. Biol.* 174, 45-64.

Dickinson, M. H., Lehmann, F. O., & Sane, S. P. (1999). Wing Rotation and the Aerodynamic Basis of Insect Flight. *Science*, 284(5422), 1954–1960.

Dudley, T.R. (1987). The mechanics of forward flight in Insects. Ph.D. thesis, University of Cambridge.

Ellington, C. P. (1984). The aerodynamics of hovering insect flight. II. Morphological parameters. *Philosophical Transactions of the Royal Society of London. B, Biological Sciences*, 305(1122), 17-40.

Ellington, C. P., Van Den Berg, C., Willmott, A. P., & Thomas, A. L. (1996). Leading-edge vortices in insect flight. *Nature*, 384(6610), 626.

ENNOS, A. R. (1988). The Importance of Torsion in the Design of Insect Wings. *Journal of Experimental Biology*, 140(1), 137–160.

Fung, Y. C. (2008). An introduction to the theory of aeroelasticity. Courier Dover Publications.

Graftieaux, L., Michard, M., & Grosjean, N. (2001). Combining PIV, POD and vortex identification algorithms for the study of unsteady turbulent swirling flows. *Measurement Science and technology*, 12(9), 1422.

Heathcote, S., Martin, D., & Gursul, I. (2004). Flexible Flapping Airfoil Propulsion at Zero Freestream Velocity. *AIAA Journal*, 42(11), 2196–2204.

Heathcote, S., Wang, Z., & Gursul, I. (2008). Effect of spanwise flexibility on flapping wing propulsion. *Journal of Fluids and Structures*, 24(2), 183–199.

Jones, A. R., & Babinsky, H. (2010). Unsteady lift generation on rotating wings at low Reynolds numbers. *Journal of Aircraft*, 47(3), 1013-1021.

Lentink, D., & Dickinson, M. H. (2009). Rotational accelerations stabilize leading edge vortices on revolving fly wings. *Journal of Experimental Biology*, 212(16), 2705-2719.

MARDEN, J. H. (1987). Maximum Lift Production During Takeoff in Flying Animals. *Journal of Experimental Biology*, 130(1), 235–258.

Maxworthy, T. (1979). Experiments on the Weis-Fogh mechanism of lift generation by insects in hovering flight. Part 1. Dynamics of the 'fling'. *J. Fluid Mech.* 93, 47-63.

Muijres, F. T., Johansson, L. C., Barfield, R., Wolf, M., Spedding, G. R., & Hedenström, A. (2008). Leading-edge vortex improves lift in slow-flying bats. *Science*, 319(5867), 1250-1253.

Percin, M. (2015). Aerodynamic Mechanisms of Flapping Flight. Doctoral dissertation, Delft University of Technology.

Sane, S. P. (2003). The aerodynamics of insect flight. *Journal of Experimental Biology*, 206(23), 4191–4208.

Shyy, W., Aono, H., Chimakurthi, S. K., Trizila, P., Kang, C. K., Cesnik, C. E., & Liu, H. (2010). Recent progress in flapping wing aerodynamics and aeroelasticity. *Progress in Aerospace Sciences*, 46(7), 284-327.

Van de Meerendonk, R (2016). Three-dimensional flow and load characteristics of flexible revolving wings at low Reynolds number. Master thesis, Delft University of Technology.

Vogel, S. (1967). Flight in *Drosophila*. III. Aerodynamic characteristics of fly wings and wing models. *J. exp. Biol.* 46.

Wagner, H. (1925). Über die Entstehung des dynamischen Auftriebes von Tragflügeln. *ZAMM-Journal of Applied Mathematics and Mechanics/Zeitschrift für Angewandte Mathematik und Mechanik*, 5(1), 17-35.

Walker, J. A. (2002). Rotational lift: something different or more of the same? *Journal of Experimental Biology*, 205(24), 3783–3792.

Walker, P. B. (1931). Experiments on the growth of circulation about a wing and an apparatus for measuring fluid motion. Rep. Memo. Aeronaut. Res. (Great Britain) No 1402.

Weis-Fogh, T. (1973). Quick estimates of flight fitness in hovering animals, including novel mechanisms for lift production. *Journal of experimental Biology*, 59(1), 169-230.

Yang, W., Song, B., Song, W., & Wang, L. (2012). The effects of span-wise and chord-wise flexibility on the aerodynamic performance of micro flapping-wing. *Chinese Science Bulletin*, 57(22), 2887–2897.

Yazdanpanah, M. (2019). Flow characteristics of translating flexible wings at low Reynolds numbers. Master's thesis, Middle East Technical University

Zhao, L., Huang, Q., Deng, X., & Sane, S. P. (2009). Aerodynamic effects of flexibility in flapping wings. *Journal of The Royal Society Interface*, 7(44), 485–497.

Zhao, L., Deng, X., & Sane, S. P. (2011). Modulation of leading edge vorticity and aerodynamic forces in flexible flapping wings. *Bioinspiration & Biomimetics*, 6(3), 036007.